You can’t milk a cow with your hands in your pants.

Tom Van Laere – Admiral Freebee (2003)

Members of the jury

Prof. Dr. I. Lambrichts, UHasselt, Diepenbeek, Belgium, chairman

Prof. Dr. L. Michiels, UHasselt, Diepenbeek, Belgium, promoter

Prof. Dr. P. Wagner, UHasselt, Diepenbeek, Belgium, co-promoter

Dr. V. Vermeeren, UHasselt, Diepenbeek, Belgium, co-promoter

Prof. Dr. M. Ameloot, UHasselt, Diepenbeek, Belgium

Prof. Dr. J. Lammertyn, KU Leuven, Leuven, Belgium

Prof. Dr. P. Dubruel, UGent, Gent, Belgium

Prof. Dr. L. Lagae , KU Leuven, Leuven, Belgium

Dr. D. Molin, UM, Maastricht, The Netherlands

Table of contents

List of abbreviations

10-UDA	10-undecenoic acid
A_1 (Ω)	denaturation-related decay amplitude (ohm)
A_2 (Ω)	medium exchange-related decay amplitude (ohm)
Ab-AI488	Alexa Fluor® 488 labeled antibody
AC	alternating current
ACT	activated clotting time
AP	alkaline phospatase
BH_4	tetrahydrobiopterin
BRCA1	breast cancer 1
BSA	bovin serum albumin
C (F)	capacitance (farad)
C_{dl} (F)	double layer capacitance (farad)
cDNA	copy DNA
CNT	carbon nanotubes
CRP	C-reactive protein
cTnT	cardiac troponin-T
CVD	chemical vapour deposition or cardiovascular disease
Cyt C	cytochrome c
DGGE	denaturing gradient gel electrophoresis
dsDNA	double-stranded DNA
EDC	1-ethyl-3-(3-dimethylaminopropyl)-carbodiimide
ELISA	enzyme-linked immunosorbent assay
EIS	electrochemical impedance spectroscopy
FET	field-effect transistor
FITC	fluorescein isothiocyanate
FM	full match
FMM	full mismatch
gDNA	genomic DNA
GID	interdigitated gold electrodes
GOD	glucose oxidase
hGH	human growth hormone
HRP	horseradisch peroxidase
HTM	heat-transfer method
I (A)	current (ampere)
IFN	interferon
IGF	insulin growth factor

IL	interleukin
ISE	ion-selective electrode
MA	methamphetamine
MDM2	murine double minute 2
MES	2-(N-morpholino)ethanesulfonic acid
MM	mismatch
NCD	nanocrystalline diamond
NCD:COOH	carboxyl-terminated NCD
NCD:H	H-terminated NCD
NCD:O	O-terminated NCD
NGS	next generation sequencing
NP	nanoparticle
N. R_{th} (°C/W)	normalized R_{th} (degree Celsius per watt)
Ω (Hz)	frequency (hertz)
PAH	phenylalanine hydroxylase
PBS	phosphate buffered saline
PCR	polymerase chain reaction
PKU	phenylketonuria
POC	point-of-care
PS	polystyrene
PSA	prostate cancer marker
φ	phase shift
Q	constant phase element
QCM	quartz crystal microbalance
R (**Ω**)	resistance (ohm)
R_{ct} (**Ω**)	charge transfer resistance (ohm)
RT	room temperature
R_{th} (°C/W)	heat-transfer resistance (degree Celsius per watt)
SDS	sodium dodecyl sulphate
SEM	scanning electron microscope
SMCC	Succinimidyl-4-(N-maleimidomethyl)cyclohexane-1-carboxylate
SNP	single nucleotide polymorphism
SPR	surface plasmon resonance
SSC	sodium chloride/sodium citrate
ssDNA	single-stranded DNA
TBS	tris buffered saline
TFAAD	trifluoro-acetamide
T_m (°C)	melting temperature (degree Celsius)

TNF	tumor necrosis factor
TRIS	tris(hydroxymethyl)aminomethane
τ_1 (min)	Denaturation time constant (minute)
τ_2 (min)	Medium exchange time constant
τ_3 (min)	Fluorescence decay time constant
U (V)	potential (volt)
UV	ultraviolet
V (V)	voltage (volt)
VEGF	vascular endothelia growth factor
WBCs	white blood cells
Z ()	impedance (ohm)

List of figures

List of tables

Summary

A biosensor is an integrated device, combining a biological recognition element with a transducer. The transducer translates the recognition of target molecules into a quantifiable output signal. Since the first biosensor in 1962, a lot of different biosensor platforms are developed for a multitude of applications, but mostly for medical applications. Biosensors can be categorized by the type of recognition element, like enzymes, antibodies and DNA-molecules. Alternatively, biosensors can be classified based on the type of transduction principle. There are for example electrochemical, optical and piezoelectrical biosensors. Electrochemical transduction is preferred for clinical diagnostics, because it can be used for the relative cheap, fast and sensitive detection of disease-related biomarkers, like proteins and DNA-molecules. The different types of electrochemical biosensors as well as their (potential) clinical applications are discussed in Chapter 1. Diamond is an attractive alternative transducer material, because it has better electronic and chemical properties as compared with traditional transducer materials like silicon (Si) and gold (Au). The properties and advantages of diamond are discussed in Chapter 1.

The main goal of this dissertation was to develop an universal biosensor platform based on nanocrystalline diamond (NCD) electrodes for the label-free and real-time detection of C-reactive protein (CRP) in cardiovascular disease (CVD) patient serum samples and for the detection of point mutations in PKU patient DNA samples.

In Chapter 3, an impedimetric DNA-sensor for the detection of single nucleotide polymorphisms (SNPs) in synthetic 29-mer DNA fragments was developed. SNP detection was based on the difference in the intrinsic stability upon chemically induced denaturation. A mathematical model was used to describe the impedimetric denaturation kinetics of complementary and SNP-containing DNA fragments. Longer denaturation times were observed for complementary DNA fragments as compared to mismatched DNA fragments. Even the denaturation times of to different SNP-containing DNA fragments were distinct from each other. The developed, impedimetric DNA-sensor was able of fast and label-free SNP detection in synthetic DNA fragments. However, the disadvantage of this impedimetric method is the requirement of complex data

analysis. Therefore a second DNA-sensor based on a new transduction principle was developed, as described in Chapter 4 and 5.

In Chapter 4, a new type of DNA-sensor for the detection of SNPs in synthetic 29-mer DNA fragments was developed. SNP detection was based on the difference in heat-transfer resistance (R_{th}) upon thermal denaturation of DNA fragments. An increase in R_{th} was observed upon denaturation of double-stranded (ds) DNA fragments. The temperature associated with the change in R_{th} was correlated with the melting temperature of the immobilized DNA fragments. The highest T_m was obtained for the complementary DNA fragments, the mismatched DNA fragments had lower T_m's. The developed R_{th}-based DNA-sensor was able to detect common PKU related SNPs in 29-mer synthetic fragments of the PAH gene. However, in order to translate this technique into a simplified multiplexed assay for routine genetic analysis, the R_{th}-based method must be extend to exon-size SNP analysis in patient-derived DNA fragments, as described in Chapter 5.

In Chapter 5, the use of the R_{th}-based DNA sensor for SNP detection in exon-length PAH DNA fragments up to a length of 123 base pairs was described. Additionally, the Rth-based sensor was able to detect 3 of the most common SNPs in the PAH gene associated with PKU, based on a difference in T_m.

In Chapter 6, an impedimetric immunosensor for the real-time detection of CRP was developed. Our prototype of CRP sensor reached sensitivity within physiologically relevant concentration ranges in buffer solutions. Additionally, the impedimetric immunosensor was able to distinguish between unspiked serum and serum spiked 500 nM CRP. In the future, the immunosensor needs to be improved to reach clinical relevant detection limits in CVD patient samples. Possible improvements are described in Chapter 7.

In Chapter 7, the obtained results were critically evaluated and some future prospects and possible improvements were summarized. In the future, the improved R_{th}-based DNA-sensor should be able to detect both PKU patients as well as PKU carriers. On the other hand, the improved impedimetric immunosensor could be used in the future for the prediction of CVD's.

Nederlandstalige samenvatting

Biosensoren zijn analytische apparaten die bestaan uit een laag van biologische herkenningsmoleculen gebonden aan een vaste drager, genaamd een transducer. Deze transducer vertaalt de herkenning van biologische doelwitmoleculen in een kwantificeerbaar uitleessignaal. Sinds de eerste biosensor in 1962 werden er verschillende biosensorplatformen ontwikkeld voor tal van uiteenlopende toepassingen. De meeste biosensoren werden echter ontwikkeld voor toepassingen binnen de klinische wereld. Biosensoren kunnen ingedeeld worden volgens het gebruikte type biologische herkenningsmolecule, zoals enzymen, antilichamen of DNA-moleculen. Biosensoren kunnen op alternatieve wijze ingedeeld worden via de gebruikte uitleesmethode. Zo bestaan er o.a. elektronische, optische en piëzo-elektrische biosensoren. Echter voor klinische toepassingen geniet elektronische uitlezing de voorkeur, omdat het mogelijk is om via deze uitleesmethode biomerkers, gerelateerd met bepaalde ziektes, op een relatief goedkope, snelle en gevoelige manier op te sporen. De verschillende soorten elektronische biosensoren en hun klinische toepassingen worden besproken in Hoofdstuk 1. Synthetisch diamant is een interessant alternatief voor de veel gebruikte transducermaterialen, zoals silicium en goud. Diamant overtreft silicium en goud met betere elektronische en chemische eigenschappen, zoals beschreven in Hoofdstuk 1.

Het doel van deze thesis was het ontwikkelen van een universeel biosensorplatform, dat gebruik maakt van nanokristallijn diamant als transducer en van een real-time en labelvrije uitleesmethode. Dit voor het opsporen van enerzijds C-reactief eiwit (CRP) in patiënten die een verhoogd risico vertonen voor hart- en vaatziekten en anderzijds voor het opsporen van puntmutaties in het DNA van personen die mogelijks lijden aan de genetische aandoening Fenylketonerie (PKU).

In Hoofdstuk 3 werd er een DNA-sensor ontwikkeld voor de impedimetrische detectie van puntmutaties tijdens de chemische denaturatie van synthetische DNA-fragmenten van 29 baseparen lang. Kinetische verschillen tijdens de denaturatie van complementaire DNA-fragmenten en DNA-fragmenten die een puntmutatie bevatten werden waargenomen. Gebruikmakend van het voorgestelde wiskundig model, konden de denaturatietijden van de verschillende

DNA-fragmenten berekend worden. De langste denaturatietijd was geassocieerd met de denaturatie van de complementaire fragmenten, de kortste tijd met de fragmenten die een puntmutatie bevatten. Het bleek zelfs mogelijk om onderscheid te maken tussen de denaturatietijden van DNA-fragmenten met een identieke puntmutatie op een andere positie. De ontwikkelde impedimetrische DNA-sensor kan op een snelle en labelvrije manier puntmutaties opsporen in synthetische DNA-fragmenten. Een nadeel is echter dat ingewikkelde analyse van de ruwe data vereist is. Daarom werd er een tweede type DNA-sensor ontwikkeld voor de detectie van puntmutaties tijdens de thermische denaturatie van DNA-fragmenten gebaseerd op een verschil in thermische weerstand tussen geïmmobiliseerde dubbelstrengige en enkelstrengige DNA-fragmenten, zoals beschreven in Hoofdstuk 4 en 5.

In Hoofdstuk 4 werd het principe van de thermische DNA-sensor uitgewerkt a.d.h.v. de denaturatie van synthetische DNA-fragmenten van 29 baseparen lang. Een lagere thermische weerstand voor dubbelstrengige DNA-fragmenten werd waargenomen t.o.v enkelstrengige DNA-fragmenten. De overgang van een lagere naar een hogere thermische weerstand kon gecorreleerd worden met de smelttemperatuur van de gebruikte DNA-fragmenten. In vergelijking met complementaire DNA-fragmenten startte de overgang van lage naar hoge thermische weerstand op een lagere temperatuur wanneer DNA-fragmenten met een puntmutatie werden gedenatureerd. Op deze manier, kan de thermische sensor op een goedkope en snelle manier puntmutaties opsporen in synthetische DNA-fragmenten. Vooraleer deze sensor kan gebruikt worden voor routinematige genetische analyses, moet de bruikbaarheid van deze sensor uitgebreid worden naar het opsporen van puntmutaties in DNA-fragmenten afkomstig van PKU-patiënten. Dit wordt beschreven in hoofdstuk 5.

In Hoofdstuk 5 werd de thermische DNA-sensor gebruikt voor het opsporen van puntmutaties in DNA-fragmenten tot een lengte van 123 baseparen lang. Deze lengte is vergelijkbaar met die van exonen. De thermische sensor kon de 3 vaakst voorkomende puntmutaties, geassocieerd met de genetische aandoening PKU, opsporen.

In Hoofdstuk 6 werd een impedimetrische immunosensor ontwikkeld voor de real-time detectie van CRP. In fysiologische buffer oplossingen kon een

detectielimiet van 10 nM bereikt worden. Deze concentratie benadert het fysiologische concentratiegebied. Daarenboven kon de ontwikkelde impedimetrische immunosensor onderscheid maken tussen serum en serum waaraan hoge concentraties CRP werden toegevoegd. De immunosensor zal in de toekomst aangepast worden, zodat klinisch relevante detectielimieten bereikt kunnen worden in serumstalen van personen die een verhoogd risico vertonen op hart- en vaatziekten, zoals beschreven in Hoofdstuk 7.

In Hoofdstuk 7 werden de bekomen resultaten kritisch beoordeeld en werden er suggesties opgesomd om de ontwikkelde biosensoren nog te verbeteren in de toekomst. Verbeteringen aan de thermische DNA-sensor zouden ervoor kunnen zorgen dat deze sensor in de toekomst niet alleen patiënten maar ook dragers van de genetische aandoening PKU kan opsporen. Een verbeterde impedimetrische immunosensor zou gebruikt kunnen worden om het risico op hart- en vaatziekten te voorspellen.

1

INTRODUCTION AND AIMS

In healthcare the demand for point-of-care diagnostics is growing. Point-of-care diagnostics entails the detection of certain disease-related markers on site, e.g. at the GP's office or even at the patient's home. Essential features are fast result analysis, cheap production cost, reliability and sensitivity. State-of-the-art disease-related biomarker detection techniques, like DGGE, microarray and ELISE, have many disadvantages. Mainly the use of labels, the associated expensive read-out instrumentation and the long sample-to-diagnosis time. For these reasons a lot of research is being performed on the development of miniaturized and automated devices, called biosensors, as fast, inexpensive and simple alternative for the detection of molecular biomarkers.

1.1 Biosensor

A biosensor is an integrated device, combining a biological recognition element with a transducer, which is capable of translating a biorecognition process into a quantifiable output signal [Thévenot et al., 1999]. The first descriped biosensor was an amperometric enzyme-based sensor for glucose monitoring introduced in 1962 by Clark and Lyons [Clark et al., 1962]. Since then, there was a continuous growth in designs of biosensors for a multitude of applications. However, most frequently biosensors are developed for medical applications [Turner et al., 2013]

Modern medicine has shifted the focus from diagnosis based on a variety of symptoms towards the detection of disease-related biomarkers. Biomarkers are biological molecules, including lipid metabolites, peptides, proteins and DNA-based markers, such as gene mutations or polymorphisms. Currently, biomarker tests are typically performed at centralized laboratories using large automated clinical analyzers. Therefore, it takes some time before the test results are known by a patient. In contrast, biosensors have the potential to provide rapid and real-time results using inexpensive equipment at the Doctor's cabinet or even at home. Widely known examples of self-test biosensors are the glucometer and the pregnancy test. However, there is still need for more biosensor devices in other application fields like emergency medicine.

Biosensors can be categorized by the recognition element, there are enzyme-based biosensors, immunological biosensors, and DNA biosensors. Alternatively, based upon the transduction principle, there are electronic

biosensors (electrical or electrochemical) [Fan et al., 2003; Park et al., 2002], optical biosensors (fluorescent, surface plasmon resonance, or Raman) [Taton et al., 2000; Gaylord et al., 2002], and piezoelectric biosensors (quartz crystal microbalance) [Cooper et al., 2001]. This dissertation will focus on electrochemical biosensors as wel as their potential clinical applications. Also nanocrystalline diamond (NCD) will be introduced as alternative transducer material.

1.2 Electrochemical biosensors

Electrochemical biosensors have traditionally received most attention, because of the low cost, the real-time detection and the simplicity to miniaturize. Electrochemical biosensors can be subdivided in: (1) potentiometric, (2) voltammetric or amperometric, (3) conductometric and (4) impedimetric biosensors, based upon their analytical working principal.

1.2.1 Potentiometric biosensors

Potentiometric sensors measure the potential across a membrane in a two electrode electrochemical cell under zero current conditions. The difference in potential shows a logarithmic relationship with the analyte concentration, described by the Nernst equation. Commercial available potentiometric sensors, including glassy carbon electrodes and ion-selective electrodes (ISE), are used for the determination of various ions in many applications. The best known example is the pH meter. This electrode measures hydrogen ion concentrations in solutions.

In the literature, potentiometric biosensors have been reported since the sixties. However, only a small number can be applied for biomedical analysis. An example is the enzyme-based biosensor, containing urease, for the detection of urea, which is an important indicator for kidney dysfunction. Urease converts urea into ammonium and bicarbonate ions, therefore the analysis can be carried out in a number of ways. Urea detection is possible with enzyme-modified ammonium ISEs [Syu et al., 2009], ammonia gas electrodes [Lui et al., 1997] or with pH-electrodes [Lakard, et al., 2011]. Due to insufficient selectivity of ammonium ISEs, alkaline ions in clinical samples interfere in urea analysis. A possible approach for the removal of interfering ions from samples is the use of

a cation exchange system before analysis. This purpose has been successfully utilized for the detection of clinically relevant concentrations of urea in dialysis fluids [Radomska et al., 2004].

In conventional potentiometric immunoassays the antigen-antibody binding reaction is often insufficient to produce a large signal change. Therefore, most potentiometric immunsensors described in literature require the use of enzyme labels for signal amplification [Koh et al., 2009]. The main disadvantage of label-based immunoassays is the indirect detection of antigens, increasing the reaction time. Additionally, enzyme labels are rather expensive. To overcome these disadvantages label-free potentiometric immunosensors are intensively investigated. Recently, reports have been published that describe the direct potentiometric shift upon antigen-antibody reaction. The label-free detection was improved by increasing the biorecognition interface with nanoparticles [Tang et al., 2005] or with a three-dimensional porous chitosan film attached to the electrode [Liang et al., 2008]. The potentiometric immunosensor with three-dimensional porous structure exhibits a linear range from 6.85 to 708ng/mL with a detection limit of 3.89ng/mL for the detection of hepatitis B surface antigen in buffer solutions. The immunosensor was also tested with serum samples and compared to an ELISA-based method. There was no significant difference between the results obtained by the two methods. However to be applicable in clinical areas, the detection limit of the sensor needs to be improved to 0.5ng/mL, as recommend by the food and drug administration of the USA. Nowadays, the sensitivity of label-free potentiometric immunosensors is not acceptable for real biomedical applications.

Label-free potentiometric biosensors for the detection of DNA sequences are at an experimental level. Shiskanova et al. reported an ISE modified with ssDNA probes for potentiometric detection of the hybridization between complementary oligonucleotides. The oligo$(dA)_{15}$ modified electrodes were sensitive towards complementary oligo$(dT)_{15}$ targets in the concentration range of 9.43 – 377ng/mL [Shiskanova et al., 2007]. This DNA-sensor is unfortunaly obscured by the fact that the hybridization of polyoligonucleotides has questionable clinical relevance. Zhou et al. applied polyaniline electrodes to monitor the binding of 14-mer and 25-mer complimentary targets with the immobilized probes. No potential change was observed with non-complimentary

targets and with samples with a mutation in the sequence [Zhou et al., 2009]. The effect of increasing lengths of the probe and target molecules on potentiometric hybridization detection are currently studied. Untill now, label-free potentiometric DNA-sensors sensitive for SNP detection related to genomic diseases are not reported.

1.2.2 Voltammetric/Amperometric biosensors

Amperometric biosensors monitor the current associated with the redox reaction of electroactive analytes involved in the recognition process while a constant potential is applied. The current generated shows a linear relationship with the analyte concentration. The term voltammetry is used when the potential is not fixed, but varies linearly over time.

Most amperometric biosensors are enzyme-based biosensors. The majority described is used for blood glucose monitoring. In the 1970s, Yellow Springs Instruments was the first company that commercialized an amperometric biosensor: a bench top glucose analyzer. These first generation amperometric biosensors rely on reactions catalyzed by the enzyme oxidase and subsequent detection of H_2O_2 on platinum electrodes. However, the high oxidizing potential required for H_2O_2 oxidation results in interference from the oxidation of other compounds in complex media. Therefore, second generation biosensors make use of freely diffusing mediators (e.g. ferrocene species) to mediate the electron transfer between the immobilized glucose oxidase and the detection electrode. Soluble electron mediators are oxidized with lower potentials than required for H_2O_2 oxidation, therefore, decreasing the interference of non-specific analytes. The first company to market a second generation biosensor for blood glucose monitoring at home is MediSense. Since the 1980s, third generation sensors have been developed. They are based on enzymes and mediators that are both immobilized on the electrode surface. Thus, there is no need to add soluble mediators before a measurement. Therefore, third generation enzyme-based sensors allow continuous analyte monitoring. Continuous glucose monitoring systems are produced by Abbott, DexCom and Medtronic.

Amperometric enzyme-based biosensors are not only used for blood glucose monitoring. Other examples reported in the literature are the detection

of cholesterol [Gholivand et al.,2014], lactate [Lin et al., 2007] and ascorbate and uric acid [Nassef et al., 2007]. Recently, Nova Biomedical designed a hand-held device for the detection of whole blood creatinine, an indicator of renal function. The StatSensor uses a tri-enzyme construction, based on creatininase, creatinase and sarcosine oxidase immobilized on a membrane, to convert creatinine in H_2O_2 , which is amperometrically detected. A recent evaluation showed that whole blood creatinine levels measured with the StatSensor correlate well with laboratory plasma measurements (R^2=0.9328), but with a negative proportional bias at high creatinine concentrations. Also, high concentrations of creatine and urea overestimated creatinine levels [Schnabl et al., 2010].

Abbott constructed a commercially available, hand-held point-of-care (POC) system, that combines several amperometric and potentiometric biosensors. The i-STAT analyzer is used for the detection of multiple electrolytes and metabolites in clinical samples. For example this device can be used for measuring the activated clotting time (ACT). The i-STAT analyzer uses a single-use test strip onto which a clotting activator (ACT Celite) and a substrate for thrombin was deposited. Upon addition and coagulation of the sample, thrombin cleaves an electro-active group from the substrate. This electro-active group is detected amperometrically and the time of detection is measured in seconds. This device was evaluated for the monitoring of heparin therapy during cardiopulmonary bypass surgery. Their investigation showed that Hemochron (considered as a reference technique) and i-STAT ACT results were statistically different when high concentrations of heparin were used. Therefore further studies are needed to evaluate whether the i-STAT analyzer can be safely used to monitor heparin administration during cardiac surgery [Paniccia et al., 2003].

Although most amperometric biosensors are enzyme-based biosensors, amperometric immunosensors have also been developed. Because antibodies and antigens are not electrochemically active, they cannot participate directly in redox reactions. Therefore, electrochemically active labels, directly or as products of an enzymatic reaction, are needed, resulting in an indirect approach. An example of an amperometrically detectable complex is ferrocene monocarboxylic acid, as described by Prabhulkar et al. They described an amperometric biosensor for vascular endothelial growth factor (VEGF), a human

tumor biomarker [Prabhulkar et al., 2009]. The detection is based on a decrease in electrochemical response induced by the binding between VEGF and surface immobilized antibody complexed with ferrocene monocarboxylic acid, due to increased spatial blocking. A detection limit of 38 pg/mL in buffer solution was obtained. Additionally, there are immunosensors reported, that use enzyme labels with electrochemically active products. For example, alkaline phosphatase (AP) catalyzes the conversion of phenyl phosphate to the electrochemically active phenol. Examples of biosensors that use AP labeled antibodies as secondary antibodies in an sandwich assay are biosensors directed towards the cardiac biomarker troponin I [Christenson et al., 2009], towards markers for acute myocardial function, fatty acid binding protein [Key et al., 1999; O'Regan (a) et al., 2002] and myoglobin [O'Regan (b) et al., 2002], and towards a lipid metabolism marker apolipoprotein E [Meusel et al., 1995]. They all have ng/mL detection limits in body fluids. Furthermore, enzymes, such as horseradisch peroxidase (HRP), glucose oxidase (GOD) and others, have also been successfully used as labels. Siegmann-Thoss et al. developed an immunosensor for the detection of heart fatty acid binding protein (h-FABP) in blood plasma, based on a sandwich assay with immobilized anti-h-FABP antibodies and secondary GOD-labeled anti-h-FABP antibodies. The limit of detection of this immunosensor is 5 ng/mL in plasma [Siegmann-Thoss et al., 1996]. Additionally, HRP-labeled detection antibodies are used to detect disease specific antibodies [Belluzo et al., 2011; Pividori et al., 2009], hCG [Chetcuti et al., 1999; Santandrea et al., 1999] and prostate cancer marker (PSA) [Panini et al., 2008]. Moreover, metal oxides are also used as labels in amperometric immunosensors. Brianina et al. fabricated an amperometric biosensor for measurement of antibodies related to Forest-Spring encephalitis. The Forest-Spring encephalitis antigen was immobilized onto a screen printed graphite electrode to form an immune complex with antibodies present in human serum. This complex was recognized by gold-labeled protein A. The oxidation of gold (Au) is proportional to the concentration of antibodies in the range of 0.1 ng/mL to 10 µg/mL, with good agreement to the ELISA method [Brianina et al., 2003]. Currently, a commercial amperometrical POC immunosensor is available for targeted cardiac biomarker detection. The i-STAT (Abbott Point of Care, U.S.A) is capable of measuring the concentrations of cTnI, creatine kinase isoenzyme

MB (CK-MB) and B-type natriuretic peptide (BNP) cardiac markers directly from whole blood samples [Christenson et al., 2009].

DNA-sensors with amperometric read-out have also been reported. DNA hybridization has been detected by direct oxidation of the DNA or indirectly by using non-covalently bound redox mediators. The detection principle is based on an increased amount of labels bound when DNA is hybridized to a surface modified with a probe sequence. However, the sensitivity of these methods is not sufficient for practical applications. Electrochemical cycling of redox mediators can be used to amplify the signal. Lapierre et al. constructed a biosensor for the detection of PCR amplified DNA target sequences from Helicobacter pylori and the determination of a medically significant SNP. The biosensor utilizes a reaction between $Ru(NH_3)_6^{3+}$, a DNA-binding and redox-active probe, and $Fe(CN)_6^{3-}$, which permits Ru(III) to be regenerated for multiple redox cycles, thereby significantly amplifying the response obtained [Lapierre, 2003]. Improved sensitivity can also be achieved with miniaturized metal electrodes offering reduced background current. Sensitivity at the low pg/mL level is achievable when using Au nanoelectrodes [Gasparac et al., 2004; Lapierre-Devlin et al., 2005]. Similar to the Au nanoelectrode ensembles, vertically aligned diamond nanowires have been applied for DNA sensing [Yang et al., 2008]. Electrochemical detection of DNA hybridization was conducted with $Fe(CN)_6^{3-}$ as indicator. Clear discrimination between complementary and single-base-mismatched dsDNA was detected and a limit of detection of 14,1pg/mL for 23-mer fragments was reported.

1.2.3 Conductometric biosensors

Conductometric biosensors measure the change of the conductance between a working and a reference electrode in a bulk solution. Overall conductivity of a sample changes when electrochemical reactions generate or consume ions.

Conductometric biosensors often include enzymes, because some enzyme reactions generate charged products resulting in ionic strength changes, and thus increase conductivity. Examples include the measurement of urea, l-asparagine and creatinine using interdigitated electrodes [Cullen et al., 1990]. However, commercial applications of conductometric biosensors are limited due

to the variable ionic background of clinical samples and the requirement to measure small conductivity changes in these samples. One commercial system, for the measurement of urea in serum, plasma and urine, is the BUN analyzer (Beckman-Coulter) and is based on the enzyme urease. The hydrolysis of urea into the products NH_4^+ and HCO_3^- produces a change in sample conductivity. The initial conductivity is measured to compensate for the ionic background of the sample. However, this sensor is limited for the measurement of relatively high concentrations of urea, because low concentrations of analyte produce only small changes in conductivity [Eckfeldt et al., 1982].

Conductometric immunosensors have also been developed. Yagiuda et al. developed a sensor for the conductometric detection of methamphetamine (MA) in urine using antibody-immobilized platinum electrodes. Binding of MA with the immobilized antibodies caused a decrease in the conductivity. The conductivity change has a linear relationship with the MA concentration in the range of 1-10 µg/mL [Yagiuda et al., 1996]. Bangar et al. constructed a polypyrrole nanowire based immunosensor for measurement of cancer antigen 125. A decrease in conductance is observed upon exposure to the charged antigen, due to changes in the surface potential of the conducting polymer. The nanoimmunosensor has a detection limit of 1 U/mL and a dynamic range up to 1000 U/mL in spiked human blood plasma. The normal level of cancer antigen 125 in blood is less than 35 U/mL [Bangar et al., 2009]. Chua et al. presented an electrochemical immunosensor for cardiac troponin-T (cTnT) by creating an array of silicon (Si) nanowires. A limit of detection of 30 fg/mL in desalted serum samples was demonstrated [Chua et al., 2009].

Hahm et al. demonstrated that Si nanowires functionalized with peptide nucleic acid (PNA) receptors can distinguish wild-type from the ΔF508 mutation in 28-mer DNA fragments of the cystic fibrosis gene. Increase in conductance, on association of negatively charged nucleic acids, was observed at concentrations down to 86,2fg/mL [Hahm et al., 2004]. Although direct measurement of conductance change upon DNA hybridization is possible, often Au nanoparticles are used to enhance the signal. Au nanoparticles are coated with a probe nucleotide sequence complementary to one end of a target sequence. Another probe sequence that hybridizes to the other end of the target sequence is attached to the sensor surface between two electrodes. If the target

sequence is present, it will bind the nanoparticles to the surface. A subsequent silver precipitation on the Au particles, will result in a measurable conductivity signal. These hybridization-induced conductivity signals offer low detection levels down to 500 fM and point mutation selectivity [Park et al., 2002]. Nanosphere Inc. developed the Verigene system, a commercially available Au nanoparticle-based microarray assay system for the detection of mutations associated with abnormalities in blood coagulation [Lefferts et al., 2009; Maurice et al., 2010; Buchan et al., 2011]. Weizmann et al. constructed a DNA-sensor using enzyme-labeled DNA probes instead of Au nanoparticles. A detection limit of 94.2fg/mL was obtained and the impact of single, double and triple base pair mismatches in the target sequence was investigated. A decreased sensitivity was observed when the number of mismatches increased. They improved the sensitivity by performing the experiments at slightly elevated temperatures, 32 °C instead of 25 °C. Furthermore, the conductance data are comparable with theoretical melting temperatures. Finally, a detection limit of 9.42ng/mL for complementary ssDNA fragments in serum samples was reached, SNP sensitivity in serum samples was not investigated [Weizmann et al., 2010]. Maruccio et al. reported a prototype device consisting of a nanojunction array functionalized with molecular probes. The target sequences are labeled with conductive particles. As a consequence of target-probe binding, a conductive bridge forms between the electrodes, resulting in a discrete change of the electrical conductivity. The use of a small inter-electrode gap makes single biorecognition event sensitivity possible without silver deposition for signal enhancement [Maruccio et al., 2009].

1.2.4 Impedimetric biosensors

In a ideal resistor, the electrical resistance is defined by Ohm's law in terms of the ratio between voltage (V) and current (I):

$$R = \frac{V}{I} \tag{1.1}$$

However, in real world applications, the electrical circuit contains elements that exhibit more complex behavior. Instead of using the concept of resistance, the

term impedance is used. Electrochemical impedance is usually measured by applying an AC voltage to an electrochemical cell and then measuring the AC current through the cell. The applied V and the measured I can be written as sinusoidal functions in time:

$$V(t) = V_0 \sin(\omega t) \quad (1.2)$$

$$I(t) = I_0 \sin(\omega t + \varphi) \quad (1.3)$$

where V(t) is the potential at time t, V_0 is the amplitude of the signal, and ω is the frequency. The measured I(t) is shifted in phase (φ) and has an amplitude I_0.

Using Eulers relationship:

$$e^{j\varphi} = \cos\varphi + j \sin\varphi \quad (1.4)$$

the applied V(t) and measured I(t) can be written as complex functions:

$$V\ t = V_0 e^{j\omega t} \quad (1.5)$$

$$I(t) = I_0 e^{j\ \omega t - \varphi} \quad (1.6)$$

Where the real part of the complex function is described by amplitudes V_0 and I_0 and the imaginary part by the exponent of e.

Consequently, the simple R in equation (1.1), can be replaced by the complex impedance Z using equations (1.5) and (1.6):

$$Z = Z_0 e^{j\varphi} \quad (1.7)$$

Where the amplitude Z_0 and the phase φ are respectively the real part, Re(Z), and the imaginary part, Im(Z), of the complex impedance, Z.

Using equation (1.4), Z can also be described as:

$$Z = Z_0[\cos\ \varphi\ + j\sin(\varphi)] \tag{1.8}$$

Where

$$Re(Z) = Z_0 \cos\ \varphi \tag{1.9}$$

$$Im(Z) = Z_0 \sin(\varphi) \tag{1.10}$$

Impedance data can be presentated in two ways, in a Bode plot or in a Nyquist plot. In a Nyquist plot the Re(Z) is plotted on the X-axis and the negative Im(Z) is plotted on the Y-axis. Each point on the Nyquist plot represents the impedance at one frequency. On a Nyquist plot the low frequency data are shown on the right side of the plot and higher frequencies are shown on the left. The impedance can be represented as a vector with magnitude |Z|. The angle between this vector and the X-axis represents the phase shift φ. Figure 1.1 shows an example of a Nyquist plot for a parallel RC circuit. The semicircle is characteristic for such a circuit at a single time point.

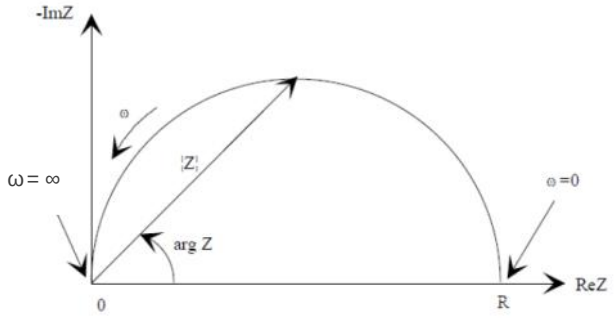

Figure 1.1: Nyquist plot for a parallel RC circuit. This curve displays – Im(Z) versus Re(Z) [Basics of Electrochemical Impedance Spectroscopy, application note Gamry Instruments].

In a Bode plot, the impedance is plotted with a logarithmic presentation of ω on the X-axis and a logarithmic presentation of the magnitude of the impedance (

|Z|=Z(0)) or the phase shift on the Y-axis. The Bode plot for the parallel RC circuit is shown in Figure 1.2. [Basics of Electrochemical Impedance Spectroscopy, application note Gamry Instruments].

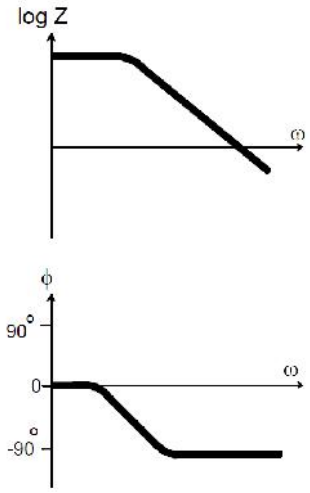

Figure 1.2: Bode plot for a parallel RC circuit. Upper panel displays the complex impedance, Z, in logarithmic scale versus the frequency ω in logarithmic scale. Lower panel displays the phase shift φ versus the frequency ω in logarithmic scale. [Basics of Electrochemical Impedance Spectroscopy, application note Gamry Instruments].

Impedance data are commonly analyzed by fitting them to an equivalent electrical circuit model. The Randlers and Ershler model (Figure 1.3) is very often used to model phenomena associated with effects in an electrochemical cell. This electronic equivalent circuit includes the ohmic resistance of the electrolyte solution, R_s, the Warburg impedance, Z_w, resulting from the diffusion of ions from the solution to the sensor surface, the double layer capacitance, C_{dl}, and the electron transfer resistance, R_{et}, originating when a redox probe is used. Electrochemical impedance spectroscopy (EIS) offers several advantages over the previously described techniques, because the effects of solution resistance, double layer charges and currents due to diffusion or to other processes occurring in the surface-immobilized biological monolayer can be described more precisely by equivalent models. EIS can be used for the real-time measurement of all different electrochemical reactions that occur.

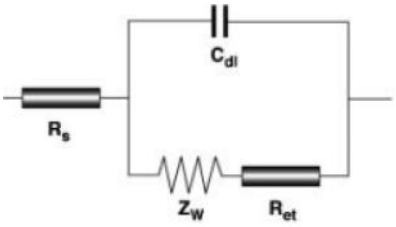

Figure 1.3: General equivalent circuit for modeling EIS measurements in an electrochemical cell. This electronic equivalent circuit includes the ohmic resistance of the electrolyte solution, R_s, the Warburg impedance, Z_w, the double layer capacitance, C_{dl}, and the electron transfer resistance, R_{et} [Basics of Electrochemical Impedance Spectroscopy, application note Gamry Instruments].

Impedimetric detection is primarily used for affinity biosensors. It can be used to monitor immunological binding events or to monitor DNA hybridization or denaturation processes.

The specific binding of an antigen to an antibody-immobilized (semi)conductive sensor surface, will chemically modify the biological interface, altering the impedance of that interface. The formation of an antigen-antibody complex will disturb the dielectric layer at the conductor-liquid interface, resulting in an enlarged thickness and insulation of the electrode surface (Figure 1.4). This will change the double layer capacitance (C_{dl}) and the charge transfer resistance (R_{ct}) [Katz et al., 2003].

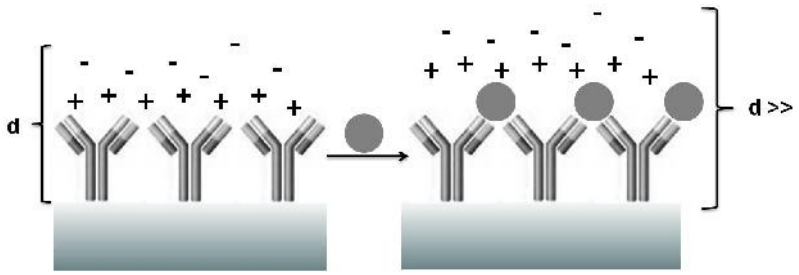

Figure 1.4: Schematic illustration of impedance immunosensing. The interaction between an antigen and an antibody-functionalized electrode increases the dielectric layer thickness and inhibits the interfacial electrochemical processes.

Non-faradaic impedance spectroscopy, in the absence of a redox probe, is used to monitor antigen detection at antibody-functionalized electrode surfaces. For example, Figure 1.5 shows small changes of the real part of the impedance (Z') and the imaginary part of the impedance (Z''), upon the binding of interferon-γ (IFN-γ) with anti-INF-γ antibodies on a Au surface in phosphate buffer. Although the impedance changes were small, kinetic analysis of the antigen-antibody binding was possible [Bart et al., 2005]. Similar impedance measurements were applied for the quantitative determination of bisphenol A in phosphate buffer on antibody-modified glass carbon electrodes [Rahman et al., 2007].

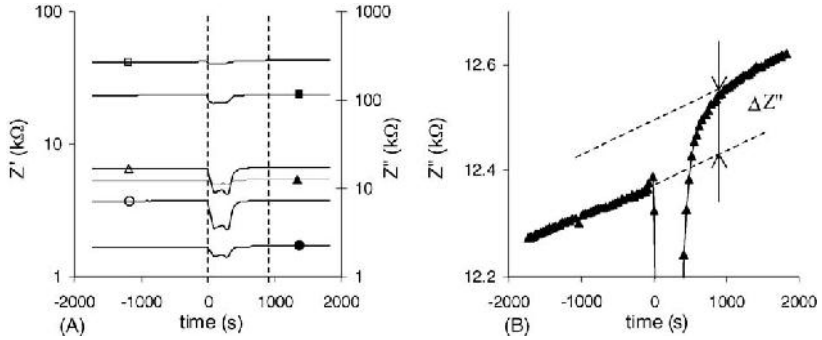

Figure 1.5: Real-time impedance change upon binding of interferon-¥. (A) Typical multi-frequency recording of the sensor impedance before, during and after IFN-γ injection. The real (Z', open symbols, left axis) and the imaginary part of the impedance (Z'', filled symbols, right axis) are plotted on a logaritmic scale vs. time, for selected frequencies: 9 Hz (open and filled squares), 113 Hz (open en filled triangles) and 1017 Hz (open and filled circles). The dashed vertical lines indicate the time of the sample entrance in the cell (t=0 s) and the time at which Z'' is determined (t=900 s). (B) Magnification of the curve of Z'' at 113 Hz, illustrating the baseline corrected small impedance shift (ΔZ''). Sample: 50 µl IFN-γ (130 pM) in 10mM phosphate buffer pH 7.4 at 10 µl/min; E_{ac} = 10mV [Bart et al., 2005].

In order to quantify D-dimer, a deep venous thrombosis marker, the variation of the R_{ct} on antibody-functionalized carbon nanotubes (CNT) was analysed [Bourigua et al., 2010]. The immunosensor calibration curve (Figure 1.6) presents a linear relation between R_{ct} and the logarithmic concenctration of

D-dimer ranging from 0.1pg/mL to 2µg/mL with a detection limit of 0.1pg/mL in phosphate buffer. Comparable impedance measurements, based on the changes in R_{ct}, were performed for the detection of internalin B [Tully et al., 2008] and human serum albumin (hsa) [Cabellero et al., 2012] in phosphate buffer.

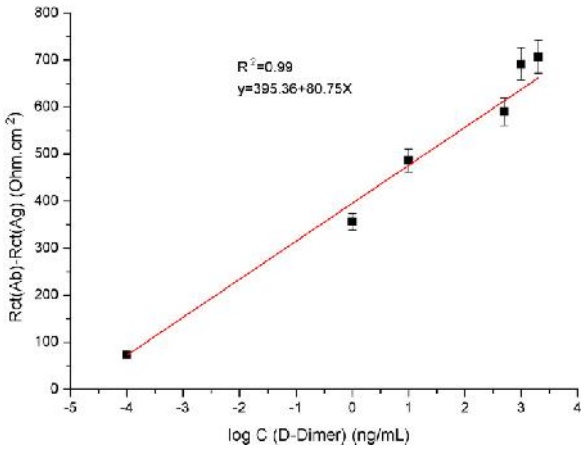

Figure 1.6: Calibration curve describing the variation of charge transfer resistance ΔR_{ct} in function of the logarithmic concentration of D-dimer. [Bourigua et al., 2010]

In 2009, Quershi et al. developed a capacitive biosensor for the detection of C-reactive protein (CRP) using anti-CRP antibodies coupled to interdigitated Au electrodes (GID) on a nanocrystalline diamond (NCD) surface. When CRP interacts with the immobilized antibodies, the thickness of the dielectric layer on the GID-NCD surface will change. This will induce a change in capacitance, which has a linear relation with the CRP concentration ranging from 25 – 800ng/mL in phosphate buffer [Quershi et al., 2009]. In 2010, this sensor was improved to a multi-analyte capacitive sensor for the detection of CRP, tumor necrosis factor α (TNF-α) and interleukin 6 (IL-6). CRP and IL-6 were detected within the range of 25pg/mL to 25ng/mL in phosphate buffer, as shown in Figure 1.7 [Qureshi et al., 2010].

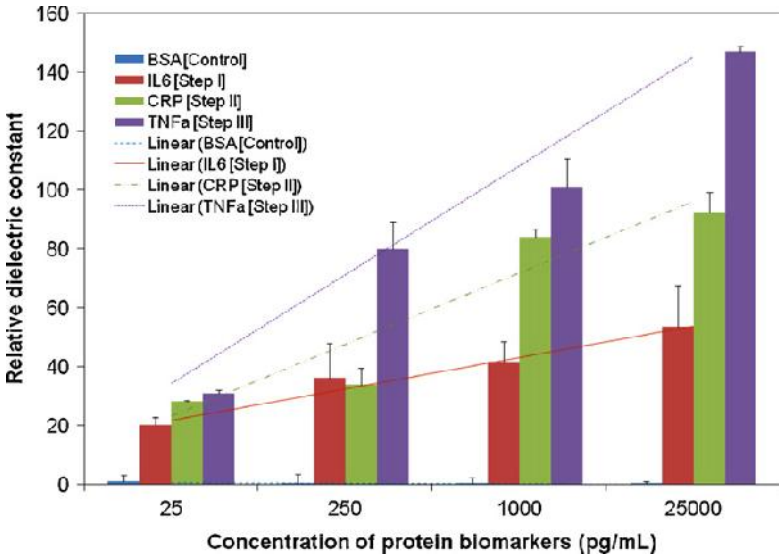

Figure 1.7: Multiplexed detection of protein biomarkers on chips immobilized with an equimolar mixture of anti-CRP, -IL-6 and –TNF~ antibodies. The sensor shows a concentration dependent increase in dielectric response at a frequency of 173 MHz. The coloured lines are derived from a linear fit of the obtained values for the tested proteins. BSA was used as a negative control [Qureshi et al., 2010].

However, to be applicable in clinical diagnostics, the sensitivity and reproducibility of the developed immusensors need to be tested in patient samples, like blood, serum and urine. Vasconcelos et al. constructed an capacitive immunosensor for the detection of cTnT in serum samples. Based on the change in C_{dl} a linear detection range of 0.07 – 6.83ng/mL was obtained [Vasconcelos et al., 2009]. However, the cut off value of cardiac infarction (0.03ng/mL) lies outside the detection range of the sensor. This problem can be addressed by the use of nanostructured surfaces instead of plain electrodes [Lin et al., 2010]. This concept was exemplified by Kunduru et al. with the detection of CRP at polystyrene (PS) nanotextured surfaces. They observed a significant enhancement in signal magnitude due to CRP binding on the PS nanofibers as compared to detection on PS microbeads. A clinical relevant, linear detection range of 1pg/mL to 1µg/mL in serum samples was achieved [Kunduru et al., 2010]. The addition of a redox probe, often $[Fe(CN)]^{-3/-4}$, to the electrolyte solution can possibly increase the sensitivity of the immunosensor. For example,

the interaction of murine double minute 2 (MDM2), a prognostic brain tumor marker, with an Au electrode functionalized with antibodies resulted in a significant insulation of the electrode surface, reflected by a large increase of the R_{ct}. In mouse brain tissue homogenates a detection limit of 1.3pg/mL was obtained [Elshavey et al., 2013]. Another way to enhance the response of a label-free immunosensor is to increase the amount of immobilized antibodies on the electrode. Recently, this enhancement method was investigated by Rezaei et al. by immobilizing antibodies on multilayer Au nanoparticle (AuNP) networks, increasing the electrode surface area. The immunosensor shows ~pg/mL detection limits for human growth hormone (hGH) and insulin-like growth factor 1 (IGF-1) in serum samples, based on the increase in relative R_{ct} [Rezaei et al., 2009 and 2011]. Although the sensor has good sensitivity in serum samples, the antigen incubation times are too long, respectively 2 and 3 hours, to be clinical relevant. Finally, to amplify the impedimetric signal different labels can be used. Hou et al. described an immunosensor with triple signal amplification for the detection of prostate specific antigen (PSA) by using a anti-PSA detection antibody labeled with AuNP, Au-palladium nanotags (AuPd) and DNAzyme. The signal amplification is on one hand based on DNAzyme, that catalyzes the precipitation of 4-choloro-1-naphthol (4-CN) and on the other hand based on AuPd, that provides a large surface coverage for the immobilization of the DNAzyme label. The produced insoluble product precipitates on the electrode surface, and hinders the electron transfer between the solution and the electrode, thereby increasing the impedance [Hou et al., 2014].

Table 1.1. gives a literary overview of all label-free impedimetric immunosensors discussed in this chapter in terms of sensitivity against their target analytes.

Table 1.1: Literary overview of label-free impedimetric immunosensors up to date

Target	Medium	Dynamic range	Reference
IFN-γ	buffer	17.1 - 171ng/mL	[Bart et al., 2005]
BPA	buffer	1 - 100ng/mL	[Rahman et al., 2007]
D-dimer	buffer	0.1pg/mL – 2µg/mL	[Bourigua et al., 2010]
Internalin B	buffer	1 – 100pg/mL	[Tully et al., 2008]
hsa	buffer	0.670 – 6.70fg/mL	[Caballero et al., 2012]
CRP	buffer	25 – 800ng/mL	[Quershi et al., 2009]
CRP IL-6 TNF-α	buffer	25pg/mL – 25ng/mL	[Qureshi et al., 2010]
cTnT	serum	0.07 - 6.83ng/mL	[Vasconcelos et al., 2009]
CRP MPO	serum	1pg/mL – 1µg/mL	[Lin et al., 2010]
CRP	serum	1pg/mL – 1µg/mL	[Kunduru et al., 2010]
MDM2	serum	1pg/mL – 1µg/mL	[Elshavey et al., 2013]
hGH IGF-1	serum	3 – 100pg/mL	[Rezaei et al., 2009]
hGH IGF-1	serum	1 – 180pg/mL	[Rezaei et al., 2011]

The most important driving force for the development of impedimetric DNA-sensors is the possibility of label-free detection. The DNA-sensors described in previous sections mostly require a label, e.g. a redox enzyme. In the case of EIS-based DNA-sensors, changes in the electrical properties of the surface can occur solely due to addition of a target DNA strand. Thus, no label is required for impedimetric DNA sensing. However, since labeling can enhance sensitivity, some impedimetric DNA-sensors described in literature use labels. This will improve the detection limit and preamplificiation of the target DNA by polymerase chain reaction (PCR) can be avoided. However, labeling will also increase the time, complexity and cost. Therefore label-based impedimetric DNA-sensor are not discussed in this dissertation.

Many EIS-based DNA-sensors have been presented in the literature during the last 10 years, either based on faradaic or non-faradaic impedance

spectroscopy. In non-faradaic impedance spectroscopy, usually the capacitance of the double layer formed between the solution and the electrode surface is studied. No additional reagent is required. This is due to the displacement of water and ions from the surface upon biomolecule binding (Figure 1.8) [Seland et al., 2006].

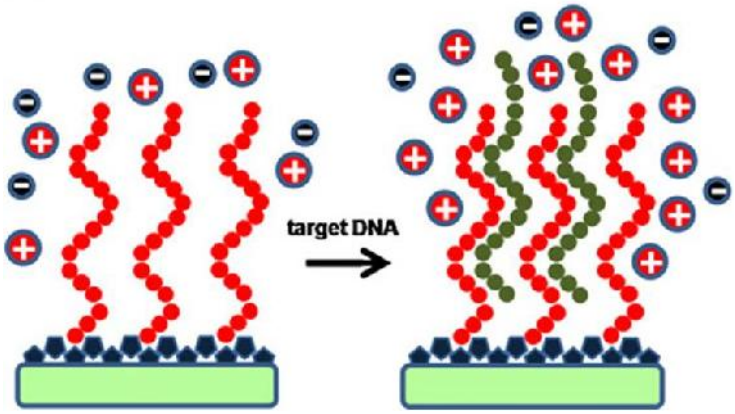

Figure 1.8: Schematic illustration of non-faradaic DNA-sensing. The electrochemical interface properties change after hybridization with target DNA, represented in green [modified from Tosar et al., 2010].

For example, Vermeeren et al. investigated SNP detection on NCD using non-faradaic EIS. Probe ssDNA molecules were covalently attached to carboxyl (COOH)-modified NCD working electrodes. Real-time SNP discrimination was possible during hybridization with complementary, 1-mismatch and non-complementary 30-mer target ssDNA at low frequencies (~1000 Hz). A decrease of the impedance was observed when the complementary target DNA was added, while the addition of 1-mismatch target ssDNA caused no significant impedance change (Figure 1.9).

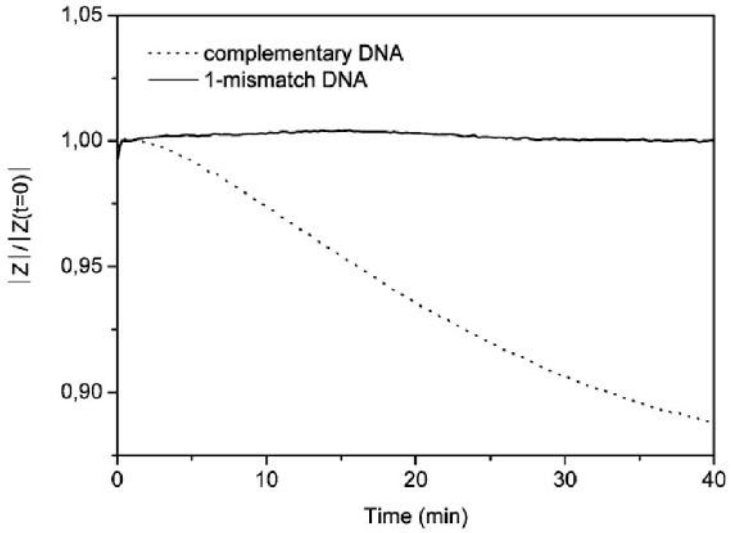

Figure 1.9: Real-time hybridization curves at 1150Hz. The modulus of Z is normalized to the value immediately after adding the target ssDNA (t=0) [Vermeeren et al., 2007].

A non-faradaic impedance-based DNA hybridization sensor for breast cancer was reported by Mohan et al. A glassy carbon electrode, modified with a conducting polymer, was functionalized with 19mer ssDNA probes. A linear detection range from 5.97ag/mL – 59,7ng/mL was obtained after hybridization with target ssDNA for an optimal time period. The described technique is able to detect a single base mutation in a BRCA1 related sequence based on a difference in R_{ct} between single base mismatch and complementary strands [Mohan et al., 2010].

However, to be applicable in clinical diagnostics, the performance of the developed DNA-sensors needs to be evaluated with real patient DNA samples (genomic DNA or PCR amplified DNA fragments). Davis et al. constructed an impedimetric DNA hybridization sensor for differentiating between different gene sequences. Screen-printed carbon electrodes modified with conducting polymer were used to immobilize ssPCR fragments from plasmid DNA of the pyruvate kinase gene. A large drop in impedance was measured upon exposure to complementary ssDNA targets in a concentration range from 1 fg/mL to 1 ng/mL. SNP-sensitivity was not investigated [Davis et al., 2007]. Booth et al.

studied the effect of the length of DNA probes and target strands on the performance of the DNA-sensor. Increased response was observed upon hybridization of longer complementary target ssDNA, because longer strands are associated with more negative charges [Booth et al., 2011]. Baccar et al. developed an impedimetric DNA-sensor for the detection of 80b long ssDNA sequences on layered double hydroxide nanomaterials. A dynamic range of 18 – 270 ng/mL was achieved for complementary sequences. SNP-sensitivity was not investigated [Baccar et al., 2012].

The addition of a redox probe to the bulk solution can possibly increase the sensitivity of a DNA-sensor for patient-derived DNA samples. The redox probe is alternatively oxidized and reduced at the working (semi)conductive electrode surface. During this process a variation in charge transfer resistance between the solution and the electrode surface can be observed. The redox probe is considered as a marker, not as a label, since it is indirectly related to the biorecognition event. In the case of DNA-sensors, negatively charged redox probes are usually employed. In fact, since DNA is a polyanionic molecule, hybridization generates a repulsion of the redox probe, thus inhibiting the redox reaction and enhancing the charge transfer resistance value (R_{ct}) (Figure 1.10) [Katz et al., 2003]. For example, Baur et al. presented a faradaic DNA-sensor for the detection of HIV. The sensor consists of a poly(pyrrole-nitrilotriacetic acid) film modified with Cu^{2+} ions for the immobilization of histidine-tagged ssDNA. In the presence of hydroquinone, a neutral redox probe, a linear quantificiation of a 48-mer HIV DNA target in the range of 14.1fg/mL – 1.4ng/mL was possible based on an increase in R_{ct} [Baur et al., 2010]. Pandey et al. reported a DNA-sensor based on cystine dendrite structures on Au electrodes. In the presence of $[Fe(CN)6]^{3-/4-}$, a linear response to complementair E. Coli-specific target DNA in the concentration range of 50pg/mL to 5.00mg/mL was achieved. No cross-reactivity towards other water-borne pathogens like Salmonella typhimurium, Neisseria meningitides, and Klebsiella pneumonia was detected [Pandey et al., 2011].

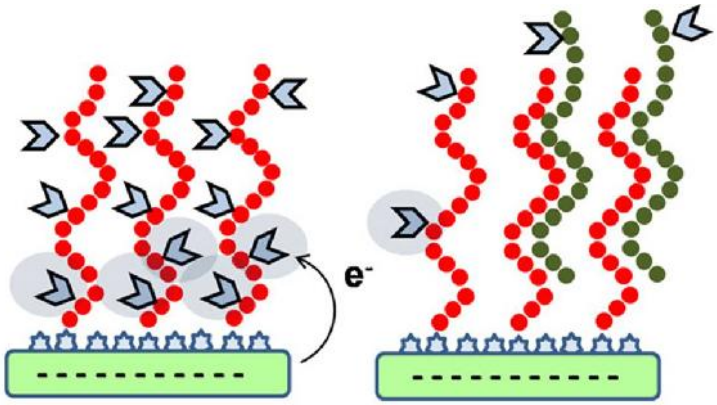

Figure 1.10: Schematic illustration of faradaic impedimetric DNA-sensing. The charge transfer resistance will change after hybridization, due to repulsion of the redox probe (blue arrowheads) by the target DNA molecules. Probe DNA is shown in red, and complementary target DNA is represented in green [Tosar et al., 2010]

SNP detection of previously described impedimetric DNA-sensors is based on the difference in hybridization efficiency. Alternatively, single base mutations can be detected based on the difference in the denaturation rate of dsDNA containing a SNP or not. For example, the previously described DNA-sensor developed by Vermeeren et al. Showed also SNP sensitivity during the chemical denaturation of 30-mer dsDNA fragments with NaOH. Denaturation of complementary dsDNA showed the longest exponential impedance decay time, while the decay time during the denaturation of SNP-containing dsDNA was shorter (Figure 1.11) [Vermeeren et al., 2007]. However, in general it is not easy to fine tune chemical denaturation to identify mismatches that have comparable melting temperatures. NCD can be used as a temperature regulator for thermal denaturation [Clukers et al., 2010]. However, impedance spectroscopy is not the ideal read-out for thermal denaturation, because it is sensitive to temperature changes.

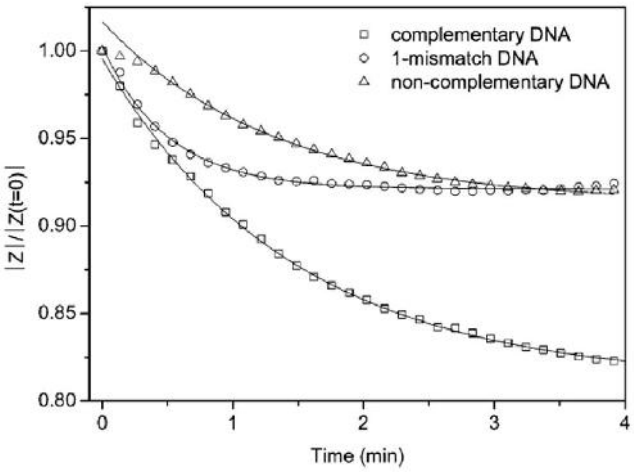

Figure 1.11: Real-time denaturation curves at 1MHz for complementary, 1-mismatch or non-complementary dsDNA. The modulus of Z is normalized to the value immediately after NaOH addition (t=0 min). The solid lines indicate fits using an exponential decay function [Vermeeren et al., 2007].

1.3 Nanocrystalline diamond: an alternative transducer material in biosensor applications

Most of the traditional transducer materials like glass, polystyrene, carbon electrodes, Au and Si do not have all the desired properties for biosensor applications. For example, Si and Au show degradation of the attached biological layer in electrolyte solutions. Diamond is an attractive substrate for electrochemical biosensor applications, because it has good electronic and chemical properties. For example, diamond has a larger electrochemical potential window and a lower background current as compared to other commonly used electrode materials. In addition, diamond is known to be chemically inert, so it does not degrade upon contact with electrolyte solutions. Moreover, the carbon composition of diamond allows strong carbon bonds with biological molecules. Furthermore, diamond is biocompatible, allowing in vivo applications [Qureshi et al. (review) 2009]. Finally, diamond has a high thermal conductivity and a low thermal expansion. Therefore, diamond can be used as a temperature regulator for sensing applications [Clukers et al., 2010].

1.3.1 Diamond growth

Because of the useful electronic and chemical properties of diamond, discussed in the section above, different methods for the synthesis of NCD were developed. These methods can improve the high costs and the low abundance of naturally occurring diamond, encouraging the use of diamond in technological applications. Two main procedures have been developed for the synthesis of diamond. The first technique is called High Pressure-High Temperature (HPHT) and mimics the natural process for the production of diamond from graphite. This technique provides a reliable way to produce synthetic diamond, but requires metal solvents during the production. Therefore, traces of metal are often found in the diamond end product, limiting possible applications. For that reason a low pressure, low temperature method was developed, called Chemical Vapour Deposition (CVD). CVD processes include Hot Filament CVD (HFCVD), Direct Current Plasma CVD (DCCVD), Microwave Plasma Enhanced CVD (MWPECVD). These processes involve the deposition of carbon atoms, originating from a carbon-containing gas, in the presence of a large quantity of atomic hydrogen (H_2). Using CVD, it is possible to deposit thin films of diamond on various substrates. These substrates can be bulk diamond or non-diamond, like Si, resulting in either single-crystalline diamond (SCD) or polycrystalline diamond (PCD) films. PCD films are microcrystalline, nanocrystalline or ultrananocrystalline, according to the average grain size and macroscopic properties [Williams et al., 2008; Vermeeren et al., 2009; Gracio et al., 2010]. Only NCD is used in the biosensor applications described in Chapters 3-6, and therefore this introduction focuses on the properties, functionalization and biosensor applications of NCD.

NCD films have grain sizes ranging from a few nanometers up to a hundred nanometers and very low (0.1 %) to high (50 %) amounts of sp^2-bonded carbon, in the form of defects or grain boundaries [Gracio et al., 2010]. A SEM image of a NCD film on a Si substrate is shown in Figure 1.12.

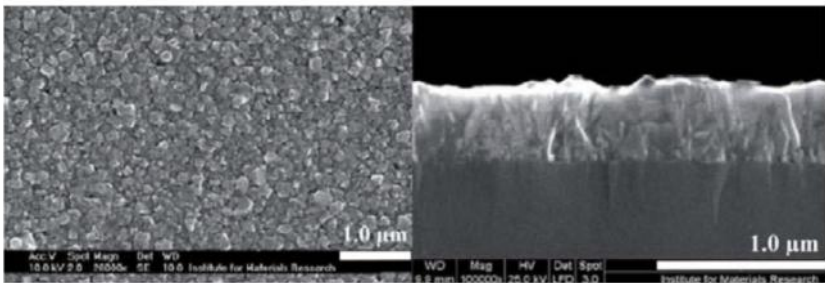

Figure 1.12: SEM images of an NCD film on Si. The left panel shows a topographical view of the NCD film. The nm grain sizes are clearly visible. The right panel shows a cross-section of the thin NCD layer on top of the Si. [Vermeeren et al., 2009]

Intrinsic or undoped NCD has insulator-like properties, like a very wide bandgap at room temperature. However, NCD can be made semiconductive by either p-type (conduction via holes) or n-type (conduction via electrons) doping. P-type doping can be obtained by the addition of boron to the plasma during growth of the NCD films [Vermeeren et al., 2009]. N-type-doped NCD films can be accomplished through the addition of phosphor [Vermeeren et al., 2009] or nitrogen gas [Qureshi et al., 2009].

1.3.2 Biofunctionalization of nanocrystalline diamond

Yang et al. (2002) demonstrated the covalent attachment of short, synthetic, thiolated (SH) ssDNA to a hydrogenated NCD (NCD:H) surface by a photochemical process, as illustrated in Figure 1.13. Firstly, H-terminated NCD surfaces were covered with trifluoro-acetamide (TFAAD) under UV illumination. Next, the trifluoro-acetic groups were removed in a hydrochloric (HCl)/methanol solution, forming amino (NH_2)-modified NCD surfaces. Subsequently, the heterobifunctional cross-linker molecule SMCC was bound to the NH_2-modified NCD surface. Finally, SH-modified ssDNA molecules were linked to the COOH-group of the SMCC molecules. The activity of the immobilized ssDNA molecules was verified by the fluorescent detection of hybridization with complementary target ssDNA.

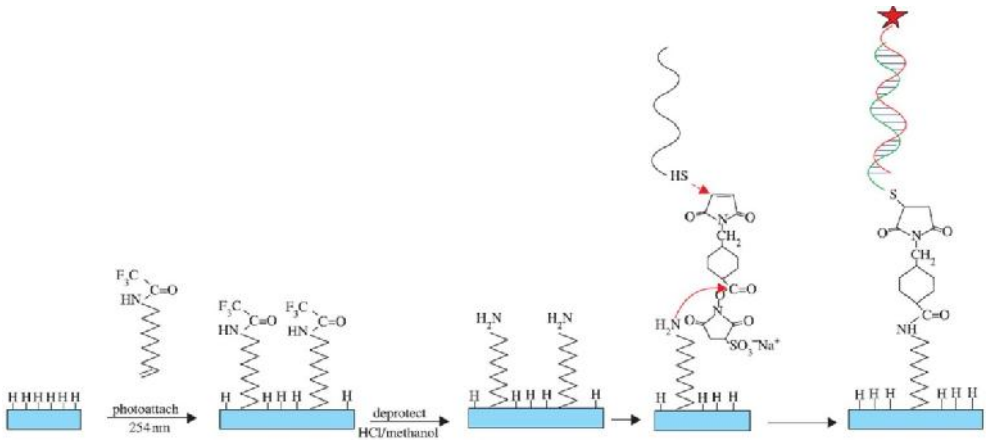

Figure 1.13: Photochemical attachment scheme developed by Yang et al. First, NH_2-containing molecules are photochemically and covalently attached to NCD:H. The linker molecules are then deprotected and reacted with a heterobifunctional cross-linker and thiol-modified ssDNA [Nebel et al., 2007].

The photochemical attachment procedure developed by Yang et al. uses cross-linker molecules to attach biomolecules to the NCD surface. Christiaens et al. developed a two-step photochemical method for the covalent attachment of NH_2-modified dsDNA onto NCD surfaces, using a zero-length cross-linker (Figure 1.14). In the first step, a H-terminated NCD surface is reacted for 20 hours under 254 nm UV light with omega-unsaturated fatty acid molecules (10-undecenoic acid), yielding a COOH-modified NCD (NCD:COOH) for further reaction. In the second step, a zero-length cross-linker 1–ethyl–3-(3-dimethylaminopropyl)-carbodiimide (EDC) is applied to establish a covalent bond between the COOH-groups on the diamond surface and the NH_2-modified DNA molecules. This two-step method is easy, reproducible, and highly efficient. Furthermore, the EDC cross-linker does not remain present in the formed amide (NH) bond, resulting in a smaller distance between the DNA molecules and the NCD surface. The functionalization of the dsDNA molecules was verified with PCR and gelelectrophoresis [Christiaens et al., 2006]. In 2008, this method was optimized for the covalent attachment of short, synthetic NH_2-modified ssDNA molecules. The functionalization and the activity of the functionalized ssDNA molecules was verified by fluorescence microscopy [Vermeeren et al., 2008].

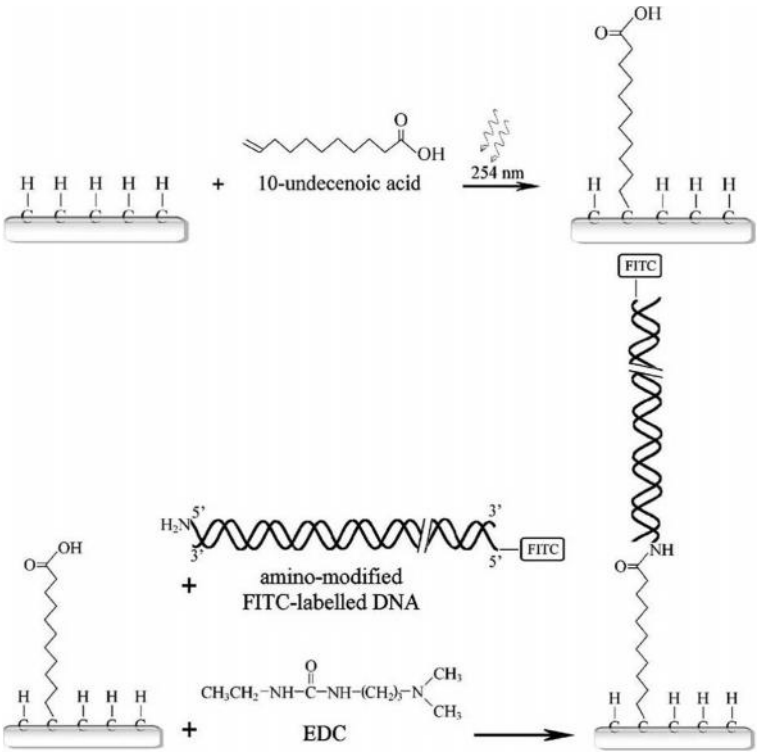

Figure 1.14: Two step photochemical attachment scheme developed by Christiaens et al. First, 10-undecenoic acid is attached to NCD:H through irradiation with 254 nm UV light. Second, NH_2-modified dsDNA is covalently attached to the fatty acids on the NCD substrate using an EDC-mediated reaction [Christiaens et al., 2006].

Similar immobilization chemistries can be used for the covalent attachment of proteins, including enzymes and antibodies, on NCD surfaces. A summary of protein-modified NCD surfaces can be found in the reviews written by Härtl et al. and Stavis et al. [Hartl et al., 2004; Stavis et al., 2011]. However, in our study we used physical adsorption of antibodies onto H-terminated NCD for the impedimetric detection of CRP [Vermeeren et al., 2011 and Chapter 6]. For that reason, the covalent immobilization strategies for proteins on NCD surfaces will not be discussed in the introduction, but in the general discussion in Chapter 7.

1.4 Problem statement and objectives

As stated in the beginning of this introduction, the demand for point-of-care diagnostics is growing. Because point-of-care diagnostics relies on essential features like fast result, low cost, reliability and sensitivity, there is a worldwide interest in the development of fast and inexpensive miniaturized and automated devices, called biosensors.

Different types of biological recognition molecules can be combined with numerous transduction principles, offering a wide diversity in biosensor specificity. A suitable detection principle needs to be selected for each application. Furthermore, diverse materials can be used as transducer substrate. However, not all transducer materials are compatible with each type of transduction principle, e.g. electrochemical transduction requires semiconducting transducers. The choice of a specific transduction principle largely depends on the type of application. In clinical applications, important features are speed, reliability and cost. Faster results can be obtained by eliminating time consuming steps and by real-time monitoring of the experiment. Accuracy, precision, sensitivity and specificity are the cornerstones of the test reliability. These indicators need to be thoroughly tested for each developed biosensor. Accuracy and precision can be enhanced by automating the process and so reducing variation induced by human manipulation. High costs, reflected by the required equipment and consumables, can be reduced by using transduction principles that do not need expensive labels and that can be combined with low cost equipment.

Because this dissertation focuses on the development of biosensors with fast, label-free and real-time detection, the indirect optical transduction principles, like colometry and fluorescence, will not be considered as detection principle of our biosensor. The direct optical transduction principle SPR is capable of real-time and label-free analyte detection. However, state-of-the-art SPR devices, like Biacore™ T200, require expensive and sophisticated benchtop lab equipment as read-out instrumentation. QCM, using piezoelectric transduction, is temperature sensitive and can not be easily modified to multi-analyte detection. Biosensors using electrochemical transduction are generally considered to have a low production cost, the possibility for real-time detection

and the simplicity to miniaturize. However, amperometry, potentiometry and conductimetry, usually require enzymatic labels to reach clinically relevant sensitivity. On the other hand, electrochemical impedance spectroscopy can be used for the real-time and label-free monitoring of binding events on sensor surfaces.

Considering the advantages and disadvantages of above mentioned transduction principles, EIS is best fitting the essential features of point-of-care diagnostic devices. In EIS-based transduction, semiconductive electrode materials are used, such as Si and Au. However, the chemical linkage between Si/Au and biological recognition molecules is weak and unstable in electrolyte solutions, causing degradation of the attached biological layer. This may have a negative effect on the reliability of the biosensor. Diamond is an attractive alternative substrate for EIS-based biosensor applications, because the carbon composition of diamond allows strong covalent carbon bonds with biological recognition molecules. Moreover, diamond has good electronic properties like a larger electrochemical potential window and a lower background current, as compared to Si and Au. In addition, diamond has a high thermal conductivity and a low thermal expansion. Moreover, synthetically grown diamond combined with an inexpensive read-out equipment, such as an impedimetric setup does fit our criteria for a suitable platform to develop clinical relevant or point-of-care applications.

At the start of this PhD project, the impedimetric NCD-based DNA-sensors described in literature had the drawback of not displaying real-time information or no tests were performed on patient-derived samples. For example, Yang et al. developed an impedimetric, NCD-based DNA-sensor for the monitoring of selective DNA hybridization. A clear difference in impedance upon hybridization with complementary target DNA and 4-mismatch target DNA was detected, using a redox marker [Yang et al., 2004]. The first biosensor describing real-time information on the difference in denaturation kinetics of complementary and mismatched DNA was described by Vermeeren et al. in 2007. However, SNP-sensitivy in patient-derived DNA samples was not shown. Also, the impedimetric NCD-based immunosensors described in literature do not meet all the required properties of an ideal diagnostic device. For example, the impedimetric NCD-based immunosensor developed by Yang et al. for the

detection of IgG and IgM is not clinical relevant due to the manner of antigen recognition [Yang et al., 2007]. The impedimetric immunosensor developed by Quershi et al. (2009), has a clinicical relevant concentration range in buffer solutions [Quershi et al., 2009]. However, clinical relevance in serum samples is not investigated.

Taken together, the main goal of this dissertation is to develop diamond-based sensor platforms for the detection of clinically relevant DNA point mutations and protein biomarkers. Important objectives were to obtain a DNA-sensor offering denaturation-based, SNP-sensitivity in patient-derived samples and a selective immunosensor capable of measuring physiologically relevant concentrations of the target molecule in patient-derived samples. Both sensor platforms should make use of real-time and label-free detection principles. In order to reach these striving objectives, milestones were set and following research questions were formulated:

a. Can an automated DNA-sensor platform be developed to measure the differences in denaturation kinetics in complementary DNA strands and DNA strands containing clinically relevant single base mismatches?

b. Can this prototype be used to identify clinically relevant point mutations in patient-derived, exon-size DNA fragments?

c. Can an electrochemical immunosensor platform be developed to selectively detect a clinically relevant target molecule? And is it possible to detect it in a physiologically appropiate concentration range?

d. Can this prototype also be used to measure the target molecule in a clinically relevant concentration range in patient-derived serum samples?

In order to answer these research questions, the following topics were investigated. These topics also define the outline of the different chapters in this dissertation.

a. In order to develop a DNA-sensor platform in which denaturation-based SNP-sensitivity is reached, the two following strategies will be applied. A first approach, described in Chapter 3, involves SNP detection using chemical denaturation in an automated EIS-based sensor. Alternatively, thermal denaturation could allow fine tuning of the DNA denaturation process and therefore could increase the kinetic information collected during DNA denaturation, important for the sensitivity of the SNP detection. However, EIS is known to be sensitive for temperature changes and therefore a novel type of sensing principle, based on heat-transfer resistance, will be introduced. The results of the second approach are described in Chapter 4.

b. To demonstrate a possible proof of application for the developed prototype DNA-sensor, PKU patient-derived exon-size DNA fragments will be used. First, the maximum DNA length, where the developed DNA-sensor is still sensitive to SNPs, will be determined. Furthermore, the detection of common SNPs in the PAH gene, associated with PKU, will be studied. These results are described in Chapter 5.

c. To address the applicapibility of an EIS-based sensor platform for the detection of proteins, an immunosensor platform will be created for the detection of CRP. To demonstrate the specificity of the EIS-based immunosensor, EIS-based CRP detection was compared to detection of plasminogen. The sensitivity of this sensor will be assessed by measuring the EIS effect of different clinically relevant CRP concentrations in buffer and in CRP-spiked serum samples. These results are described in Chapter 6.

2

MATERIALS AND METHODS

This section gives an overview of the physiological solutions and chemicals, sensor setups and experimental procedures used in the following chapters.

2.1. Physiological solutions and chemicals

Sodium dodecyl sulphate (SDS) was obtained from VWR International (Zaventem, Belgium). 10-undecenoic acid (10-UDA) was bought from Sigma-Aldrich (Bornem, Belgium). 1-ethyl-3-(3-dimethylaminopropyl)-carbodiimide (EDC) and 2-(N-morpholino)ethanesulfonic acid (MES) were purchased from Perbio Science (Erembodegem, Belgium). PCR buffer was bought from Roche Diagnostics (Vilvoorde, Belgium). Sodium Hydroxide (NaOH) and acetic acid (HCl) were acquired from Merck (Overijse, Belgium). Bovin serum albumin (BSA) was bought from Immunosource (Halle-Zoersel, Belgium). Taq-DNA polymerase (5U/µl) was bought from Roche Diagnostics (Vilvoorde, Belgium). An ELISA amplification system based on the cyclic redox reaction of NADH/NAD^+ was obtained from Invitrogen (Merelbeke, Belgium). C-reactive protein (CRP), unlabeled and alkaline phosphatase (AP)-labeled anti-CRP monoclonal antibodies and plasminogen were synthesized by Scipac (Kent, United Kingdom). Quantification of the CRP levels in human serum was performed in Labo Rigo (Genk, Belgium) by a turbidimetric assay, which indicated a CRP concentration well below 4 nM. All primers and DNA-sequences were purchased from Integrated DNA technologies (Leuven, Belgium). Following buffers were homemade: phosphate buffered saline (1×PBS) (129 mM NaCl; 5mM Na_2HPO_4.2 H_2O and 1.5 mM KH_2PO_4), pH 7.2; 20 mM tris(hydroxymethyl)aminomethane (TRIS) buffer, pH 8; c-reactive protein (CRP) buffer (0.28 M NaCl; 0.09 % NaN_3 and 5 mM $CaCl_2$), pH 8; coating buffer (14 mM Na_2CO_3; 35mM $NaHCO_3$ and 3mM NaN_3); conjugation buffer (1x PBS and 0.05 % Tween 20), pH 7.2; sodium chloride/sodium citrate (2×SSC) buffer (300 mM NaCl and 30 mM $C_6H_8O_7$.3Na), pH 7.5; TRIS buffered saline (1×TBS) (50 mM TRIS base; 150 mM NaCl), pH 7.6.

2.2 Sensor setup and experimental procedures

This section gives an overview of the different sensor setup and the standardized protocols used in the following chapters. The techniques performed by experts are briefly summarized.

2.2.1 Synthesis, cleaning, hydrogenation and carboxylation of NCD

NCD films were prepared by microwave plasma-enhanced chemical vapour deposition (MW PE-CVD) from 0.5% methane/hydrogen mixtures in an ASTeX reactor as described in [Williams et al., 2008]. The substrates were 2-inch Si wafers (thickness 500 – 550 µm, crystalline orientation (100), p-type doped with phosphorus and resistivities from 1 to 20 Ωcm), which were diced into samples of 10 mm by 10 mm after deposition. The diamond layers had a thickness of 100 nm with an average grain size of 50 nm as determined by X-ray diffraction and atomic force microscopy. To ensure a good electrical conductivity of the diamond layer (in the order of 1 Ωcm), the CVD deposition was done with an admixture of trimethyl borane ($B(CH_3)_3$) to the CH_4 gas with a boron concentration between 10^{-19} – 2 x 10^{-20} cm^3. The as-prepared diamond samples were hydrogenated in H_2 plasma (50 Torr, 800 °C, power 4000 W, duration of 14 min). The hydrogenated NCD (NCD:H) samples were used as substrate for the adsorption of antibodies in Chapter 6. For the covalent attachment of DNA fragments in Chapter 3, 4 and 5, 10-undecenoic fatty acid was photochemically attached to the NCD:H samples by UV illumination (wavelength 254 nm, intensity 265 mW/cm²) during 20 hours under a protective N_2 atmosphere. After this photochemical treatment, the samples were thoroughly rinsed in acetic acid at 100 °C to remove unbound fatty acid fragments. Diamond growth was performed by Dr. Stoffel Janssens, hydrogenation was done by Drs. Weng Siang Yeap and carboxylation was carried out by Dr. Lars Grieten or Dr. Mohammed Sharif Murib.

2.2.2 NCD functionalization

For all experiments described in Chapter 3, 4 and 5, amino (NH_2)-modified probe ssDNA fragments were covalently immobilized onto carboxyl (COOH)-terminated nanocrystalline diamond (NCD) sensor electrodes, hereafter referred to as NCD:COOH, using carbodiimide coupling. First NCD surfaces were incubated with a mixture of 65.8µg/mL probe DNA and 20mg/mL EDC in a 25mM MES solution, pH 6, for 2 hours at 4 °C. Non reacted probe DNA was then rinsed off by washing the samples for 30min in 2× SSC buffer with 0.5 % SDS at RT. The immobilized

probe DNA sequences were hybridized by incubating the samples for 2 hours with 263µg/mL of target DNA fragments in 10× PCR buffer at a sequence specific annealing temperature. During hybridization, the samples were kept under a saturated water vapour atmosphere to avoid evaporation of the reaction fluid. After hybridization, unbound DNA was removed by rinsing the samples for 30 minutes with 2× SSC buffer containing 0.5 % SDS at (30min, room temperature). To remove incompletely hybridized DNA, the samples were subsequently rinsed with 0.2× SSC buffer at a sequence specific stringency temperature.

For the experiments described in Chapter 6, anti-CRP monoclonal capture antibodies were physisorbed onto NCD:H. Therefore the NCD:H samples were immersed in coating buffer containing 3µg/mL antibodies for 2 hours at 37 °C. The anti-CRP coated NCD samples were subsequently incubated overnight in a 6 % BSA solution in 1x PBS, to block the remainder of the NCD surface that was not coated with anti-CRP. Also, NCD:H samples treated only with 6 % BSA but without anti-CRP antibodies were used as a control.

2.2.3 Confocal fluorescence microscopy

A Zeiss LSM 510 META Axiovert 200 M laser scanning confocal fluorescence microscope (Carl Zeiss Meditec AG, Jena, Germany) was used for measuring the fluorescence intensities of NCD samples functionalized with Alexa Fluor® 488-labeled DNA (Chapter 3,4 and 5) or antibodies (Chapter 6) (Extinction: 495nm, Emission: 519nm). To excite the Alexa Fluor® 488 dyes a 488nm argon-ion laser was used with a maximum intensity at the sample surface of 1.00 ± 0.05mW. Spurious 514nm light passing through the Acousto Optical Tunable Filter (AOTF) was blocked by a 488/10nm interference filter placed in front of the coupling fiber optics. Confocal optics included a 490nm dichroic mirror and a 500-550nm emission filter. All images were collected with a 10x/0.3 Plan Neofluar air objective with a working distance of 5.6mm. The image size was 512x512 pixels or 128x128 pixels corresponding with a total scanned area of respectively 500 µm x 500 µm or 225 µm x 225 µm. The pinhole size was 150µm and the laser intensity was set at 10 %. The detector gain, being a measure for the multiplier voltage in arbitrary units, varied between 850 and 1200. In order to demonstrate

that the fluorescence intensity originates from the Alexa Fluor® 488 dyes and not from the underlying diamond layer, bleaching experiments were performed. During photobleaching, the laser intensity was set to 100 % for 3 minutes. Images were collected using the AIM Zeiss software and were processed using the ImageJ software (National Institute of Health, Bethesda, MD).

2.2.4 Enzyme linked immunosorbent assay

To verify the formation of the anti-CRP/CRP-complex, 3µg/mL of unlabeled anti-CRP capture antibodies and 6 % BSA were coated on two H-terminated NCD samples using the method described above, in section 2.2.2. One NCD sample was subsequently incubated with 0,3mg/mL of CRP, while the other was treated with CRP buffer without CRP. After two hours of reaction, detection occurred through the incubation with 0,105µg/mL AP-labeled anti-CRP antibodies in conjugation buffer for one hour, and a subsequent substrate reaction using an ELISA amplification system based on NADPH. This substance is transformed by AP to NADH, which is the substrate for a secondary enzymatic redox cycle. Diaphorase oxidizes NADH to NAD^+ while reducing a tetrazolium salt to an intensely colored formazan dye. Subsequently, while ethanol is oxidized by alcohol dehydrogenase, NAD^+ is again reduced to NADH, driving the cyclic behavior of the amplification reaction. After several minutes, the reaction liquid was removed from the surface of the NCD samples with a micropipette, and transferred into the wells of a microtiter plate. This microtiter plate was subsequently placed inside an ELISA reader, and the absorption of the colored product was measured at 405nm. To examine the adsorption of CRP molecules and AP-labeled anti-CRP antibodies to unmodified NCD, two H-terminated samples that were not coated with anti-CRP but only blocked with 6 % BSA were also treated with CRP and CRP buffer, respectively.

2.2.5 Sensor setup

The sensor setup used in Chapter 3 is shown in Figure 2.1. This experimental setup consists of impedance spectroscopy unit and a syringe system coupled to a Perspex flow cell with an inner volume of 110µl. The NCD working electrode is sealed with an O-ring, resulting in an effective area of $28 mm^2$ exposed to the liquid. The counter electrode is a Au wire (diameter 500µm, oriented

perpendicular to the flow direction) at a distance of 1.7mm from the surface of the working electrode. The working electrode is pressed with the Si backside on a copper lid, serving as back electrode. The cell is equipped with a quartz-glass bottom, enabling simultaneous fluorescence imaging with an inverted confocal fluorescence microscope. The syringe system comprises two identical programmable syringe pumps (ProSense, model NE-500, The Netherlands) enabling flow rates of 0.73µl/hour to 1699mL/hour. One syringe serves for administering a 0.1M NaOH solution, the other delivers a 1× phosphate buffered saline (PBS) solution. Both are connected to a computer-controlled three-way valve.

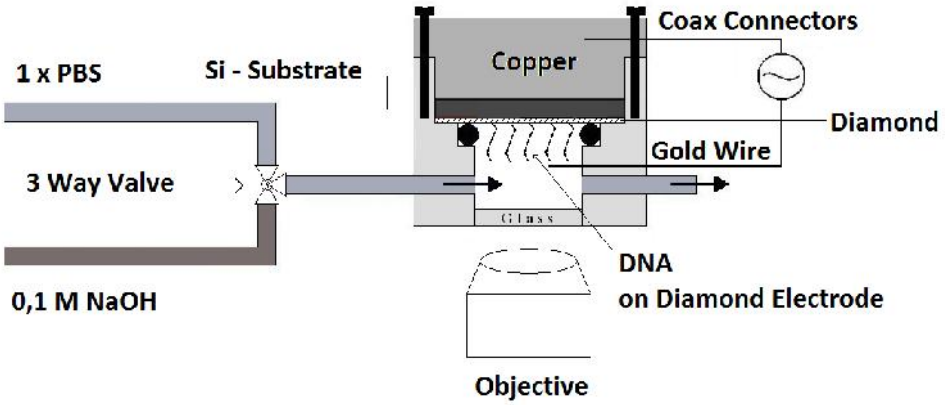

Figure 2.1: Schematic layout of the impedimetric flow cell.

For the heat-transfer measurements described in Chapter 4 and 5, the sensor setup described in Figure 2.1 is adapted as shown in Figure 2.2. The device was now equipped with two miniaturized thermocouples (type K, diameter 500 µm, TC Direct, The Netherlands) monitoring the temperature T_1 of the copper backside contact and the liquid temperature T_2 at a position in the center of the flow cell at 1.7mm above the chip surface. The heat flow was generated with a power resistor (22 Ω, MPH 20, Farnell, Belgium) glued onto the copper block with heat-conductive paste and tightly fixed with a screw. To regulate T_1, the thermocouple signal was led to a data acquisition unit (Picolog TC08, Picotech, United Kingdom) and from there processed into a PID controller

(parameters: P = 10, D = 5, I = 0.1). The calculated output voltage was sent via a second controller (NI USB 9263, National Instruments, USA) to a power operational amplifier (LM675, Farnell, Belgium) and fed into the power resistor. Sampling of the T_1 and T_2 values was done at a rate of one measurement per second.

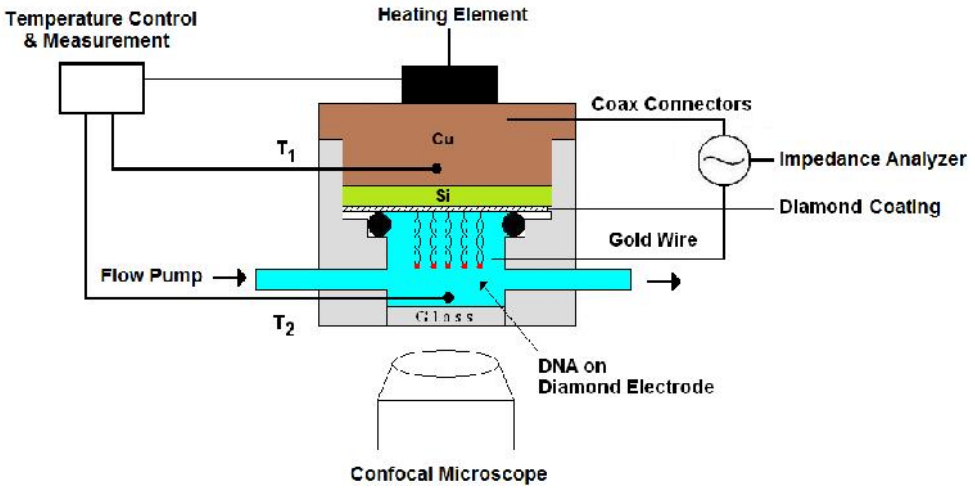

Figure 2.2: Schematic layout of the temperature controlled flow cell.

The sensor setup devised for the development of a CRP-sensitive immunosensor in Chapter 6 is displayed in Figure 2.3.

Four separate NCD samples of 1cm^2 coated with anti-CRP antibodies, functioning as working electrodes, were mounted on a copper (Cu) back contact using silver (Ag) paste. Rubber O-rings with a diameter of 6mm and an acrylic glass lid containing circular openings of equal size were pressed onto the samples to create four reaction wells above the NCD samples.

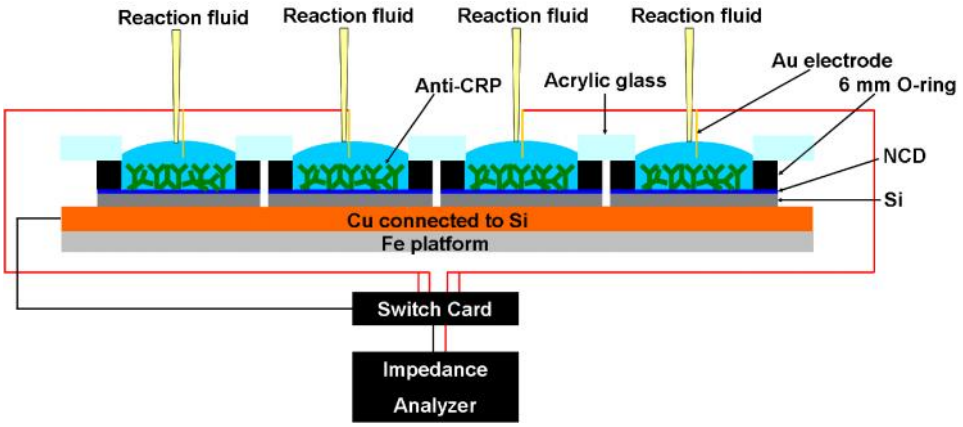

Figure 2.3: Schematic diagram of the immunosensor setup. The sensor houses four anti-CRP-functionalized NCD samples, allowing the simultaneous measurement of four conditions.

Each well was filled with reaction fluid. Au wires, placed ~1mm above each NCD surface and in contact with the reaction fluid, were used as counter-electrodes. Working and counter-electrodes were connected to the impedance analyzer with shielded cables. Hence, four signals were recorded simultaneously. Experiments were performed at 37 °C, by placing the sensor setup inside a humidity-controlled oven, which also provided electromagnetic shielding.

2.2.6 Electrochemical impedance spectroscopy

In Chapter 3 and 4, electrochemical impedance spectroscopy (EIS) was measured using a impedance spectroscopy unit constructed by and described in van Grinsven et al., 2010. The impedance spectroscopy unit measures the impedance in a frequency range of 100Hz to 100kHz built up logarithmically with 10 frequencies per decade and a scanning speed of 5.7s per sweep. The amplitude of the AC voltage was fixed to 10mV. All data discussed in Chapter 3 refer to a frequency of 10kHz and in Chapter 4 of 1kHz.

In Chapter 6, EIS was performed using a Hewlett Packard 4194A Impedance/Gain-Phase Analyzer (Agilent, Diegem, Belgium). The impedance is measured by applying an AC potential (U) of 10mV to the measurement cell. The response to this potential is an AC current signal (I). The complex

impedance (Z) was measured for 50 frequencies, equidistant on a logarithmic scale, in a frequency range from 100Hz to 1MHz. The duration of one complete frequency sweep per channel was 8 seconds. A Keithley 7001 switch card (Keithley Instruments, B.V., Sint-Pieters-Leeuw, Belgium) was used to switch between the four channels after each frequency sweep.

Real-time impedance curves from anti-CRP-functionalized or BSA-functionalized NCD samples mounted into the above described setup were recorded continuously during stabilization in buffer before antigen addition, antigen addition, and rinsing. The reaction wells were first filled with pure (1× or 0.1×) PBS buffer, and the device was allowed to stabilize until the difference in Z between two successive frequency sweeps was negligible throughout the entire frequency range.

For the specificity experiments, 62.5µg/mL of CRP or 40,0µg/mL plasminogen was then added to the PBS buffer, and allowed to react for one hour. After the reaction, the reaction wells were rinsed and refilled with pure (1× or 0.1×) PBS buffer.

For the sensitivity analysis, 12.5µg/mL, 1.25µg/mL or 0µg/mL of CRP in CRP buffer, was added to the PBS buffer. After the reaction, the reaction wells were rinsed and refilled with pure (1× or 0.1×) PBS buffer.

For the serum measurements, spiked and unspiked serum was added to pure serum to a final concentration of 62.5µg/mL of CRP. After the reaction, the reaction wells were rinsed and refilled with pure serum.

2.2.7 Heat-transfer resistance based method

In Chapter 4 and 5, the thermal denaturation of dsDNA fragments on NCD samples was evaluated by monitoring the change in R_{th} derived from the transition from dsDNA to ssDNA. During these measurements the dsDNA fragments on the NCD were denatured by increasing T1 from 35 °C to 85 °C with a heating rate of 1 °C/min. After cooling back down to 35 °C, a second heating run was performed to check if the dsDNA fragments were completely denatured during the first heating run. During these heating runs T1, T2 and P were recorded every second.

3

IMPEDIMETRIC MONITORING OF SNPs IN DNA

Partly based on:

Rapid Assessment of the Stability of DNA Duplexes by Impedimetric Real-time Monitoring of Chemically Induced Denaturation

B. van Grinsven, N. Vanden Bon, L. Grieten, M. Murib, S. D. Janssens, K. Haenen, E. Schneider, S. Ingebrandt, M. J. Schöning, V. Vermeeren, M. Ameloot, L. Michiels, R. Thoelen, W. De Ceuninck and P. Wagner

Lab Chip 2011; 11(9):1656 – 1663

Own contribution: Suggesting the development of a DNA-sensor for SNP-detection using chemical denaturation, suggesting the DNA sequences, suggesting the denaturation solution, biofunctionalization sensor electrodes, suggesting and performing the impedimetric and optical measurements, suggesting the reproducibility experiments, data processing using OriginLab, calculating theoretical melting temperatures, discussing the results and helping in writing and correcting the manuscript.

Abstract

In this chapter the electronic monitoring of DNA denaturation by NaOH using electrochemical impedance spectroscopy as a read-out technique in combination with fluorescence imaging as a reference technique is reported. The probe DNA, consisting of 36 nucleotides was covalently immobilized on nanocrystalline-diamond electrodes and hybridized with different types of 29 bases target DNA: a completely complementary sequence, two sequences containing a 1-base mismatch at different positions, and a completely random sequence. The mathematical separation of the impedimetric signal into the time constants for NaOH exposure and the intrinsic denaturation-time constants give clear evidence that the denaturation times reflect the intrinsic stability of the DNA duplexes. The measured intrinsic time constants correlated with calculated DNA-melting temperatures. The impedimetric method requires minimal instrumentation, is label-free and fast with a typical time scale of minutes and is highly reproducible. The sensor electrodes can be used repetitively. These elements suggest that the monitoring of chemically induced DNA denaturation is an interesting alternative to thermal denaturation to perform single nucleotide polymorphism analysis based on the difference in denaturation kinetics of complemenatary DNA duplexes and DNA duplexes containing a single mismatch.

3.1 Introduction

One of the central challenges in human genomics is the detection and identification of single nucleotide polymorphisms (SNPs). SNP detection can be performed by techniques that use information out of the hybridization of DNA strands, like microarray analysis. Microarrays are miniaturized assays with a parallelized read-out in combination with small sample volumes [Kwok, 2001; Ng et al., 2006]. Disadvantages are the long reaction times at the scale of at least 16 hours, the complete lack of dynamic information on the DNA binding kinetics, the need for fluorescent labeling of the target DNA, and the sophisticated optical read-out techniques. Also, microarrays are in principle limited to the detection of known mutations although there is recent progress to identify SNPs using a mathematical model that determines the thermodynamic aspects of the hybridization process between probe DNA and target DNA [Hooyberghs and Carlon, 2010].

Alternatively, mutation analysis can be performed using techniques that exploit the denaturation of double-stranded (ds) DNA rather than the hybridization process. The best known examples are real-time PCR with associated melting-curve analysis [Tindall et al., 2009] and denaturing gradient gel electrophoresis (DGGE) [Fodde et al., 1994; Lodewyckx et al., 2001]. Both techniques rely on the fact that DNA duplexes containing a SNP are less stable than complementary duplexes, resulting in lower denaturation temperatures. Nevertheless, both techniques require expensive instrumentation, real-time PCR requires the use of fluorescent labels and DGGE is not suitable for high-throughput analysis.

Due to the inherent complexity of microarrays and the established denaturation-based approaches, strong efforts are put into the development of label-free detection techniques based on electronic read-out principles. One of these electronic routes is the DNA switching method on Au electrodes proposed by Rant et al. [Rant et al., 2007]. This technique allows for real-time monitoring of hybridization and denaturation with the possibility to distinguish between complementary DNA duplexes and DNA duplexes containing mutations. Although the method requires no fluorescent labeling of the target DNA, labels are involved on the probe DNA. A switching effect is also the basis of the E-DNA

sensor [Rant et al., 2007], which employs an electrochemical redox reaction rather than fluorimetric detection and offers femtomolar detection limits. A method without any labeling and auxiliary chemistry is the solution-gate field-effect transistor (FET) device with the probe DNA directly immobilized on the gate oxide [Uslu et al., 2004; Sakata et al., 2005; Ingebrandt et al., 2007]. Real-time monitoring of hybridization is in principle possible and FETs can discriminate between complementary and mismatched DNA strands under ex situ conditions. The sensing effect of FETs is attributed to the intrinsic negative charge of ss- and ds-DNA fragments and to a redistribution of ionic charges at the proximity of the gate insulator during hybridization [Poghossian et al., 2005]. DNA-hybridization sensors based on impedance spectroscopy have been reported, this technique is especially versatile and can be employed not only for DNA hybridization, but also for protein detection and enzymatic reactions as shown in the review by Katz and Willner [Katz et al., 2003]. Moreover, impedimetric sensors are comparatively easy in fabrication since they are two-terminal devices without the need for specific semiconductor-doping profiles or advanced encapsulation techniques. Impedimatric DNA-sensors are established with screen-printed carbon electrodes [Davis et al., 2007], mixed self-assembled monolayers on Au electrodes using a redox system, conjugated polymers, GaN nanowires [Park et al., 2009]. In our prior impedimetric studies we reported a DNA-sensor based on nanocrystalline diamond electrodes [Vermeeren et al., 2007]. In this study was proven that this impedimetric biosensor is suitable for monitoring DNA hybridization and denaturation under relevant buffer solution- and temperature conditions.

Despite of all recent progress, the aforementioned electronic- or opto-electronic methods for DNA sensing have in common that they suffer from at least two or more of the following drawbacks: i) need for high-end instrumentation and incompatibility with upgrading towards high-throughput assays; ii) need for additional chemicals such as fluorescent dyes or redox mediators; iii) lack of sensor-regeneration capacity; iv) missing proof that the sensor response is intrinsic and unaffected by conductivity effects related to temperature or ionic composition of the buffer liquids; v) insufficient statistics to demonstrate the reproducibility; vi) lack of dynamic information on the kinetics of hybridization- or denaturation events.

In this work, we will address these challenges by combining synthetic diamond electrodes, with covalently immobilized probe DNA, with label-free, dynamic impedance read-out and a stringent control on temperature and medium composition using a miniaturized flow cell. Hereby, we will focus on the denaturation kinetics. One may expect a faster denaturation of DNA duplexes containing mismatches compared to complementary DNA duplexes, when they are exposed to a denaturation agent. Mutation-related denaturation times have indeed been recently reported by Özkumur et al., who employed label-free, optical interferometry on spotted microarrays, while the denaturation was induced by reducing the ionic strength of the buffer medium [Özkumur et al., 2010]. Besides of the intrinsic analogy with melting experiments, denaturation experiments offer the advantage to study duplex ensembles that are close to or at thermal equilibrium prior to the denaturation step. This starting condition is not necessarily fulfilled in the hybrization-based microarrays, where artefacts can occur due to metastable DNA-hybrid states formed between non-complementary DNA strands [Hooyberghs, Balesi et al., 2010].

3.2 Design of the sensor setup

To monitor DNA denaturation of different DNA sequences, a sensor setup is constructed as shown in Figure 3.1. This experimental setup consists of a homemade impedance spectroscopy unit as described in [van Grinsven et al., 2010] and a syringe system coupled to a Perspex flow cell with an inner volume of 110 µl. The NCD working electrode is sealed with an O-ring, resulting in an effective area of 28mm^2 exposed to the liquid. The counter electrode is a Au wire (diameter 500µm, oriented perpendicular to the flow direction) at a distance of 1.7mm from the surface of the working electrode. The working electrode is pressed with the Si backside on a copper lid, serving as back electrode and heat sink together. The impedance is measured by applying a fixed AC potential of 10mV. The response to this potential is an AC current. The complex impedance was measured for 31 frequencies, equidistant on a logarithmic scale, in a frequency range of 100Hz to 100kHz. The duration of one complete frequency sweep was 5.7 seconds. Miniaturized thermocouples are integrated in the copper lid and in the liquid. The cell is equipped with a quartz-glass bottom, enabling simultaneous fluorescence imaging with an inverted

confocal fluorescence microscope. The syringe system comprises two identical programmable syringe pumps (ProSense, model NE-500, The Netherlands) enabling flow rates of 0.73µl/hour to 1699mL/hour. One syringe serves for administering a 0.1M NaOH solution, the other delivers a 1× phosphate buffered saline (PBS) solution. Both are connected to a computer-controlled three-way valve.

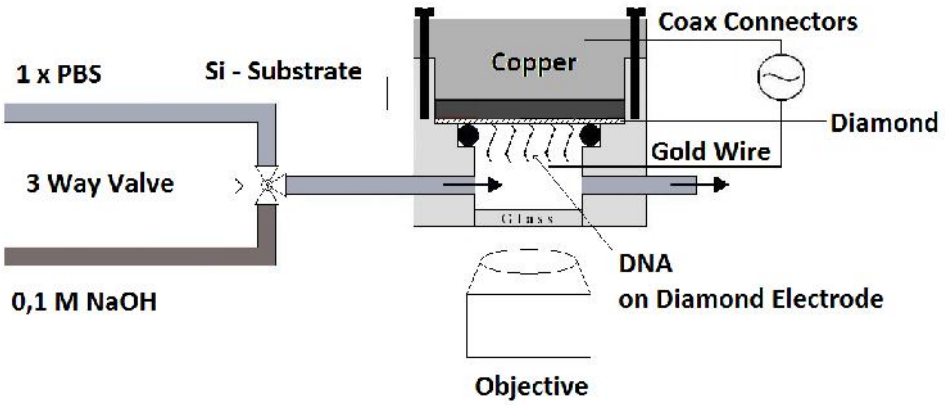

Figure 3.1: Schematic layout of the impedimetric flow cell.

3.3 Biofunctionalization of the sensor electrodes

Five NCD samples (#D1, #D2, #D3, #D4, #D5) were functionalized with the DNA sequences summarized in Table 3.1, using the procedure described in Section 2.2.2.

3.3.1 DNA sequences

The probe and target ssDNA molecules were purchased from Integrated DNA Technology (IDT, Leuven, Belgium) and the sequences are summarized in Table 3.1. The probe DNA sequence consists of 29 bases complementary to the target ssDNA and was modified at the 5' end with an NH_2-label and a spacer of 7 adenosine (A) bases that will remain single stranded. The first 7 adenosines at the 5' end of the probe DNA serve as a spacer to avoid border effects at the proximity of the electrode surface. The target DNA sequences, 29 bases, were

modified at the 5'-end with an Alexa Fluor® 488 label. The target DNA is either completely complementary to the probe DNA (FM), carries a 1-base mismatch to the probe DNA at bp 7 (MM7), carries a 1-base mismatch to the probe DNA at bp 20 (MM20) or is completely random and will not hybridize to the probe DNA (FMM). Note, that in both MM7 and MM20 sequences, a wildtype nucleotide G is substituted by a mismatch nucleotide C.

Table 3.1: Summary of the probe and the four target ssDNA sequences used in the hybridization and denaturation experiments.

Name	Size (b)	Sequence (5'-3')
Probe DNA[a]	36	CCCCTGCAGCCCATGTATACCCCCGAACC
FM[b]	29	GGTTCGGGGGTATACATGGGCTGCAGGGG
MM7[b,c]	29	GGTTCGGGGGTATACATGGGCTCCAGGGG
MM20[b,c]	29	GGTTCGGGGCTATACATGGGCTGCAGGGG
FMM[b]	29	TCAAATTGCCAGAACAACTACTGACTGAA

Notes:

[a] Probe sequence was modified at the 5'-end with an NH_2-label and a spacer of 7 A bases. The NH_2-label is conjugated to the 5'-end of the probe sequence with a C6 spacer arm.

[b] Target sequences were modified at the 5'-end with an Alexa Fluor® 488 label. This label is conjugated post-synthesis to the amino-modified target sequences as NHS ester.

[c] The position of the mismatched base, with respect to the probe DNA, is underlined

3.3.2 Functionalization with DNA

In a first step, NH_2-modified probe DNA-molecules are covalently linked on a NCD:COOH sample using carbodiimide coupling. The details of this procedure and the final washing steps to remove non-reacted probe DNA have been described in section 2.2.2. The concentration of the probe ssDNA used to functionalize 1 cm^2 of the NCD was 65,8µg/mL. This high concentration ensures a rapid functionalization.

In a second step the target DNA is hybridized to the probe DNA molecules attached to the NCD, by incubating the DNA-modified NCD samples for 2 hours at 30 °C with 263µg/mL of target DNA in 10× PCR buffer. Four different types of target DNA have been employed, respectively: FM, MM7, MM20 and

FMM, as described in Table 3.1. The hybridization conditions were determined in a previous study [Vermeeren et al., 2007].

After hybridization with the different types of target DNA, each of the NCD samples is studied by confocal microscopy to ensure the presence and homogeneous distribution of DNA. Details of confocal fluorescence microscopy are described in Section 2.2.3. In order to demonstrate that the fluorescence intensity originates from the Alexa Fluor® 488 dyes and not from the underlying diamond layer, bleaching experiments were performed. The hybridization with respectively FM, MM7 and MM20 target DNA was successfull and as expected, no FMM target DNA was hybridized (Figure 3.2).

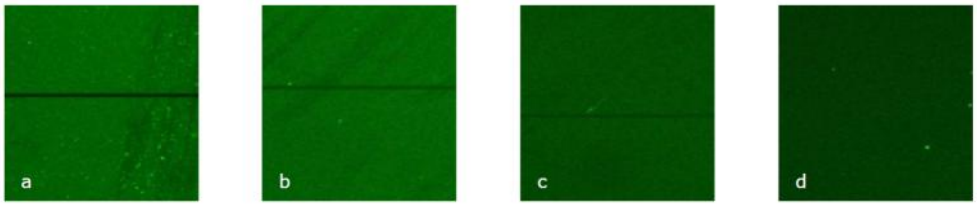

Figure 3.2: Confocal fluorescence images of a diamond electrode functionalized with different types of dsDNA. a. FM, b. MM7, c. MM20 and d. FMM DNA.

3.4 Comparison of impedimetric and optical denaturation monitoring

A real-time denaturation experiment on perfectly complementary dsDNA (probe + FM target DNA) on one diamond electrode is shown in Figure 3.3.

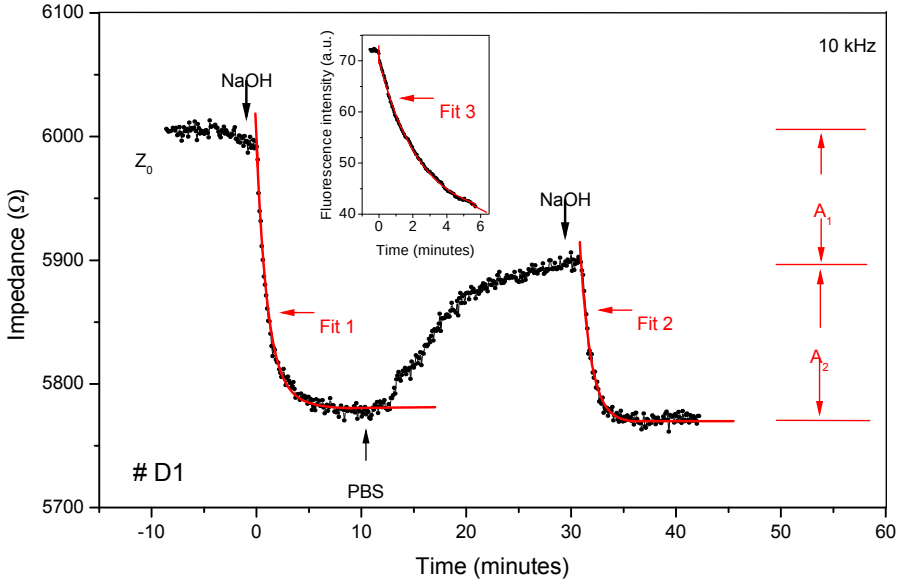

Figure 3.3: Impedance and fluorescence intensity profile during the denaturation of completely complementary dsDNA. Measured on #D1 and at frequency 10kHz. At t_0= 0min, 0.1M NaOH is pumped into the flowcell, replacing the 1×PBS buffer. The drop in fluorescence intensity (as shown in the insert) and in the impedance is described by respectively fit 3 and fit 1. At t_1= 12min, the cell was refilled with 1×PBS. At t_2= 30min, the cell is again flushed with 0.1M NaOH. The resulting decrease in impedance is described by fit 2. The amplitudes A_1 and A_2 indicate the individual influence of denaturation and medium exchange on the impedance.

After placing the functionalized electrode into the flowcell, the cell is filled with 1× PBS buffer and installed on the confocal fluorescence microscope. The cell is stabilized for 45min to guarantee that drift effects, due to temperature changes, are minimized and the noise level is below 0.5 %. The noise level in this measurement is related to the fact that the ambient temperature of about 25 °C could not be actively controlled. In all further measurements, not performed on the confocal microscope, the ambient temperature and temperature of all liquids were strictly stabilized to 19.3 °C, resulting in lower noise levels. At t_0 = 0min, 0.1M NaOH at a flow rate of 250µl/min enters the cell and replaces the 1x PBS buffer. This results in an impedance drop, which

consists of two separate contributions: i) the intrinsic effect of denaturation, which affects the electronic properties in the vicinity of the topmost diamond layer and ii) the medium exchange, because 0.1M NaOH has a higher conductivity than 1× PBS. To distinguish between both contributions quantitatively, the 0.1M NaOH was replaced by reintroducing 1× PBS at t_1 = 12min at a flow rate of 250µl/min The impedance increases and stabilizes at a plateau with a lower value as compared to the starting condition (Z_0). This demonstrates that the impedimetric properties of the electrode surface must have changed during denaturation because the ionic properties of the 1x PBS buffer are identical before and after the denaturation step. To analyze the effects solely due to the medium exchange from 1x PBS to 0.1M NaOH, at t_2 = 30min the 1× PBS was again replaced by 0.1M NaOH at a flow rate of 250µl/min This results in an impedance drop, reaching the same level as during the first NaOH phase. The superimposed processes of denaturation and medium exchange and the pure effect of medium exchange can mathematically be described as respectively fit 1 and fit 2.

Fit 1: $$Z(t) = Z(t=\infty) + A_1 \cdot \exp\left\{-\frac{t}{\tau_1}\right\} + A_2 \cdot \exp\left\{-\frac{t}{\tau_2}\right\} \quad (3.1)$$

Fit 2: $$Z(t) = Z(t=\infty) + A_2 \cdot \exp\left\{-\frac{t-t_2}{\tau_2}\right\} \quad (3.2)$$

The double-exponential equation 1 for superimposed, independent decay processes is known e.g. from the decomposition of biomass (tomato leaves) and the mass loss of tomato DNA as a function of time [Poté et al., 2005]. The parameter A_1 represents the denaturation-related decay amplitude and τ_1 the associated denaturation time constant; the amplitude A_2 refers to the impedance drop by the medium exchange and τ_2 is the corresponding medium exchange time constant. Equation 2 describes solely the influence of the medium exchange from 1× PBS to 0.1M NaOH after the denaturation has taken place and is therefore representative for the medium exchange as such. Note that there is no

intrinsic reason for the exponential time dependence related to the medium exchange, but the agreement with experimental data is excellent with a coefficient of determination (R^2) of 0.97 for Fit 2. The exponential time dependence of the splitting of DNA duplexes is naturally inherent to decay processes of non-interacting ensembles.

First, we applied equation 2 and extracted τ_2= 0.97±0.06min and A_2= 112±9Ω for the medium exchange effect. Inserting these values into equation 1 resulted in a denaturation-time constant τ_1= 2.24±0.14min and an amplitude A_1= 115±13Ω. The R^2 of Fit 1 is 0.94, giving support to the concept of superimposed decay processes. All fits are performed with Origin 7.1.

To crosscheck the electronically determined τ_1, time-lapse fluorescence imaging was performed during the denaturation step (time interval of 1.4 seconds between subsequent images) and the intensity I(t) was averaged over an area of 900 by 900µm^2. Selected images with intervals of 36 seconds, taken during the first 6 minutes of the dynamic imaging, are shown in Figure 3.4. There is remnant background intensity I_0, which is not vanishing even long after this period, and therefore attributed to the reflected laser light (data not shown).

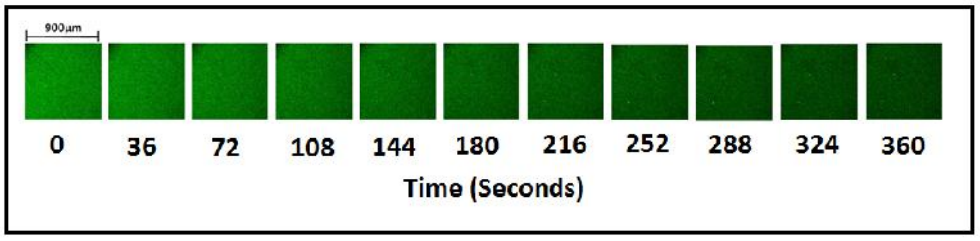

Figure 3.4: Confocal fluorescence images of the diamond electrode during the denaturation of perfectly complementary dsDNA at selected time points. The depicted area is 900x900µm; images are recorded with gain 1000.

The area-averaged intensity values are shown as an insert in Figure 3.3 and described with Fit 3.

Fit 3: $$I(t) = I_0 + I_{DNA} \cdot \exp\left\{-\frac{t}{\tau_3}\right\} \quad (3.3)$$

The fluorescence decay time constant τ_3= 2.41±0.05min is, within the error margins, perfectly comparable to the electronically determined τ_1. τ_3, as is τ_1, is insensitive to the medium composition and truly reflects the progressing denaturation at the diamond electrode surface. The Alexa Fluor® 488 labeled target DNA sequences are removed by NaOH exposure, and as such are responsible for the decaying fluorescence intensity, as they are transported away by the constant NaOH flow, while the confocal volume is restricted to a distance of less than 4.5µm from the surface of the NCD electrode. In conclusion, the electronically determined denaturation time constant τ_1 is a reliable measure for the duration of the chemically induced denaturation process.

Repeating the entire procedure on diamond sample #D1, re-hybridized with completely complementary target DNA, but measured in a temperature-stabilized environment of 19.3 °C and without laser illumination, gave τ_1 = 2.28±0.16min and τ_2 = 0.58±0.04min. The denaturation time constant is clearly consistent with the measurement at 25 °C although the time constant of the medium exchange τ_2 is faster, due to a slight modification to the flow system.

In a next step, the probe DNA was hybridized with target DNA containing a 1-base mismatch at base pair 7 (MM7). This resulted in a τ_1 =1.21±0.10min and τ_2= 0.48±0.02min. As expected, the time constant for the medium exchange τ_2 is very similar under identical environmental- and flow conditions, but the DNA duplexes containing a 1-base mismatch denature considerably faster than the completely complementary DNA duplexes. This strongly suggests that the monitoring of chemically induced denaturation can give an indication of the presence of SNPs.

3.5 Denaturation monitoring of SNPs in target DNA

In order to evaluate the reproducibility of the method and whether it allows to localize and identify 1-base mismatches, systematic studies on four additional diamond electrodes (#D2, #D3, #D4, and #D5) were performed. Each probe DNA-modified diamond electrode was consecutively hybridized with four different types of target DNA: FM, MM20, MM7 and FMM. Note that during the consecutive hybridizations with the different variants of target DNA, the same initial probe DNA layer was used to hybridize to, without any regeneration treatment to the level of COOH groups. The results obtained with electrode #D2 are shown in Figure 3.5. All measurements on each diamond sample were performed under temperature-stabilized conditions, which resulted in excellent R^2 values between 0.96 and 0.996 for Fit 1 and 2.

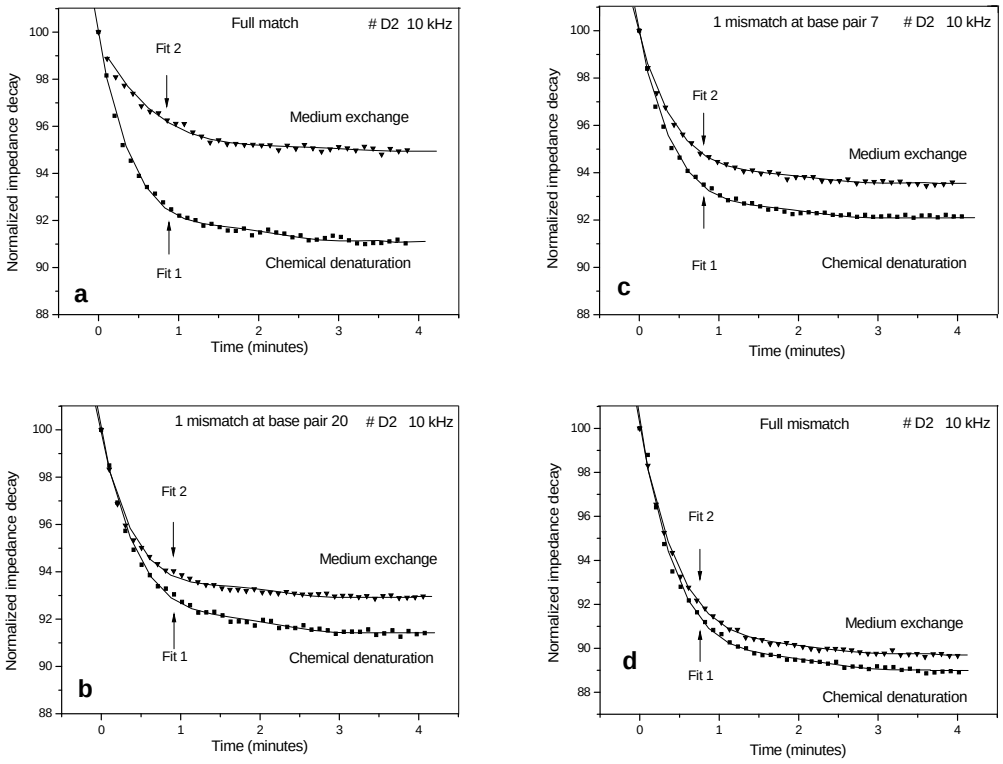

Figure 3.5: Impedance decrease during denaturation and medium exchange of FM (a), MM20 (b), MM7 (c), and FMM (d) target DNA. Measured on #D2 at frequency 10 kHz. The first and second impedance drop are described as chemical denaturation and medium exchange, respectively.

In Figure 3.5, the first impedance decay is normalized to the impedance value at t_0 and fitted with the equation for Fit 1; the second impedance decay is normalized to the equilibrium impedance value at the time t_2 and fitted with the equation for Fit 2.

The averaged time-constants for denaturation (τ_1) and medium exchange (τ_2) together with their respective standard deviations σ, obtained from the impedance measurements with all five different diamond electrodes are summarized in Figure 3.6.

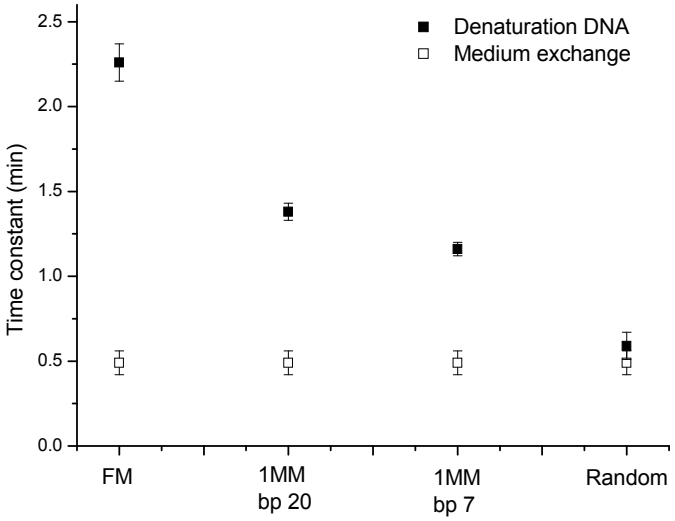

Figure 3.6: Compilation of the averaged denaturation and medium exchange time constants for the four different types of target DNA. The time constants for denaturation of DNA are indicated by closed symbols. The time constants for medium exchange are indicated by open symbols. All time constants are the average of 4 independent measurents on five different diamond electrodes, with corresponding standard deviations.

The averaged time-constants and the averaged normalized amplitudes are also summarized in Table 3.2. Concerning τ_1, we obtain 2.26±0.11min for completely complementary duplexes, 1.38±0.05min for the 1-base mismatch at

bp 20, 1.16±0.04min for the mismatch at bp 7, and finally 0.59 ± 0.08min for the completely random target sequence. The time constant for denaturation of the random sequence is the same within error margins, as to the averaged τ_2= 0.49±0.07min corresponding to the medium exchange.

To ensure that the marked difference in time constants is not emerging from an aging effect of the functional layer during consecutive denaturation processes, the order of hybridization and denaturation with the different types of target DNA was also considered. The samples #D2, #D3, and #D4 were first hybridized with FM, second with MM7, third with MM20 and finally with FMM. In case of sample #D5 the order was reversed, starting with the random sequence. As a result, all time constants determined with #D5 were found to be fully in line with the other electrodes.

Table 3.2: Comparison between theoretical melting temperatures and impedimetric denaturation time constants.

Target DNA	FM	MM20	MM7	FMM
T m(°C) (FractTM)	84	78	81	N/A
T m(°C) (HyTher)	79.5	75.0	76.7	N/A
$\langle\tau_1\rangle$(min)[a]	2.26±0.11	1.38±0.05	1.16±0.04	0.59±0.08
$\langle\tau_2\rangle$(min)[b]	0.49±0.07	0.49±0.07	0.49±0.07	0.49±0.07
$\langle A_1/Z(0)\rangle$(%)[a]	3.4±1.1	2.0±0.3	2.0±0.7	0.4±0.2
$\langle A_2/Z(t_2)\rangle$(%)[a]	4.9±1.3	6.9±0.5	5.6±1.2	9.8±1.1

[a] The parameters are the average of five independent measurements, with corresponding standard deviations.

[b] The parameter is the average of twinty independent measurements, with corresponding standard deviations.

Since the melting temperature T_m is the established measure for the stability of DNA duplexes and the key parameter for the localization and identification of SNPs, we employed two different algorithms to estimate T_m for the four different target-probe duplexes in our study. FractTM is available online [FractTM] and the underlying principles are described in [Leber et al., 2005]. HyTher™ is also available online and allows taking into account that the 5' end

of the probe DNA is tethered to a solid support. Both algorithms calculate T_m on the basis of the sequence of probe- and target DNA, nearest neighbor effects, the concentration of the probe DNA, and the Na^+ concentration of the surrounding electrolyte. The results of both algorithms are summarized in Table 3.2. In general, the predicted melting temperatures are in agreement with the obtained denaturation time constants: the complementary duplexes have the highest T_m and the longest denaturation time constant τ_1, the duplexes with the random sequence have the lowest T_m and shortest τ_1. The T_m of the duplexes containing a 1-base mismatch is reduced by 3 to 6 °C as compared to the completely complementary duplexes, while we observe a strongly decreased denaturation time τ_1. Interestingly, both algorithms predict a slightly higher stability for the duplex with the 1-base mismatch at bp 7 (FractTM: T_m = 81 °C, Hyther: T_m = 76.7 °C) compared to the 1-base mismatch at bp 20 (FractTM: T_m = 78 °C, HyTher: T_m = 75.0 °C). However our data reproducibly suggest that the duplexes with a 1-base mismatch at bp 7 denature slightly faster than those with a 1-base mismatch at bp 20. This may be explained by the fact that the impedimetric signal is influenced by changes of the ion distribution close to the electrode surface at the scale of the Debye length [Poghossian et al., 2005], being in the order of 1nm for 0.1M NaOH. Assuming that chemically induced denaturation starts preferentially at both ends of a DNA duplex and at the position of mismatches, a mismatch in the proximity to the electrode surface may indeed cause a faster response than a more distant defect.

Furthermore, we also studied the intra-sample reproducibility by hybridizing and denaturating electrode #D1 six times with the complementary target DNA sequence (FM) over a period of more than 4 months. The results are summarized in Table 3.3. The averaged value of the denaturation time constant τ_1 is 2.25±0.18min. This value is comparable to the averaged denaturation time constant obtained with the five different electrodes #D1 to #D5 as summarized in Table 3.2. The averaged values of this intra- versus inter-electrode comparison are practically identical. The slightly wider data scattering for the intra-electrode measurements can be attributed to the elongated time span in between these measurements with a possible influence on the biochemical reagents. The averaged time constant for the medium exchange τ_2 and the

corresponding standard deviation σ τ_2 in Table 3.3 is also comparable with the data in Table 3.2.

Finally, also the impedance amplitude A_1 gives information on the amount of bound target DNA. There is a systematic decrease of the normalized value A_1/Z_0, related to DNA denaturation, from 3.4 % for FM, to 2.0 % for MM20 or MM7 and finally to 0.3 % for FMM, which is close to a zero effect within the standard deviation. Keeping in mind that the hybridization was performed under standardized conditions, it is evident that defected sequences hybridize to a lesser extent than the complementary targets, the latter resulting in duplexes with the highest thermodynamic stability. Except for the random sequence, the normalized $A_2/Z(t_2)$, related to the medium exchange, is identical for all samples and sequences within the error margins.

Table 3.3: Time constants for denaturation (τ_1) and medium exchange (τ_2) for FM DNA over a period of 132 days. Measured on #D1.

# D1	τ_1 (min)	τ_2 (min)
Day 1	2.39 ± 0.08	0.49 ± 0.13
Day 44	2.21 ± 0.14	0.50 ± 0.07
Day 49	2.10 ± 0.16	0.55 ± 0.09
Day 50	2.02 ± 0.04	0.45 ± 0.08
Day 84	2.51 ± 0.02	0.46 ± 0.15
Day 132	2.28 ± 0.16	0.58 ± 0.04
‹τ›	2.25±0.18	0.50±0.05

3.6 Conclusion

In summary, impedance spectroscopy was used to monitor the real-time kinetics of chemically induced denaturation of four different types of DNA duplexes on diamond electrodes. By using this technique, denaturation time constants for all the used DNA duplexes are reproducibly identified. All time constants are at the scale of minutes while the denaturation takes the longest for complementary DNA duplexes. Moreover, the time constants correlate well with calculated melting temperatures. This suggests that the novel approach may possibly allow

for a fast localization and identification of 1-base mismatches similar to the established, but cumbersome, DNA melting techniques. In addition, the novel method is intrinsically label-free (note that labels were only used to allow for fluorescence imaging as a reference technique) and as-prepared electrodes can be used repetitively thanks to the strong covalent link between probe DNA and the diamond platform, and to the chemical inertness of diamond as such. The required instrumentation is minimal, consisting of an impedance analyzer, which can operate at a fixed frequency, and a system to administer NaOH with defined temperature and flow rate. Finally, the proposed method has the potential to be downsized and parallelized towards a microarray-like format as illustrated by the diamond-based microelectrode arrays with spot sizes of 50µm [Bonnauron et al., 2008]. Given the fact that the real-time denaturation method provides dynamic information, it can reduce the number of required spots considerably as compared to the end-point character of classical microarrays with fluorimetric readout.

4

DETECTION OF SNPs BY HEAT-TRANSFER RESISTANCE

Partly based on:

Heat-Transfer Resistance at Solid-Liquid Interfaces: A Tool for the Detection of Single-Nucleotide Polymorphisms in DNA

B. van Grinsven, N. Vanden Bon, H. Strauven, L. Grieten, M. Murib, K. L. Jiménez Monroy, S. D. Janssens, K. Haenen, M. J. Schöning, V. Vermeeren, M. Ameloot, L. Michiels, R. Thoelen, W. De Ceuninck and P. Wagner

ACS Nano. 2012; 6(3): 2712 – 2721

Own contribution: Suggesting the development of a DNA-sensor for SNP-detection using thermal denaturation, suggesting the DNA sequences, biofunctionalization sensor electrodes, optical measurements, co-editing the manuscript.

Abstract

In this chapter, a novel method to detect single-nucleotide polymorphisms in DNA based on the heat-transfer resistance change during DNA denaturation is reported. The heat-transfer resistance of a DNA-functionalized diamond surface increased during DNA denaturation, therefore the resulting ssDNA molecules onto the diamond electrode behave like a thermally insulating layer. This effect can be utilized to identify DNA melting temperatures via the switching from a low to a higher heat-transfer resistance. The melting temperatures of different types of 29 base pairs DNA duplexes (completely complementary or containing 1-base mismatch) identified with this method correlate well with data calculated by modelling. The method is fast, label-free, allows for repetitive measurements, and can also be extended towards array formats. Reference measurements by confocal fluorescence microscopy and impedance spectroscopy confirm that the switching of heat-transfer resistance upon denaturation is, indeed, related to the thermal on-chip denaturation of DNA.

4.1 Introduction

The detection and identification of single-nucleotide polymorphisms (SNPs) in DNA is of central importance in genomic research for several reasons. First, SNPs are involved in hundreds of genetic disorders such as Alzheimer, mucoviscidosis, phenylketonuria, and several types of breast- and colon cancer [Schon et al., 1997; Dunning et al., 1999]. Second, SNPs in the so-called ADME (absorption, distribution, metabolism, excretion) genes significantly influence the effectiveness of treatment and this is a major topic in the field of theranostics [Hooper, 2006]. SNPs can be characterized by hybridization-based assays such as microarrays: the massive parallelized readout is an advantage, but the method requires fluorescent labeling, optical readout, and long hybridization times of ~ 16 hours at elevated temperatures. Furthermore, the method has an 'end-point' character without providing dynamic information on molecular recognition between probe- and target fragments. Finally, it is hard to unravel unknown mutations by microarrays although there is recent progress based on refined statistical analysis allowing detecting unknown mutations [Hooybergs and Carlon, 2010]. Due to these drawbacks, unknown mutations are frequently identified by denaturation-based approaches. Widespread methods are real-time PCR with associated melting-curve analysis [Tindall et al., 2009] and DGGE or temperature-gradient gel electrophoresis (TGGE) [Fodde et al., 1994; Muyzer et al., 1998]. However, real-time PCR requires fluorescent labeling and expensive instrumentation while DGGE is time- consuming, less suitable for parallelized analyses, and lacking information on denaturation kinetics.

To overcome these limitations, several label-free electronic and opto-electronic DNA-sensor concepts have been proposed in recent literature. All of them have in common that they can operate in principle under hybridization- and under denaturation conditions, while they can also be miniaturized and integrated in sensor arrays with a parallelized readout. Without being exhaustive, we mention electrostatic switching effects and associated fluorescence monitoring [Rant et al., 2007], impedance spectroscopy [Katz et al., 2003; Vermeeren et al., 2007; Park et al., 2009; van Grinsven et al., 2011], electric field-effect based devices [Poghossian et al., 2005; Ingebrandt et al., 2007; Kawarada et al., 2011], surface plasmon resonance [Kick et al., 2010], and

linear (electric) conductivity measurements through single DNA duplexes [Guo et al., 2008]. The underlying principles of these sensing effects are not yet clarified in all details, but they are presumably associated with one or several of the following phenomena, which occur upon hybridization or denaturation: change in mechanical rigidity of DNA, changes in the total charge of DNA, redistribution of counter ions, and changes of the dielectric properties near the surface onto which the probe DNA is attached. Most straightforward, but especially hard to implement in a low-cost diagnostic instrument, are the conductivity measurements through single DNA molecules, which have been subject to extensive theoretical and experimental studies, see e.g. [Guo et al., 2008; Dekker et al., 2001; Cuniberti et al., 2002; Cohen et al., 2005]. Very recently, Velizhanin et al. proposed in a theoretical study on nanoscale heat transport through individual DNA molecules that the thermal current should significantly increase upon denaturation [Velizhanin et al., 2011]. This would offer, besides of the aforementioned (opto-) electronic approaches, an alternative access towards the detection of denaturation events and contribute to the understanding of the underlying vibrational dynamics.

In the present work, the temperature-dependent heat-transfer properties of DNA-functionalized, temperature controlled diamond electrodes was studied. Although this approach does not work at the single-molecule level it offers distinct advantages: the DNA fragments are in contact with buffer medium at any time, the fragments are free to undergo conformational fluctuations, and the sensor device as such can be implemented with reasonable technological efforts. The methodology allows identifying melting temperatures by using only an adjustable heat source in combination with two temperature sensors. The sequence chosen in this work is an exon-9 fragment of the phenylalanine hydroxylase (PAH) gene, mutations in this gene lead to the metabolic disorder phenylketonuria [Guldberg et al., 1998].

4.2 Design of the sensor setup

The sensor setup used for thermal monitoring is shown in Figure 2.2 and was described earlier in paragraph 3.2 in the context of chemical DNA denaturation studies. This device allows simultaneous thermal, optical and impedance

monitoring. All measurements described in this chapter were performed under static conditions. For heat-transfer measurements, the device was now equipped with two miniaturized thermocouples (type K, diameter 500µm, TC Direct, The Netherlands) monitoring the temperature T_1 of the copper backside contact and the liquid temperature T_2 at a position in the center of the flow cell at 1.7mm above the chip surface. The heat flow was generated with a power resistor (22Ω, MPH 20, Farnell, Belgium) glued onto the copper block with heat-conductive paste and tightly fixed with a screw. To regulate T_1, the thermocouple signal was led to a data acquisition unit (Picolog TC08, Picotech, United Kingdom) and from there processed into a PID controller (parameters: P = 10, D = 5, I = 0.1). The calculated output voltage was sent via a second controller (NI USB 9263, National Instruments, USA) to a power operational amplifier (LM675, Farnell, Belgium) and fed into the power resistor. Sampling of the T_1 and T_2 values was done at a rate of one measurement per second.

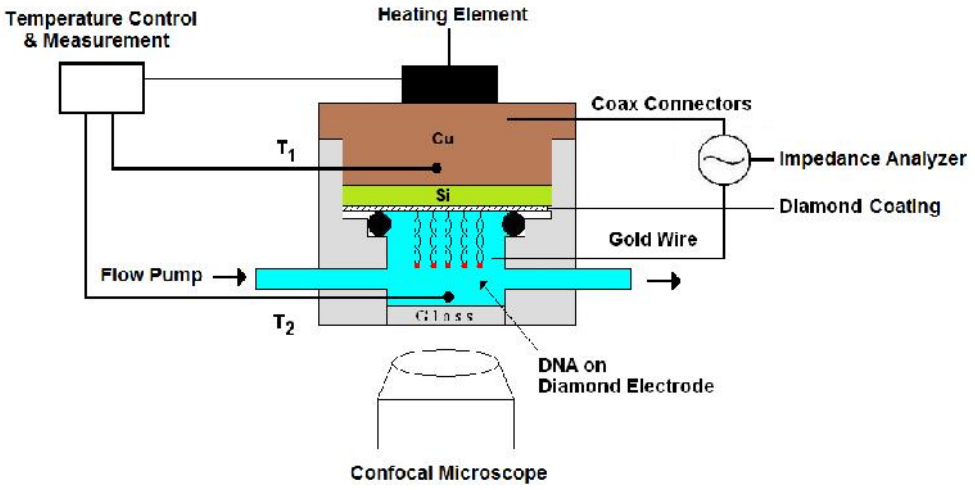

Figure 4.1: Schematic layout of the temperature controlled flow cell.

4.3 Biofunctionalization of the sensor electrodes

The central element through which the thermal current will pass is a Si chip (~ 10 by 10mm^2) covered with a thin layer of boron-doped, nanocrystalline

diamond [Janssens et al., 2011], see Section 2.2.1 for a detailed description of the fabrication of the used diamond electrodes. This diamond layer serves as an immobilization platform onto which DNA molecules are covalently bound via the photochemical 'fatty acid & EDC' coupling.

4.3.1 DNA sequences

The probe and target ssDNA molecules used in this study are similar to the sequences used in the impedimetric monitoring of chemical DNA denaturation, described in Table 3.1.

4.3.2 Functionalization with DNA

In a first step, NH_2-modified probe DNA was covalently linked on a NCD:COOH sample using carbodiimide coupling, forming a stable amide bond between the DNA probe and the NCD electrode. The details of this procedure and the final washing steps to remove non-reacted probe DNA have been described in Section 2.2.2.

In a second step the target DNA was hybridized to the probe DNA molecules attached to the NCD. Three different types of target DNA have been employed: FM, MM7 and MM20. See Section 3.3.2 for a full description of the hybridization procedure.

After hybridization with the different types of labeled target DNA, the fluorescence of each NCD sample was studied by confocal microscopy to ensure the presence and homogeneous distribution of DNA. Bleaching experiments confirmed that the fluorescence intensity originated from the Alexa Fluor® 488 dyes and not from the underlying diamond layer. All intensities measured after denaturation were in full agreement with the remnant intensities found before on bleached regions, meaning that the data are not affected by laser-intensity fluctuations.

4.4 Comparative optical, impedimetric and heat-transfer measurement

The first series of measurements, described in this section, refer to the denaturation of FM dsDNA molecules on a diamond-coated Si electrode denoted

as #D1. During this measurement, T_1 was increased with a heating rate of 1 °C/min from 35 °C to 90 °C and cooled back to 35 °C at the same rate by reducing the heating power. This was performed for three consecutive heating/cooling runs and the time dependence of T_1 and T_2 is shown in Figure 4.2. Note that during the first heating, an anomalous behaviour of T_2 occurs, highlighted with a circle, which was absent during the second and the third run. This first-run temperature anomaly was also found with three other diamond electrodes (#D2, #D3, and #D4), meaning that the effect appears to be intrinsic and most probably related to thermally induced DNA denaturation.

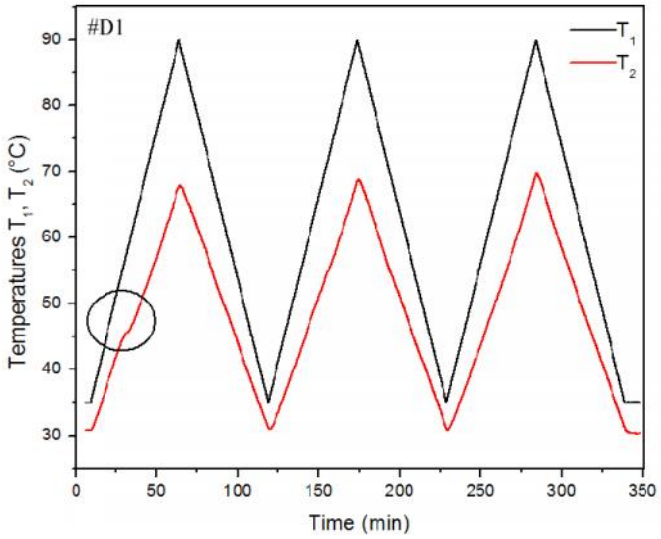

Figure 4.2: Temperature profile of the denaturation of FM DNA. The black line is the temperature T_1 of the Cu backside contact, the liquid temperature T_2 is shown as a red line.

In order to prove this assumption, the first and second heating/cooling runs were repeated with simultaneously measuring the impedance of the sensor cell and monitoring the fluorescence intensity on the electrode surface. These measurements were performed at non-regulated room temperature (about 22 °C) and we verified that there was no measurable heat input by the laser beam into the system. Figure 4.3 summarizes the data obtained with the three

independent methods, confirming the assumption that DNA denaturation has indeed an impact on the heat-transfer properties of the device.

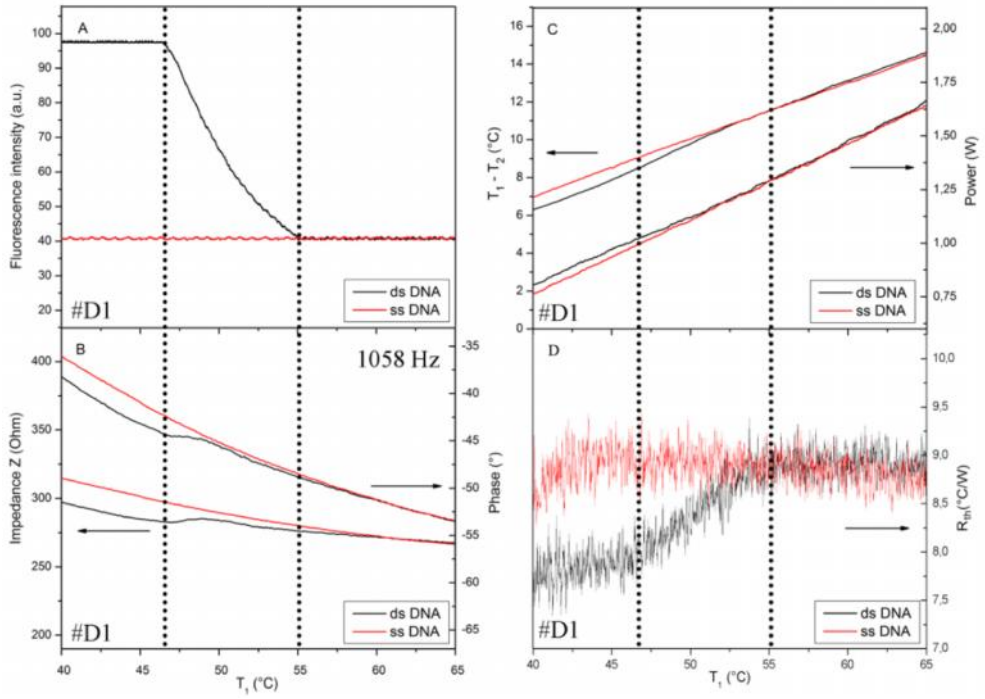

Figure 4.3: Compilation of simultaneously measured fluorescence-intensity data (panel A), impedance data (panel B) and heat-transfer related data (panel C and D). The black line is the FM dsDNA during first heating run, the second heating run is shown as a red line.

The temperature (T_1) dependence of the fluorescence-intensity signal from the electrode surface is shown in panel A from Figure 4.3. This fluorescence intensity curve is derived from confocal fluorescence images with time intervals of 1.4 seconds. This curve shows that the denaturation sets in at 47 °C and terminates at 55 °C, where the fluorescence intensity drops to its background value, which originates from strayed laser light. The denatured sample shows this background intensity at all temperatures below denaturation temperature. The midpoint temperature of the fluorescence-intensity decay is found at 49.7 °C. Labeled target DNA, removed from the immobilized probe DNA during denaturation, cannot contribute to the fluorescence signal anymore

because the confocal volume is limited to a maximum of 5µm above the chip surface, which is negligible as compared to the total cell volume. This fluorescence measurement is a stringent and independent control because it is electronically and physically decoupled from the rest of the setup, which is steering and monitoring T_1 and T_2 and measuring the impedance values. Therefore, the fluorescence data are definitely free of any hypothetical cross-talk effects. Confocal images during the denaturation of full-match dsDNA at selected temperatures are shown in Figure 4.4.

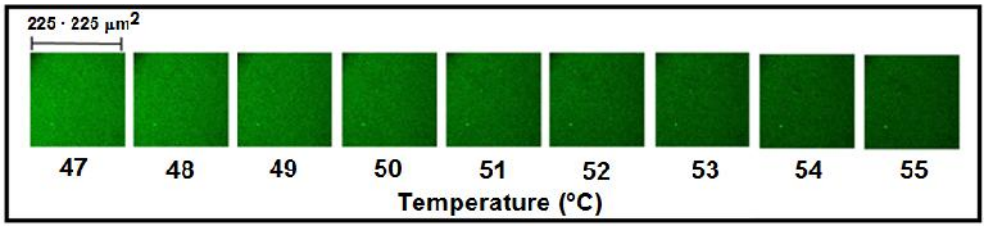

Figure 4.4: Confocal fluorescence images of the diamond electrode during the denaturation of FM dsDNA at selected temperatures. The depicted area is 225 by 225µm².

Panel B in Figure 4.3 shows the T_1 dependence of the amplitude and the phase angle of the impedance signal at a frequency of 1058Hz. Below 47 °C, the diamond electrode functionalized with dsDNA or ssDNA behave differently in impedance amplitude and in phase angle while they overlap for temperatures above 57 °C. The impedance amplitude of the first heating run clearly shows a local maximum at 49.5 °C, which corresponds with the midpoint temperature of the fluorescence-decay curve. We mention that the impedance results are a superposition of two effects: the surface impedance of electrodes with dsDNA versus ssDNA are different as reported in chapter 3, but also the impedance of the buffer solution depends sensitively on temperature.

Panel C in Figure 4.3 shows the temperature difference $\Delta T = T_1 - T_2$ as a function of T_1, with the black curve corresponding again to the first heating run while the red curve presents the second heating run. Both curves overlap at temperatures above 55 °C, where the melting transition is completed. Panel C also includes the temperature dependence of the electrical heating power P,

which was required to achieve the linear raise of T_1 according to the heating rate of 1 °C/min Also here is a difference between the diamond electrode functionalized with dsDNA or ssDNA, which disappears above 55 °C.

To extract the heat-transfer resistance (R_{th}) quantitatively, for all temperatures the ratio of the temperature difference $\Delta T = T_1 - T_2$ was analyzed and the input power P according to $R_{th} = \Delta T/P$. The resulting data are summarized in panel D of Figure 4.3. The somewhat noisy appearance is related to the fact that we show non-filtered, raw data obtained in an environment without active temperature control: while the temperature T_1 is strictly linear and smooth in time, the required heating power shows small fluctuations within short time periods. In the beginning of the measurement a low-temperature value of R_{th} = 7.7 °C/W was found, which starts to increase around 46°C and reaches a new equilibrium value of 8.9 °C/W at and above 55 °C (black curve). The midpoint of the transition is found at $T_{midpoint}$ = 49.2 °C, this is again close to the midpoint temperature of the fluorescence-decay curve. During the second heating run an almost temperature independent R_{th} of 8.9 °C/W (red curve) was observed. This increase of the absolute R_{th} value by ~ 1.2 °C/W (16 % increase) due to DNA denaturation is a substantial effect, keeping in mind that the layer of DNA molecules on the diamond electrodes is only a miniscule component (the fragment length corresponds to 10nm) as compared to the total heat-transfer path with a distance of almost 3mm between the two thermocouples. The effect size is more than twice as strong as the denaturation-induced change of the impedance amplitude with an increase around 7 %. Based on all these observations, the temperature abnormality during the first heating run documented in Figure 4.2 is one-to-one related to the thermally induced denaturation of dsDNA, which changes the R_{th} properties on DNA functionalized diamond electrode surfaces.

4.5 Denaturation monitoring of SNPs in target DNA

The R_{th} measurements described in this section were all performed with the diamond electrode #D2 in a temperature-stabilized environment. All measurements are summarized in Figure 4.5.

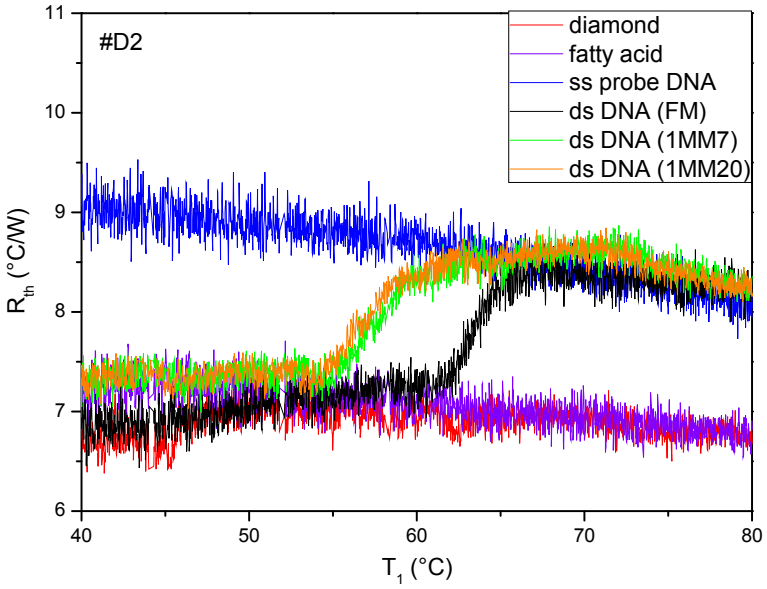

Figure 4.5: R_{th} of different target sequences in function of temperature (T_1).

First the R_{th} change of an oxidized B-NCD electrode (NCD:O) was measured in function of the temperature of the cupper lid (T_1). During measurement T_1 was increased from 35 °C to 85 °C. The R_{th} value of the NCD:O, shown as a red line in Figure 4.5 is around 6.7 °C/W – 7.0 °C/W and widely temperature-independent. Carboxylation of the B-NCD electrode (NCD:COOH) also resulted in a temperature-independent R_{th} (purple line in Figure 4.5), which can, within the experimental resolution, not be distinguished from the R_{th} of the NCD:O electrode. The R_{th} of NCD:O and NCD:COOH electrodes are comparable, because the length of the dense layer of 10-

undecenoic fatty acid molecules on the carboxylated B-NCD surface does not exceed 1nm.

Next the NCD:COOH electrode was functionalized with single-stranded probe DNA molecules, this causes an increase of the R_{th}-value to 9.0 °C/W at 40 °C and to 8.4 °C/W at 80 °C (blue line in Figure 4.5).

This sample was subsequently hybridized with the FM, MM7 and MM20 target DNA sequences, the R_{th} changes according to a temperature increase are respectively shown in Figure 4.5 as a black, a green and an orange line. Note that the three hybridizations were performed with the original probe DNA on the sensor chip without any kind of surface regeneration. All curves display a stepwise increase of R_{th} with midpoint temperatures of 63.0 °C, 57.6 °C and 56.8 °C for respectively the denaturation of FM, MM7 and MM20 dsDNA molecules. The relative order of stability agrees well with calculated melting temperatures summarized within Table 3.2 in Chapter 3. We point out that our denaturation temperatures are lower than the predicted values; however, the fluorescence control renders the experimental data unquestionable.

Finally the R_{th} changes during the thermal denaturation of FM target DNA were monitored on 4 different diamond electrodes (#D1, #D2, # D3 and #D4), all $T_{midpoint}$ and R_{th} data are summarized in Table 4.1. All data were obtained from measurements in the temperature-stabilized environment of 19.3 °C. In case of #D3, the R_{th} change is measured in threefold (a, b, and c) with a complete regeneration of the sensor surface before the third measurement.

Table 4.1: Compilation of the $T_{midpoint}$ and R_{th} data of thermally induced denaturation of FM dsDNA molecules obtained on 4 different diamond electrodes. The R_{th} values of the ss-state were measured at 10 °C above $T_{midpoint}$ while the corresponding Rth values in the ds-state were calculated at 10 °C below $T_{midpoint}$.

Diamond electrode	#D1	#D2	#D3 (a)	#D3 (b)	#D3 (c)	# D4	Average (N=6)	±
T midpoint (°C)	52.5	63.0	53.5	53.5	56.5	52.0	55.2	4.1
R_{th} (°C/W) (ss-state)	8.9	8.6	8.6	8.7	8.7	8.7	8.7	0.1
R_{th} (°C/W) (ds-state)	7.6	7.1	7.3	7.3	7.4	7.2	7.3	0.2
ΔR_{th} (°C/W)	1.3	1.5	1.3	1.4	1.3	1.5	1.4	0.1

There is a certain sample-to-sample variation of the midpoint temperatures and we attribute this to the manual mounting of the DNA functionalized diamond electrode in the sensor device, possibly in combination with minor fluctuations in the precise size of the electrodes and the thickness- and grain-size of their diamond coatings. When looking at the intra-sample variability, it can be seen that the subsequent measurements a and b performed with sample #D3 deliver practically identical results and only after the complete surface regeneration a certain shift of $T_{midpoint}$ occurs. Despite of this, the absolute change of R_{th} upon denaturation is remarkably constant and has for all DNA functionalized diamond electrodes a value of 1.4±0.1 °C/W. To determine ΔR_{th}, the difference between R_{th} measured at 10 °C above $T_{midpoint}$ and the corresponding value 10 °C below $T_{midpoint}$ is calculated. In both cases this temperature is clearly situated outside the range of the melting transition state. The universal amplitude of ΔR_{th} strongly supports the idea of a universal feature, which is independent of the employed sensor electrodes.

4.6 Discussion

The increase of R_{th} upon denaturation has to our knowledge not been reported in prior literature and there is also no explanation yet based on first-principles calculations. The theoretical work of Velizhanin et al. predicts actually an enhanced heat-transfer by ssDNA, but the boundary conditions are different (DNA molecule under dry conditions, clamped between two heat reservoirs with a fixed temperature difference) and modeling parameters come into play [Velizhanin et al., 2011]. The experimental thermal and electronic conductivity studies by Kodama et al. on individual dsDNA fragments combined with Au nanoparticles is also not comparable to our approach: These measurements under vacuum conditions (temperature regime 100 K – 300 K) did not cross the melting transition and both fragment ends were tethered to Au contacts, limiting the mechanical freedom of the molecules [Kodama et al., 2009].

However, we can clearly state that the observed impact of denaturation on the heat-transfer resistance cannot be explained by a calorimetric effect. Calorimeters measure interaction energies during a molecular recognition or unbinding process and have been employed in classical DNA studies [Privalov et al., 1969; Gruenwendel et al., 1974] and more recently in the context of

synthetic receptors [Smirnov et al., 2002; Lettau et al., 2006]. Here, we find a persistent change of R_{th} from low values at all temperatures below the melting transition to higher values at all temperatures above this transition, an effect, which is not restricted to the melting transition itself. The fact that dsDNA does not measurably increase the heat-transfer resistance can be understood on the following grounds: the dsDNA sequences of 29 base pairs have a length of 10 nm, which is far below the estimated persistence length of 50 nm [Ambia-Garrido et al., 2010; Wenmackers et al., 2006]. Therefore, these dsDNA sequences can be considered as rigid, upright helices on the electrode surface with a tilt angle in the range of 31° - 52° [Rezek et al., 2007, Wenmackers et al., 2008]. The areal density of dsDNA molecules is, irrespective of the immobilization method, in the range from 10^{12} to 10^{13} duplexes per cm^2, as described in [Vermeeren et al., 2008]. The most probable areal density in our case, as determined by x-ray photoemission spectroscopy, is $8 \cdot 10^{12}/cm^2$ [H. Yin and H.-G. Boyen, manuscript under preparation]. With a diameter of 2.37 nm for one dsDNA molecule, we conclude that about 35 % of the electrode surface is covered with dsDNA molecules while the remaining surface fraction of 65 % still represents the unaltered solid-liquid interface, this principle is illustrated in Figure 4.6.

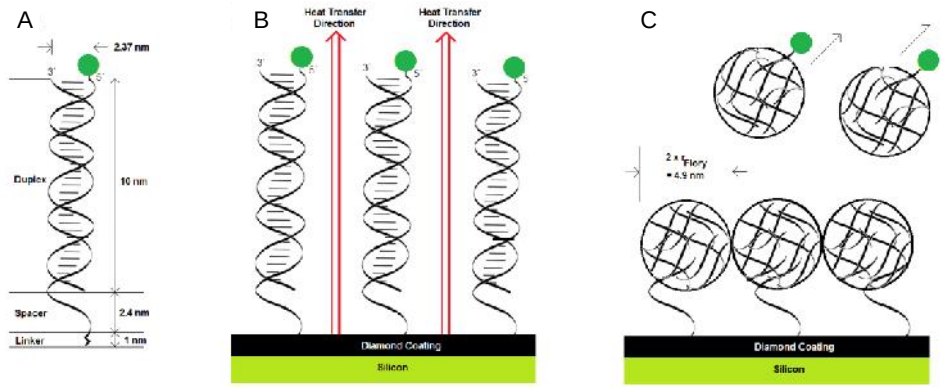

Figure 4.6: The heat-transfer principle illustrated on a DNA functionalized diamond electrode. Panel A sketches a labeled FM dsDNA molecule and panel B illustrates the heat-transfer path through a molecular dsDNA layer on a diamond electrode. The configuration of the DNA molecules after denaturation is shown in panel C.

A diamond electrode functionalized with dsDNA molecules transfers thermal energy from the phonons in the diamond lattice to the water molecules in the buffer solution above the diamond surface, while there is also recent evidence that the heat-transfer along dsDNA is based on molecular vibrations [Kodama et al., 2009]. After denaturation, we are dealing with fragments with a total length of 36 nucleotides (L=12.24 nm) while the persistence length drops to l_p = 1.48 nm [Ambia-Garrido et al., 2010]. Therefore, the ssDNA molecules curl up in irregular shapes and the typical Flory radius can be approximated according to $r_{Flory} = (l_p \cdot L/3)^{1/2}$ [Wenmackers et al., 2006]. This results in r_{Flory} = 2.46 nm. Based on the presence of $8 \cdot 10^{12}$ ss-DNA fragments per cm^2, the surface coverage increases to nominally 150 %, corresponding to a densely covered surface. Therefore, we suppose that after denaturation the major parts of the diamond surface are covered with random coils of ssDNA, which interrupts the heat-transfer from the diamond surface to the buffer. A visualization of the situation after denaturation is given in panel C of Figure 4.6.

Besides the considerations on the underlying principle of the heat-transfer effect, the method should be translated into an applicable approach in clinical genetic research. Therefore this concept has to be extended to high-throughput, parallellized mutation detection and identification in exon-size DNA-fragments of PKU patients. Also the detection of heterozygous mutations by using the heat-transfer resistance principle should be investigated to detect PKU carriers. Finally a miniaturized, array type detection system will be fabricated that allows simultaneous detection of point mutations in all PAH exons. The first step towards an array format would be the miniaturization of the sensing electrodes, diamond-based electrodes on glass substrates with a diameter below 100 µm have been documented in literature [Bonnauron et al., 2008]. Also, diamond nanowires with a thickness even below 10 nm have been fabricated by reactive ion etching [Yang et al., 2008]. The functionalization of these micro- and nanostructures with selected probe- and target DNA can e.g., be achieved by dip-pen nanolithography [Demers et al., 2002]. A bigger challenge would be the development of an array-type detection system, more specifically an array of planar thermocouples with a contact area comparable to the size of the sensor spots. Here, the present state-of-the-art are thermocouple arrays with an area of a few μm^2 of each junction [Liu et al., 2011], which looks most feasible to detect

the heat flow through the individual sensor spots with sufficient spatial resolution to minimize crosstalk between neighboring spots.

4.7 Conclusion

In conclusion, the heat-transfer based detection method presented here, could be considered as a label-free and real-time alternative to the currently available denaturation-based techniques for the detection of DNA point mutations. However, to be applicable in routine genetic analysis, detection of SNPs in patient-derived DNA samples is necessary, as is discussed in Chapter 5. Nevertheless, heat-transfer based biosensing is an inexpensive detection method, because it requires a minimum of instrumentation (two thermocouples, a PID controller and an adjustable heat source). Moreover, the heat-transfer based detection method can be expanded to monitor other types of biomolecular interactions and eventually the diamond surface used in this setup can be replaced by other sensor surface materials showing good heat conductivity. This has already been demonstrated by Eersels et al. (2013). They combined the heat-transfer based method with aluminium electrodes coated with surface imprinted polymer layers (SIPs), that specifically bind to human cancer cells. The detection of the different types of cells is based on their binding to the imprinted cavities, covering the aluminium electrode and thereby causing an increase in R_{th}. The observed detection limit in PBS buffer is 3×10^4 cells/mL, although optimization is required to reach 1 cell/mL detection limits for medical relevant analysis. Also small molecules can be detected using molecularly mprinted polymer (MIP)-type receptors. MIPs can be used for the heat-transfer based detection of L-nicotine, histamine or serotonine, as described in Peeters et al. (2013). The detection of these small molecules is based on the binding of the target molecules to the MIP nanocavities, blocking the heat-transfer through one cavity, resulting in an increase in the total R_{th}. This effect is concentration dependent, the more small molecules that are bound, the more cavities will be occupied and subsequently a gradually increase in R_{th} is observed. In buffer solutions, a detection limit in a nanomolar range was reached. Furthermore, L-nicotine could be detected in spiked saliva samples. In theory, the heat-transfer based detection principle can be extended for the detection of protein biomarkers using either antibodies or aptamers as receptor molecules.

5

HEAT-TRANSFER-BASED DETECTION OF SNPs IN THE PAH GENE OF PKU PATIENTS

Based on:
Heat-transfer-based detection of SNPs in the PAH gene of PKU patients
N. Vanden Bon, B. van Grinsven, M. S. Murib, W. S. Yeap, K. Haenen, W. De Ceuninck, P. Wagner, M. Ameloot, V. Vermeeren, and L. Michiels
Int J Nanomedicine 2014, 9: 1629-1640

Abstract

Conventional neonatal diagnosis of phenylketonuria (PKU) is based on the presence of abnormal levels of phenylalanine in the blood. However for carrier detection and prenatal diagnosis, direct detection of disease-correlated mutations is needed. To speed up and simplify mutation screening in genes, new technologies are developed. In this study, a heat-transfer method (HTM) is evaluated as a mutation detection technology in entire exons of the phenylalanine hydroxylase gene (PAH). This method is based on the change in heat-transfer resistance (R_{th}) upon thermal denaturation of dsDNA on nanocrystalline diamond (NCD). First, ssDNA fragments that span the size range of the PAH exons were successfully immobilized on NCD. Next, it was studied whether an R_{th} change could be observed during the thermal denaturation of these DNA fragments after hybridization to their complementary counterpart. A clear R_{th} shift during the denaturation of exon 5, exon 9, and exon 12 dsDNA was observed, corresponding to lengths up to 123 bp. Finally, R_{th} was shown to detect prevalent single-nucleotide polymorphisms (SNPs), c.473G>A (R158Q), c.932T>C (p.L311P) and c.1222C>T (R408W), correlated with PKU, displaying an effect related to the different melting temperatures of homoduplexes and heteroduplexes.

5.1 Introduction

Phenylketonuria (PKU; MIM# 261600) is a metabolic genetic disorder characterized by mutations in the phenylalanine hydroxylase (PAH) gene. The PAH enzyme (EC 1.14.16.1) converts phenylalanine into tyrosine in the presence of the cofactor tetrahydrobiopterin (BH_4). A deficiency of this enzyme results in accumulation of phenylalanine in the blood and the brain [Blau et al., 2010]. The neurotoxic effect of hyperphenylalaninemia causes severe mental defects, agitated behavior, eczema, seizures, epilepsy, and some additional symptoms [Paine et al., 1957]. Early diagnosis of PKU is important because it is easily treatable with a low phenylalanine diet and/or with supplements of BH_4 [Bickel et al., 1953; Muntau et al., 2002]. Therefore, in most countries, all newborns are screened for PKU by measuring the amount of phenylalanine in the blood drawn from the heel of the baby and dried onto collection cards, known as the Guthrie test [Guthrie et al., 1963].

Although conventional PKU diagnosis through this Guthrie test is based on the abnormal metabolic phenotype, this technique is not applicable for the detection of carriers of the disease, or for prenatal diagnosis. Hence, it is useful to directly detect the disease-causing mutations in the PAH gene, because the severity of the disease is mutation dependent [Blau et al., 2010]. To date, more than 500 different mutations in the PAH gene have been identified and reported to the PAH Mutation Analysis Consortium Database [http://www.pahdb.mcgill.ca]. Available methods to detect known PAH mutations, include Southern blotting, restriction enzyme digestion, gene sequencing, and denaturing gradient gel electrophoresis (DGGE) [Woo et al., 1983; Lidsky et al., 1985; Riess et al., 1987; DiLeilla et al., 1986; Guldberg et al., 1993; Michiels et al., 1996]. However, these methods are expensive and require a long analysis time, trained personnel and specialized equipment.

To overcome the limitations of the traditional mutation analysis techniques, various large scale technologies are being developed. First, the development of next generation sequencing (NGS) reduces the analysis time, increases the throughput and lowers the cost. But, in order to be widely and routinely used as a diagnostic tool, the purchase price of the system needs to be reduced and data analysis needs to be manageable [Desai et al., 2012]. Next,

DNA microarrays have become one of the most popular analytical techniques for detection of genetic mutations. The advantages of microarrays are the high throughput and robust nature of the technique, but the workflow of microarray-based assays are rather labor- and time-intensive. However, recently developed centrifugal microfluidics might become an elegant solution to automate and speed up microarray hybridization [Chen et al., 2011]. Nevertheless, microarray assays are very expensive, due to the required fluorescent labeling and the read-out infrastructure.

Over the last decades, several electrochemical DNA biosensors have been designed. These biosensors have two major advantages: they are label-free, and the biochemical process is directly translated into an electrical response. All electrochemical DNA biosensors consist of ssDNA probes that are attached to a solid surface, hybridize directly with ssDNA target strands, and use an electrochemical transduction during either the hybridization or the denaturation process. These biosensors are classified based on the nature of the bio-electrochemical transduction. Typical examples of recently developed opto-electronic and electrochemical biosensors include biosensors employing voltammetric read-out. This type of biosensor is often based on the direct oxidation, or redox labeling of DNA, or uses intercalating or soluble redox indicators [Ozkan et al., 2002; Ariksoysal et al., 2005; Farjami et al., 2011; Zhu et al., 2012]. Single nucleotide polymorphism (SNP) discrimination with oxidation-based biosensors is based on the difference in faradic charge or electron transfer through the π-stacking of double-stranded (ds)DNA upon hybridization. The reason for this change is that π-stacking of DNA bases along the helix is interrupted in a mismatched, or heteroduplex, resulting in a decrease of electron transfer efficiency. A low detection limit is achieved when using voltammetry, but mismatch discrimination is limited to short sequences. Since two decades, biosensors based on surface plasmon resonance (SPR) are reported to detect DNA-mutations [Bianchi et al., 1997]. This optical technique can detect mutations based on the difference in refractive index on the sensor chip surface upon hybridization or denaturation of DNA with high sensitivity, but requires expensive and sophisticated benchtop lab equipment as read-out instrumentation[Altintas et al., 2012]. However, a recently developed fiber optic surface plasmon resonance platform (FO-SPR) might become a competitor with

commercially available SPR devices. Nevertheless, up till now, this FO-SPR platform still needs nanoparticle labels for the detection of single-point mutations [Knez et al., 2013]. Finally, impedance spectroscopy is a popular label-free read-out technique to measure the change in interface charge density on semiconductor surfaces during hybridization with, or denaturation of, negatively charged DNA. The change in interface charge density is different for heteroduplex dsDNA, containing a SNP, as compared to homoduplex dsDNA [Vermeeren et al., 2008; van Grinsven et al., 2011]. Although impedance spectroscopy has various advantages, it requires complex data analysis.

Recently, an alternative technique for mutation detection was published [van Grinsven et al., 2012]. This technology is based on the change in heat-transfer resistance (R_{th}) of diamond sensor surfaces upon the thermal denaturation of immobilized dsDNA. The increase of the R_{th} is explained by the morphological changes of dsDNA during denaturation. Immobilized dsDNA molecules up to 50nm, corresponding with 150bp, are upright, rigid structures, allowing heat to be transferred efficiently in between the stiff dsDNA helices. After denaturation, the resulting single-stranded (ss)DNA coils up, covering and insulating the sensor surface. The transition from dsDNA to ssDNA is clearly visible by an increase in R_{th}. The temperature associated with this transition can be used to determine the melting temperature (T_m) of the dsDNA fragments. Based on the difference in T_m, the R_{th}-based sensor was able to detect SNPs during thermal denaturation of short (~10 nm or 30bp) fragments of the PAH gene. The label-free R_{th}-based technique is a promising, inexpensive, fast, and real-time alternative to the currently used denaturation-based techniques for DNA characterization and the detection of point mutations.

However, in order to translate this technique into a simplified multiplexed assay for routine genetic analysis, the R_{th} method must be applicable to longer, optimally exon-size, DNA fragments. When longer fragments, or even entire exons are present as probes on the sensor surface, an entire gene could be screened in only a limited number of assays. In the current study, the maximum DNA length was determined where the R_{th}-based technique was still sensitive to SNPs. Furthermore, we demonstrate the application of this technique by detecting some of the most common SNPs in the PAH gene associated with PKU. These single base mutations are c.473G>A (R158Q),

c.932T>C (p.L311P) and c.1222C>T (R408W) and are respectively located in exon 5, exon 9, and exon 12 of the PAH gene.

5.2 DNA extraction and PCR amplification

5.2.1 DNA extraction

Human genomic DNA (gDNA) was isolated from white blood cells (WBCs), that were extracted from peripheral blood from healthy controls or anonymous homozygous PKU patients, by incubating the cells overnight at 37 °C in lysisbuffer, 20 % SDS and proteinase K. gDNA was then purified using a chloroform-based extraction and ethanol-based precipitation method. Finally, gDNA was resuspended in sterilized milli-Q water (Millipore, Overijse, Belgium).

5.2.2 PCR amplification PAH exon 12

Exon 12 of the PAH gene was amplified in a 20 µl reaction mixture, containing 200 ng of gDNA, 1x PCR buffer with 1.5 mM MgCl2, 0.2 mM of each dNTP, 1 U Taq polymerase, 0.5 µM F primer (5'- GCCTGTGGTTTTGGTCTTAGG-3') and 0.5 µM R primer (5'-ATCTTAAGCTGCTGGGTATTGTC-3', 5'-end modified with a PO_4-label) . The iCycler™ thermal cycler (Bio-Rad, Nazareth, Belgium) was set at 5 minutes denaturation at 95 °C followed by 40 cycles of 2 seconds denaturation at 95 °C, 10 seconds annealing at 53 °C and 30 seconds elongation at 72 °C. After cycling an extra elongation at 72 °C was done for 5 minutes. The phosphorylated PCR products were purified using Sephadex G-50 Medium columns. To generate single-stranded (ss) target DNA, the purified PCR products were treated with Lambda exonuclease. The ssPCR products were purified using Sephadex G-50 Medium columns. The concentration of the purified ssPCR product is determined using a Nanodrop 2000 (Thermo Scientific, Erembodegem, Belgium).

5.3 Functionalization of sensor electrodes with exon-size DNA fragments

For the experiments described in this study, 3 or 300 pmol of exon-size, amino (NH_2)-modified probe ssDNA was covalently immobilized onto carboxyl (COOH)-

terminated nanocrystalline diamond (NCD) sensor electrodes, hereafter referred to as NCD:COOH, using carbodiimide coupling. Details of the synthesis, hydrogenation, and carboxylation of the NCD electrodes, and the coupling procedure for short ssDNA onto NCD are described elsewhere [Vermeeren et al., 2008]. In brief, 10-undecenoic fatty acid (10-UDA) was first photochemically attached to hydrogen (H)-terminated NCD to produce NCD:COOH. In a second step, NH_2-modified ssDNA was covalently linked to the COOH-group using an EDC-mediated coupling.

To evaluate the success of attachment, the immobilized probe DNA sequences were hybridized with 600 pmol of an Alexa Fluor 488-modified detection probe (Table 5.1). The fluorescence of each NCD sample was evaluated using confocal fluorescence microscopy. Settings of the confocal fluorescence microscope are described in section 2.3.3.

For the heat-transfer-based experiments, the immobilized probe DNA sequences were hybridized with 600 pmol of synthetic target DNA (Table 5.2) or with 9 pmol of purified ssPCR product.

5.4 Sensor setup and thermal data analysis

5.4.1 Sensor setup

The thermal denaturation of longer dsDNA fragments on NCD samples was evaluated by monitoring the change in R_{th} due to the transition from dsDNA to ssDNA. The sensor setup is shown in Figure 2.2 and described in section 2.3.5 [van Grinsven et al., 2012]. Briefly, when performing a denaturation experiment, a dsDNA-functionalized NCD sample is attached with its backside to a copper (Cu) lid of the setup and connected with its functionalized front end to a flow cell, filled with 1x PBS buffer. The thermal read-out of the setup consists of two thermocouples monitoring the temperature of both the Cu backside contact (T1) and the liquid compartment of the flow cell (T2). The precision of the thermocouples is experimentally determined as 0.01 °C. Moreover, T1 can be actively steered by adjusting the power (P) of the heating element, connected with the Cu lid of the sensor setup. The R_{th} (°C/W) is derived from the ratio of the temperature difference $\Delta T = T1 - T2$ (°C) and the required heating power P (W), as mathematically described in equation (5.1).

$$R_{th} = \frac{T1 - T2}{P} \quad (5.1)$$

The thermal denaturation of dsDNA fragments on NCD samples was evaluated by monitoring the change in R_{th} derived from the transition from dsDNA to ssDNA. During these measurements the dsDNA fragments on the NCD were denatured by increasing T1 from 35 °C to 85 °C with a heating rate of 1 °C/min. After cooling back down to 35 °C, a second heating run was performed to check if the dsDNA fragments were completely denatured during the first heating run. During these heating runs T1, T2 and P were recorded every second.

5.4.2 Thermal data analysis

For all measured temperatures, the corresponding R_{th} values during the first and second heating run are calculated. The R_{th} change during the first heating run is normalized with the temperature-dependent linear decrease of the R_{th} during the second heating run, to eliminate the temperature-dependent effects on the R_{th} during the first run and only highlight the changes in R_{th} due to biological events. The normalized curves were fitted in Origin 7 (OriginLab, Northampton, MA, USA) with the sigmoidal Boltzmann function as described in equation (5.2):

$$y = \frac{A1 - A2}{1 + e^{(x - x0)/dx}} + A2 \quad (5.2)$$

The parameters A1 (°C/W) and A2 (°C/W) describe the initial and final R_{th} value, corresponding with the R_{th} value before and after denaturation of dsDNA, respectively R_{th}(ds) and R_{th}(ss). The parameter x0 (°C) describes the temperature at which the R_{th} value has reached the center of the transition, thus representing T_m. The parameter dx describes the steepness of the curve. The absolute R_{th} change upon denaturation is described by substracting A1 from A2. Equation (5.2) can also be written using the parameters $R_{th}(T)$ and T_m, as described in equation (5.3):

$$R_{th}(T) = \frac{R_{th}\,ds - R_{th}\,ss}{1+e^{T-T_m/dT}} + R_{th}(ss) \quad (5.3)$$

5.5 Optical confirmation of the functional immobilization of long, exon-size ssDNA fragments onto NCD samples

In order to investigate the sensitivity of R_{th}-based mutation detection in exon-size DNA fragments, the maximum length of ssDNA fragments that can be immobilized on NCD surfaces was optically determined. Four different lengths of probe ssDNA, derived from PAH exon 6, were used. All probe DNA sequences are summarized in Table 5.1. The four probes, 1, 2, 3 and 4, are 87, 127, 167 and 204 bases (b) in length, respectively. Probe 2 represents the average size of a PAH exon. The size of probe 3 is comparable with the persistence length of dsDNA (~150 bp), predicted to be the limiting factor for R_{th} measurements.[24,25] The probe DNA sequences were all modified at the 5'-end with an NH_2-label and a spacer of 7 adenosine (A) bases. To ensure that the NH_2-label is free for immobilization, the probe DNA sequences were denatured for 5 minutes at 95 °C before immobilization.

Table 5.1: Summary of the probe ssDNA sequences used to verify the attachment of exon-size ssDNA fragments to NCD

Name	Size (b)	Sequence (5'-3')
Probe 5.1[a]	87	TGGGCAGCCCATCCCTCGAGTGGAATACATGGAGGAAGAAAAGAAA ACATGGGGCACAGTGTTCAAGACTCTGAAGTCCT
Probe 5.2[a]	127	[probe 5.1]+ TGTATAAAACCCATGCTTGCTATGAGTACAATCACATTTT
Probe 5.3[a]	167	[probe 5.2]+ TCCACTTCTTGAAAAGTACTGTGGCTTCCATGAAGATAAC
Probe 5.4[a]	204	[probe 5.3]+ ATTCCCCAGCTGGAAGACGTTTCTCAATTCCTGCAGA
Detection probe[b]	30	CTGTGCCCCATGTTTTCTTTTCTTCCTCCA

Notes:

[a] Probe sequences were modified at the 5'-end with an NH2-label and a spacer of 7 A bases. All sequences are derived from PAH exon 6. Reference sequence from GenBank: cDNA = NM_000277.1.

[b] Detection probe was modified at the 5'-end with an Alexa Fluor® 488 label. This sequence is complementary to all 4 probe DNA sequences used (in bold).

To evaluate the immobilization of the different probes, the immobilized probe DNA sequences were hybridized with 600 pmol of an Alexa Fluor 488-modified detection probe (Table 5.1), that is completely complementary to all 4 probe DNA sequences used, for 2 hours at 49 °C in 10x PCR buffer. Unbound DNA is removed by rinsing the samples for 30 minutes with sodium chloride/sodium acetate buffer, 2 times concentrated (2x SSC) containing 0.5 % SDS at room temperature (RT). To remove incompletely hybridized DNA, the samples were subsequently rinsed with 0.2x SSC buffer, first at 44 °C for 5 minutes, then at RT for 5 minutes [Vermeeren et al., 2008]. The fluorescence of each NCD sample was measured by confocal fluorescent microscopy. Figure 5.1 a-d illustrates the successful immobilization of all the probe sizes tested. Bleaching experiments confirmed that the fluorescence intensity originates only from the Alexa Fluor 488 dye and not from the underlying diamond layer. Furthermore, no aspecific binding of the detection probe to the diamond surface is detected, as shown in Figure 5.1e.

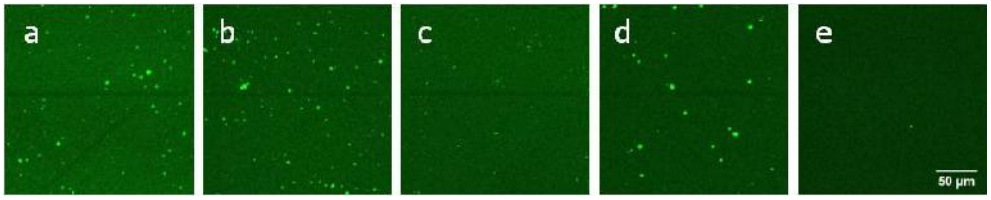

Figure 5.1: Fluorescence images of NCD samples functionalized with ssDNA fragments hybridized to an Alexa FluorÐ 488-labeled detection probe. a. 87b, b. 127b, c. 167b, d. 204 b and e. no ssDNA fragment. Laser intensity is 10 % and detector gain is 1200.

5.6 R_{th}-based denaturation monitoring of synthetic PAH exons

After the successful immobilization, the maximum size of DNA fragments that can be used in R_{th} measurements was determined. Four different probe ssDNA sequences (Table 5.2), containing the wildtype sequences of PAH exon 9, 5, 12 and 7, with different sizes (73 b, 105 b, 130 b and 157 b respectively), were immobilized on NCD sensor electrodes as described above. The DNA selected cover the range of PAH exon sizes from the shortest length (57 bp) to the predicted persistence length of dsDNA (~150 bp), which could be the limiting factor in R_{th} measurements. The immobilized probe DNA sequences were hybridized with 600 pmol of fully complementary, wildtype target ssDNA for 2 hours at 55 °C in 10x PCR buffer, forming homoduplex dsDNA fragments attached to the NCD samples. Incompletely hybridized DNA was removed during stringency washing with 0.2x SSC buffer at a temperature of 50 °C.

Table 5.2: Summary of the probe and target ssDNA sequences used in the R_{th} measurements

Name	Size (b)	Sequence (5'-3')
Probe 5.5[a,b]	73	GGACTTACTGTGGCGAGCTTTTCAATGTATTCATCAGGTGCACCC AGAGAGGCAAGGCCAATTTCC
Target 5.1[b]	66	GGAAATTGGCCTTGCCTCTCTGGGTGCACCTGATGAATACATTG AAAAGCTCGCCACAGTAAGTCC
Target 5.2[b]	66	GGAAATTGGCCTTGCCTCTCCGGGTGCACCTGATGAATACATTG AAAAGCTCGCCACAGTAAGTCC
Probe 5.6[a,c]	105	GGCAGACTTACTGGCGGTAGTTGTAGGCAATGTCAGCAAACTGC TTCCGTCTTGCACGGTACACAGGATCTTTAAAACCCTAGGAGAAA AGAGACACC
Target 5.3[c]	98	GGTGTCTCTTTTCTCCTAGGGTTTTAAAGATCCTGTGTACCGTGCA AGACGGAAGCAGTTTGCTGACATTGCCTACAACTACCGCCAGTA AGTCTGCC
Target 5.4[c]	98	GGTGTCTCTTTTCTCCTAGGGTTTTAAAGATCCTGTGTACCGTGCA AGACAGAAGCAGTTTGCTGACATTGCCTACAACTACCGCCAGTA AGTCTGCC
Probe 5.7[a,d]	130	CTTACTGTTAATGGAATCAGCCAAAATCTTAAGCTGCTGGGTAT TGTCCAAGACCTCAATCCTTTGGGTGTATGGGTCGTAGCGAACT GAGAAGGGCCGAGGTATTGTGGCAGCAAAGTTCCT
Target 5.5[d]	123	AGGAACTTTGCTGCCACAATACCTCGGCCCTTCTCAGTTCGCTA CGACCCATACACCCAAAGGATTGAGGTCTTGGACAATACCCAG CAGCTTAAGATTTTGGCTGATTCCATTAACAGTAAG

Name	Size (b)	Sequence (5'-3')
Target 5.6[d]	123	AGGAACTTTGCTGCCACAATACCTTGGCCCTTCTCAGTTCGCTA CGACCCATACACCCAAAGGATTGAGGTCTTGGACAATACCCAG CAGCTTAAGATTTTGGCTGATTCCATTAACAGTAAG
Probe 5.8[a,e]	157	TACTCACGGTTCGGGGGTATACATGGGCTTGGATCCATGTCTGA TGTACTGTGTGCAGTGGAAGACTCGGAAGGCCAGGCCACCCAA GAAATCCCGAGAGGAAAGCAGGCCAGCCACAGGTCGGAGGCG GAAACCAGTGCAAGCTGGGAT
Target 5.7[e]	150	ATCCCAGCTTGCACTGGTTTCCGCCTCCGACCTGTGGCTGGCCTG CTTTCCTCTCGGGATTTCTTGGGTGGCCTGGCCTTCCGAGTCTT CCACTGCACACAGTACATCAGACATGGATCCAAGCCCATGTATA CCCCCGAACCGTGAGTA

Notes:

[a] Probe sequences were modified at the 5'-end with an NH_2-label and a spacer of 7 A bases

[b] Sequences encloses PAH exon 9 (in bold). [c] Sequences encloses PAH exon 5 (in bold).

[d] Sequences encloses PAH exon 12 (in bold). [e] Sequences encloses PAH exon 7 (in bold).

[b, c, d, e] Reference sequence from GenBank: cDNA=NM_000277.1

The thermal denaturation of each NCD sample was evaluated by monitoring the change in R_{th}. The normalized R_{th} (N. R_{th}) of the selected DNA fragments used in this study, as a function of increasing T1, is shown in Figure 5.2. An increase in R_{th} can be observed upon denaturation of dsDNA fragments representing PAH exon 9, exon 5 and exon 12 with corresponding sizes of 66 bp (Figure 5.2a), 98 bp (Figure 5.2b) and 123 bp (Figure 5.2c). No R_{th} change was observed when using dsDNA fragments of 150 bp, representing exon 7 (Figure 5.2d).

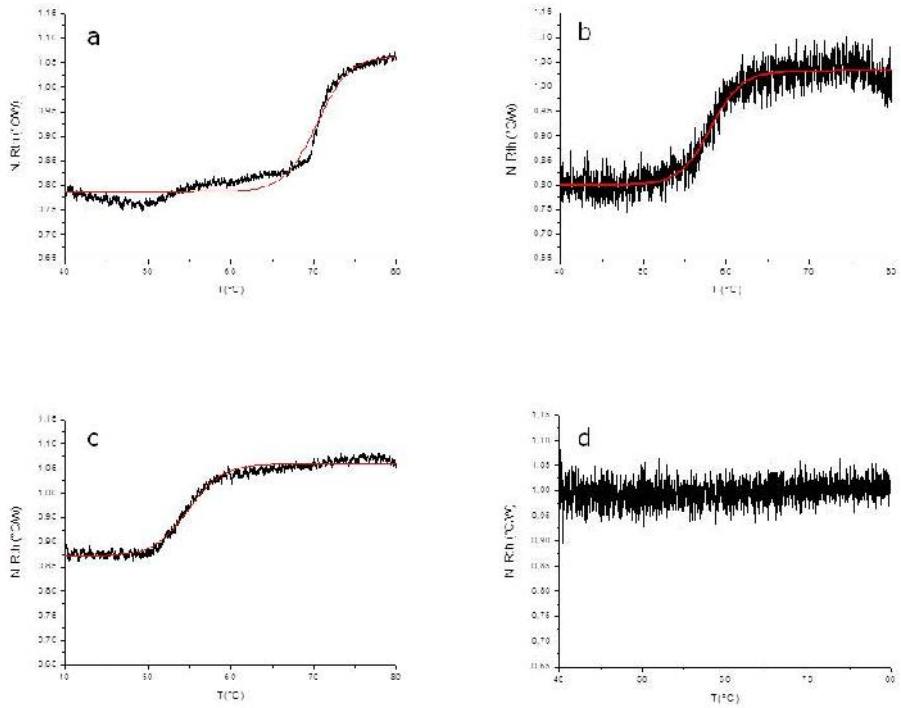

Figure 5.2: N. R_{th} in function of temperature T1 (black lines) during the thermal denaturation of fully complementary dsDNA sequences with different fragment sizes. a. 66 bp, enclosing exon 9, b. 98 bp, enclosing exon 5, c. 123 bp, enclosing exon 12 and d. 150 bp, enclosing exon 7. The Boltzmann fit is represented by a red line.

The fit of the normalized curves with the sigmoidal Boltzmann function is represented by a red line in Figure 5.2 a, b and c. The values of the corresponding parameters representing T_m (x0), the R_{th} value of dsDNA (A1), the R_{th} value of ssDNA (A2) and the R_{th} change upon denaturation (A1-A2) are summarized in Table 5.3. Exon 9 has the highest T_m of 70.37±0.04 °C, exon 5 has an intermediate T_m of 58.08±0.05 °C and exon 12 has the lowest T_m of 54.81±0.03 °C.

Table 5.3: Summary of the parameters defined by the sigmoidal Boltzmann function (equation 2) used to fit the R_{th} data during thermal denaturation of fully complementary homoduplex dsDNA fragments of 3 different sizes. Reported uncertainties are standard errors as obtained from the data fits.

	Exon 9 66 bp	Exon 5 98 bp	Exon 12 123 bp
x0[a] (°C)	70.37±0.04	58.08±0.05	54.81±0.03
A1[b] (°C/W)	0.7868±0.0005	0.8000±0.0009	0.8715±0.0004
A2[c] (°C/W)	1.064±0.001	1.0311±0.0009	1.0590±0.0003
(A2-A1) ò 100[d] (%)	28	23	19

Notes:

[a] Fitted T_m, rounded to 0.01 °C precision

[b] Fitted R_{th} value of dsDNA

[c] Fitted R_{th} value of ssDNA

[d] Relative R_{th} change upon denaturation, rounded to 2 significant digits

The average, relative increase in R_{th} upon denaturation is 23 %. However, A2 is an overestimation of the R_{th} value of ssDNA fragments, as measured in the second heating run. Therefore an average, relative increase in R_{th} of 18 % is more correct. This value is obtained by substracting the average value of A1 (0.81943 °C/W) from the theoretical A2 value of the second heating run (1,00000 °C/W) and this value multiplied by 100 %.

5.7 R_{th}-based detection of SNPs in synthetic PAH exons

After demonstrating that R_{th} can be used to monitor DNA denaturation in exon-size DNA fragments, the R_{th}-based detection of SNPs in these DNA fragments was evaluated as a proof of principle. The previous wildtype probe DNA sequences (Table 5.2) were immobilized on NCD samples as described above. The immobilized probe DNA sequences were hybridized with either 600 pmol target DNA containing a PAH mutation, forming a heteroduplex on the NCD, or with 600 pmol target DNA that was fully complementary, forming a homoduplex on the NCD. PAH mutations tested are c.473G>A (R158Q), c.932T>C (p.L311P), and c.1222C>T (R408W). The hybridization and stringency washing temperatures for both types of target DNA used are 55 °C and 50 °C,

respectively. The R_{th} change during denaturation of the dsDNA fragments containing a SNP on one NCD sample was compared with the change obtained during denaturation of fully complementary dsDNA sequences on another NCD sample.

The N. R_{th} as a function of T1 is shown in Figure 5.3. The fit of the normalized curve with the sigmoidal Boltzmann function is represented by a red line.

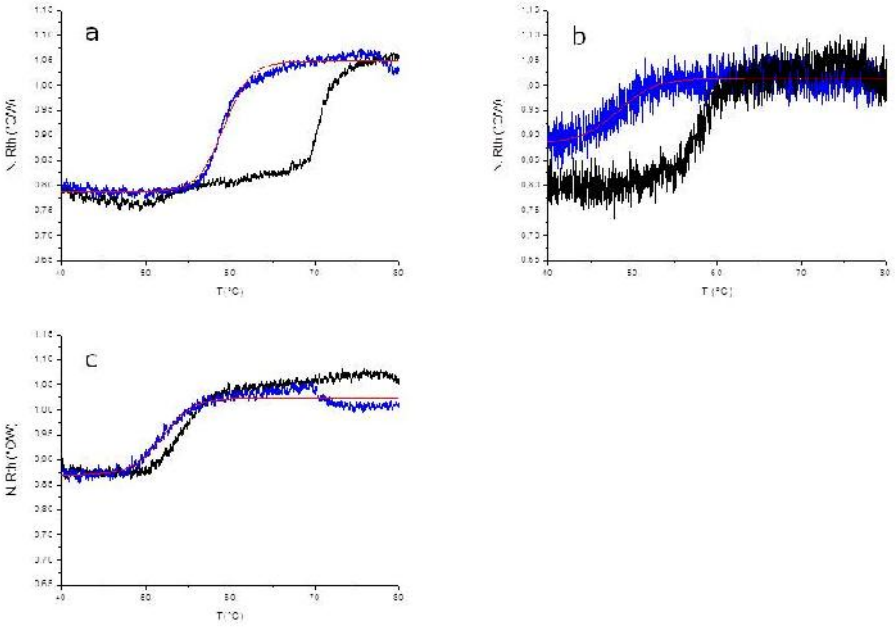

Figure 5.3: N. R_{th} in function of temperature T1 during the thermal denaturation of heteroduplex dsDNA fragments (blue lines) compared with the thermal denaturation of fully complementary dsDNA sequences (black lines). The heteroduplex dsDNA fragments contain one of the following SNPs: c.932T>C (p.L311P) (a), c.473G>A (R158Q) (b) or c.1222C>T (R408W) (c). The Boltzmann fit is represented by a red line.

The values of the corresponding parameters representing T_m (x0), the R_{th} value of dsDNA (A1), the R_{th} value of ssDNA (A2) and the R_{th} change upon denaturation (A1-A2) are summarized in Table 5.4. The T_m for heteroduplex

dsDNA of exon 9 is 59.24±0.02 °C, for exon 5 is 48.24±0.14 °C and for exon 12 is 51.97±0.04 °C.

Table 5.4: Summary of the parameters defined by the sigmoidal Boltzmann function (equation 2) used to fit the R_{th} data during thermal denaturation of heteroduplex dsDNA fragments. Reported uncertainties are standard errors as obtained from the data fits.

	Exon 9 c.932T>C p.L311P	Exon 5 c.473G>A R158Q	Exon 12 c.1222C>T R408W
x0[a] (°C)	59.24±0.02	48.24±0.09	51.97±0.04
A1[b] (°C/W)	0.7871±0.0004	0.884±0.002	0.8702±0.0007
A2[c] (°C/W)	1.0475±0.0003	1.0138±0.0005	1.0240±0.0003
(A2-A1) ò 100[d] (%)	26	13	15

Notes:

[a] Fitted T_m, rounded to 0.01 °C precision

[b] Fitted R_{th} value of dsDNA

[c] Fitted R_{th} value of ssDNA

[d] Relative R_{th} change upon denaturation, rounded to 2 significant digits

When comparing these values of heteroduplexes containing a SNP (Table 5.4) with the fully complementary, homoduplexes (Table 5.3), a decrease of T_m can be observed for the heteroduplex denaturations. Furthermore, the average, relative increase in R_{th} upon denaturation of heteroduplex dsDNA fragments containing a SNP (Table 5.4) is 18 %, as calculated from the fitted values A1 and A2. Although A2 is an overestimation of the R_{th} value of ssDNA fragments, as measured in the second heating run. Therefore an average, relative increase in R_{th} of 15 % is more correct. This value is obtained by subtracting the average value of A1 (0.84701 °C/W) from the theoretical A2 value of the second heating run (1.00000 °C/W) and this value multiplied by 100 %.

In case of exon 12, R_{th}-measurements were performed in threefold. A significant difference ($p<0.05$) is obtained between the T_m of fully complementary dsDNA fragments (58.68±4.56 °C) and dsDNA fragments

containing the c.1222C>T point mutation (50.84±1.19 °C) according to the Student T-test.

5.8 R_{th}-based detection of SNPs in patient-derived and healthy control PAH exons

As a proof-of-concept, NCD samples functionalized with 3 pmol of synthetic probe 7 were hybridized with 9 pmol of ssPCR product from a healthy control or from a homozygous PKU patient containing the c.1222C>T (R408W) SNP. N. R_{th} as a function of increasing T1 is shown in Figure 5.4. The fit of the normalized curve with the sigmoidal Boltzmann function is represented by a red line.

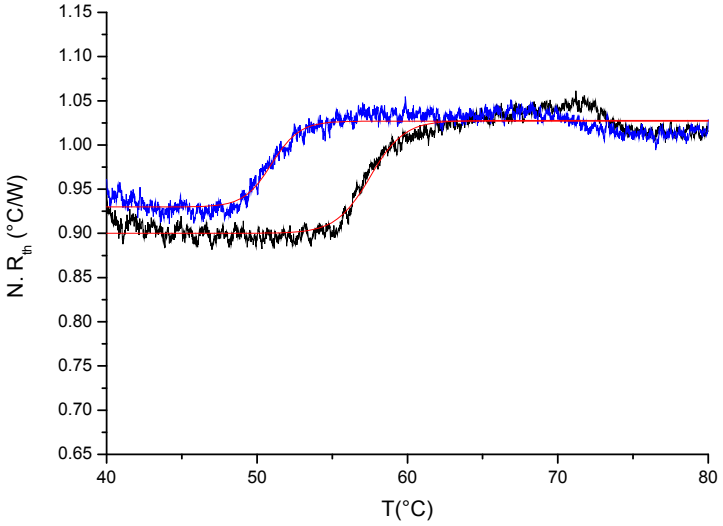

Figure 5.4: N. R_{th} in function of temperature T1 during the thermal denaturation of PCR products containing exon 12 of a healthy control (black line) compared with exon 12 of a homozygous PKU patient having the c.1222C>T (R408W) SNP (bleu lines). The Boltzmann fit is represented by a red line.

The values of the corresponding parameters representing T_m (x0), the R_{th} value of dsDNA (A1), the R_{th} value of ssDNA (A2) and the R_{th} change upon denaturation (A1-A2) are summarized in Table 5.5.

Table 5.5: Summary of the parameters defined by the sigmoidal Boltzmann function (equation 5.2) used to fit the R_{th} data during thermal denaturation of PCR products containing exon 12. Reported uncertainties are standard errors as obtained from the data fits.

	Healthy control	Homozygous PKU patient (R408W)
x0[a] (°C)	57.52±0.03	50.96±0.03
A1[b] (°C/W)	0.9001±0.0004	0.9298±0.0005
A2[c] (°C/W)	1.0278±0.0003	1.0270±0.0003
(A2-A1) ò 100[d] (%)	13	10

Notes:

[a] Fitted T_m, rounded to 0.01 °C precision

[b] Fitted R_{th} value of dsDNA

[c] Fitted R_{th} value of ssDNA

[d] Relative R_{th} change upon denaturation, rounded to 2 significant digits

The T_m of exon 12 from the healthy control is 57.52±0.03 °C and from the homozygous patient is 50.96±0.03 °C. When comparing these values with the values of synthetic target DNA fragments (Table 5.3 and Table 5.4) a similar decrease in T_m can be observed.

5.9 Discussion

In a previous study, it was demonstrated that the transition from dsDNA to ssDNA during thermal denaturation results in an increase in R_{th}. The temperature associated with the R_{th} change can be used to determine the T_m of dsDNA fragments. Based on the difference in T_m, this R_{th}-based sensor was able to detect SNPs during thermal denaturation of short dsDNA fragments of the PAH gene.[24]

In the current study, the R_{th}-based sensor was evaluated for possible use in routine genetic analysis. Therefore, it would be advantageous if the R_{th} method was applicable to longer, ideally even exon-size DNA fragments to simplify the development of a multiplex assay for screening an entire gene. First, the maximum length of ssDNA fragments that can be immobilized on NCD

surfaces was optically determined. Next, the occurrence of an R_{th} change upon denaturation of such longer dsDNA fragments was evaluated. And finally, the sensitivity of the R_{th}-based technique to SNPs in these longer dsDNA fragments was studied. As a proof-of-concept, the detection of some of the most common SNPs in the PAH gene associated with PKU were analyzed. These single base mutations are c.473G>A (R158Q), c.932T>C (p.L311P) and c.1222C>T (R408W) and are respectively located in PAH exon 5, exon 9, and exon 12.

It was demonstrated, by the use of confocal fluorescence microscopy, that is was possible to immobilize ssDNA fragments up to 200 b in length onto NCD samples. This length is similar to the length of the longest exon in the PAH gene: exon 6. Therefore, it is possible to immobilize all exons of the PAH gene onto COOH:NCD samples using an optimized version of the EDC-mediated coupling procedure.[22] This optimization entailed the denaturation of the probe ssDNA prior to immobilization, to ensure that the NH_2-label is free for immobilization and is not encapsulated by hairpins or other secondary structures of the longer probe ssDNA. This immobilization strategy is not limited to the exons of the PAH gene, but can be extended to other genes as well, since this procedure is sequence-independent. However, the fluorescence intensities shown in Figure 5.2 are lower in comparison with the fluorescence resulting from the immobilization of short (8 b and 36 b) DNA fragments [Vermeeren et al., 2008]. Furthermore, the intensity decreases with increasing length. A possible explanation is a lower surface coverage with longer ssDNA fragments. This decrease in coverage is presumed to be associated with a less ordered arrangement of longer ssDNA fragments on a surface, reflecting a more flexible ssDNA configuration [Steel et al., 2000]. The persistence length of ssDNA fragments is experimentally found to be ~2nm [Wenmackers et al., 2009]. Therefore, longer ssDNA fragments might cover up the NCD surface, thereby blocking larger regions of adjacent surface space for additional functionalization [Vermeeren et al., 2008]. Another explanation is that bending of the longer ssDNA fragments towards the NCD surface causes fluorescence quenching [Sakon et al., 2009]. The brighter fluorescence spots are possibly due to an accumulation of the immobilized probe DNA on the grain boundaries of the NCD sample, where a hotspot of hybridized detection probe can be formed.

After the successful attachment, the maximum length of dsDNA still allowing to measure R_{th} changes due to conformational changes in DNA upon denaturation was investigated by the thermal denaturation of fully complementary homoduplex dsDNA fragments with lengths up to the predicted dsDNA persistence length of 150 bp. An increase in R_{th} could be observed upon denaturation of dsDNA fragment length up to 123 bp. This increase illustrates the transition from upright dsDNA molecules, allowing efficient heat-transfer, to highly flexible ssDNA fragments, insulating the sensor surface [van Grinsven et al., 2012]. The temperature associated with this transition can be used to determine the T_m of the dsDNA fragments. In this paper a uniform procedure to evaluate R_{th} measurements is proposed to calculate the T_m, instead of estimating it, as previously described [van Grinsven et al., 2012]. This procedure consists of two steps. First, the R_{th} change is normalized to the linear decrease of the R_{th} with increasing temperatures. The decrease in R_{th} is due to an increase in power to compensate for the heat loss from the sensor setup to the surrounding environment at higher temperatures. In a second step, the normalized curves were fitted with the sigmoidal Boltzmann function (equation 2). The parameters in this equation describe the absolute R_{th} change upon denaturation and the corresponding T_m in a standardized approach. The somewhat noisy appearance of the N. R_{th} graphs shown are related to the fact that the required heating power shows small fluctuations within short time intervals. In Figure 5.2a and c and Figure 5.3a and c the noise level on the R_{th} is decreased by a factor of 3, by improving the noise on the heating power [Geerets et al., 2013].

The absolute R_{th} change upon denaturation slightly decreases with increasing DNA lengths, due to an increase in initial R_{th} value of dsDNA fragments (A1) with increasing lengths. A feasible explanation is that the longer dsDNA fragments become, the more they approach the persistence length of dsDNA and tend to curve instead of remain upright. This will disturb the heat-transfer through the spaces in between the immobilized dsDNA fragments, resulting in a decreased resolution between ssDNA and dsDNA, shown by a decreased absolute R_{th} change upon denaturation. This is illustrated by the fact that no R_{th} change was observed when using DNA fragments of 150 bp, corresponding to the persistence length of dsDNA.

Furthermore, the R_{th} change upon denaturation, as measured in the first heating run, is larger than the actual R_{th} of ssDNA fragments, as measured in the second heating run. A possible explanation for this phenomenon is the formation of a transition state during the denaturation process, as described in DGGE and TGGE experiments [Wartell et al., 1998]. The single stranded portion of the partially melted molecules can form branches which probably have a higher R_{th} value than ssDNA. Another explanation is that the higher R_{th} value is caused by the denaturated, untethered ssDNA strands that interacts with the surface, causing a higher insulation of the NCD surface. After some time this interaction is broken, causing a drop in R_{th}, as illustrated in Figure 5.3c [Qamhieh et al., 2009]. Finally, to investigate the use of R_{th} in detecting SNPs in longer dsDNA fragments, the temperature associated with the R_{th} change is studied in more detail. This temperature reflects the T_m of the studied dsDNA fragments. The T_m of heteroduplex dsDNA fragments containing a SNP is lower than the T_m of homoduplex dsDNA fragments. Based on the difference in T_m, SNPs could be detected by using the R_{th} technique by comparing the temperature of the R_{th} change during denaturation of heteroduplex dsDNA fragments containing a SNP with the temperature of the R_{th} change during denaturation of fully complementary homoduplex dsDNA sequences. The temperature at which half of the R_{th} change occurred (x0) during the denaturation of the heteroduplex dsDNA fragments is decreased compared to the temperature at which half of the R_{th} change occurred (x0) during the denaturation of the fully complementary homoduplex dsDNA fragments. This is due to the fact that heteroduplex dsDNA fragments containing a SNP are less stable than homoduplex dsDNA fragments, resulting in lower T_m. This was demonstrated by the R_{th}-based detection of following SNPs, c.473G>A (R158Q), c.932T>C (p.L311P) and c.1222C>T (R408W) in synthetic fragments encompassing PAH exon 5, exon 9, or exon 12. The effect was confirmed in a proof-of-application setting when using the PCR product from exon 12 of a healthy control or a homozygous PKU patient having the c.1222C>T (R408W) SNP.

The results in this study indicate that R_{th} can be used to detect homozygous mutations in exon-length DNA fragments of PKU patients. In future work the R_{th}-based detection of heterozygous mutations in exon-length DNA

fragments of PKU carriers will be investigated. Therefore, the NCD will be functionalized with exon-length probe DNA fragments containing a SNP or no SNP, each in isolated areas on the surface. In a next step, all probes will be hybridized in high stringent conditions with exon-length target DNA fragments from PKU carriers. The thermal denaturation will result in a bipartite R_{th} change, reflecting the denaturation of the different dsDNA fragments present on the NCD surface [Bers et al., 2013]. The bipartite R_{th} change can be fitted with the function as described in equation (5.3):

$$y = \frac{A1-A2}{1+e^{\frac{x-x01}{dx1}}} + \frac{A2-A3}{1+e^{\frac{x-x02}{dx2}}} + A3 \quad (5.3)$$

The parameter A1 (°C/W) describes the R_{th} value before denaturation of the dsDNA fragments. The parameters A2 (°C/W) and A3 (°C/W) describe respectively the R_{th} value after denaturation of the mutated sequences and after denaturation of the fully complementary sequences. The parameters x01 (°C) and x02 (°C) describe respectively the melting temperature of the mutated sequences and the melting temperature of the fully complementary sequences.

Hence, for the detection of heterozygous mutations, the sensor needs to be converted to an array-based system. However, the R_{th}-based technique is more cost effective than conventional microarray systems because of its label-free character and simple instrumentation.

5.10 Conclusion

R_{th} was evaluated as an alternative method to detect PKU-related mutations in a label-free and real-time manner during the thermal denaturation of entire PAH exons. The R_{th} effect reflects the change in DNA morphology while going from double-stranded, allowing effective heat-transfer, to single-stranded DNA, insulating the electrode surface against heat-transfer. The temperature at which this R_{th} shift occurs, reflects the T_m of the dsDNA, implying SNP sensitivity. It was shown that the Rth increase during the denaturation of homoduplex dsDNA, formed between a wildtype exon probe and a healthy control exon target, was thermally separated from the R_{th} increase during the denaturation of heteroduplex dsDNA, formed between a wildtype exon probe and an exon target

of a PKU patient. This was limited by the length of the attached dsDNA, since the closer the length approaches the persistence length of dsDNA, the lower the resolution between dsDNA and ssDNA will become. This was evident by the absence of an R_{th} effect in exon 7, but will easily be resolved by the separation of the exon into two shorter, overlapping fragments. In order to allow the R_{th}-based technique to be used in routine genetic screening, heterozygous mutation detection will need to be addressed.

6

IMPEDIMETRIC DETECTION OF C-REACTIVE PROTEIN

Partly based on:

Impedimetric, diamond-based immunosensor for the detection of C-reactive protein

Vermeeren V., Grieten L., Vanden Bon N., Bijnens N., Wenmackers S., Janssens S.D., Haenen K., Wagner P. and Michiels L.

Sensors and Actuators B: Chemical 2011; 157(1), 130 – 138

Own contribution: Suggesting the detection of CRP in serum samples, biofunctionalization sensor electrodes, suggesting and performing the impedimetric and optical measurements, suggesting the reproducibility experiments in serum, data processing using OriginLab, discussing the results and co-editing the manuscript.

Abstract

In the framework of developing a fast and label-free immunosensor for C-reactive protein (CRP), a risk factor for cardiovascular diseases (CVD), anti-CRP antibodies were physically adsorbed to the hydrogen-terminated surface of nanocrystalline diamond (NCD:H). Both fluorescence microscopy and Enzyme-Linked ImmunoSorbent Assay (ELISA) reference techniques showed that this was a suitable substrate for antibody functionalization and antibody-antigen recognition reactions. Electrochemical Impedance Spectroscopy (EIS) was used to electronically detect CRP recognition. The specificity of the immunosensor was demonstrated by incubation with plasminogen as a reference molecule. A different impedance behavior was observed in real-time after CRP addition as compared to plasminogen addition: the impedance increased only during CRP incubation. Fitting the data showed that this corresponded with a decrease in capacitance of the molecular layer due to its increased thickness by specific CRP recognition. Sensitivity experiments in real-time showed a clear discrimination between 125µg/mL, 12.5µg/mL and 1.25µg/mL of CRP after 10 minutes at 100 Hz. Since 1.25µg/mL of CRP was still clearly distinguishable from buffer solution, our CRP-directed immunosensor prototype reaches a sensitivity that is within the physiologically relevant concentration range of this biomarker in healthy controls and CVD patients. Moreover, this prototype displayed real-time discriminating power between spiked and unspiked serum, and thus also shows its applicability in this biological matrix.

6.1 Introduction

C-reactive protein (CRP) is an acute phase protein that is produced in the liver. In its native form, it is a pentamer of 126kDa, consisting of five identical monomers of 25kDa each. Its serum level increases rapidly during systemic inflammation, where it assists in complement binding to foreign and damaged cells. Through this mechanism, phagocytosis is enhanced by macrophages, that express a receptor for CRP. There is also evidence that CRP increases the expression of the cell adhesion molecules ICAM-1, VCAM-1 and E-selection in cultured endothelial cells [Pasceri et al., 2000]. Therefore, CRP has traditionally been used as a reliable marker for tissue injury, infection, and inflammation. However, studies have shown that CRP is also implicated in the development of cardiovascular diseases (CVD), such as atherosclerosis, angina, coronary heart disease, peripheral artery disease, myocardial infarction, and stroke [Haverkate et al., 1997]. Not only can elevated blood levels of CRP predict the recurrence of coronary events in patients with stable or unstable angina [Haverkate et al., 1997], but it can even determine an increased risk for hypertension [Sesso et al., 2003] and CVD in healthy controls [Ridker et al., 1997]. CRP serum levels of < 1µg/mL are considered normal, while levels > 3.13µg/mL indicate an increased risk for CVD. As a result, CRP can serve as an important risk assessment factor for the development of CVD [Ridker et al., 1997].

The most recent statistics from the American Heart Association report that in 2009, 83.6 million Americans suffered from CVD, of whom 787931 actually died in 2009. It is estimated that 2150 Americans die of CVD each day [Heart disease and Stroke statistics – 2013 update]. Hence, the need for reliable and sensitive risk assessment is obvious. Over the years, many assay methods for the detection of CRP have been developed and improved, such as latex agglutination, nephelometry, turbidimetry, and fluorescent polarization [Hokama et al., 2006]. Currently, an Enzyme-Linked ImmunoSorbent Assay (ELISA)-based blood test called the 'highly sensitive C-reactive protein (hs-CRP) assay' is available to determine CVD risk (Dade Behring, Inc., now Siemens Medical, Illinois, USA). Its limit of detection is 0.1µg/mL. However, disadvantages of ELISA tests are the long reaction times (several hours) of the multiple steps involved, and the requirement of trained personnel and expensive reagents [Hu

et al., 2006]. A Surface Plasmon Resonance (SPR) biosensing platform for CRP was developed by Hu et al., where anti-CRP antibodies were bound to a Au surface through Protein G. They reached a detection limit of 1 µg/mL of purified CRP [Hu et al., 2006]. Meyer et al. also established an immunosensor for CRP detection based on SPR. The detection principle was based on two different anti-CRP antibodies: one for CRP entrapment and one for labeling. A linear detection range of 2 – 5µg/mL CRP in PBS buffer was found [Meyer et al., 2006]. Recently, the same authors developed a novel CRP detection method in crude serum, urine, and saliva samples based on magnetic detection. With its linear detection range from 25ng/mL to 2.5µg/mL, it showed to be even more sensitive than the hs-CRP ELISA assay [Meyer et al., 2007]. In the last years, the focus on Electrochemical Impedance Spectroscopy (EIS)-based immunosensing methods for various targets has increased significantly. These impedimetric immunosensors are usually based on capacitive changes or changes based on charge-transfer resistance. Cooreman et al. investigated the interaction between the semiconducting polymer poly[2-methoxy-5-(3,7-dimethyloctyloxy)]-1,4-phenylenevinylene (MDMO-PPV) and physically adsorbed antibodies against the fluorescent dyes FITC and Cy5. Specific antigen-antibody recognition was demonstrated based on EIS. These antibody-modified polymer films show a clear response to 1.13µg/mL of antigen solution, with a time constant of 2 to 3 minutes [Cooreman et al., 2005]. Ionescu et al. devised an impedimetric Au-based immunosensor against the antibiotic ciprofloxacin. A detection limit of 10pg/mL was reached [Ionescu et al., 2007]. Yang et al. used EIS to directly detect antigen-antibody binding. They covalently bound human IgG and IgM, serving as antigens, to aldehyde-terminated nanocrystalline diamond (NCD) surfaces using a glyceraldehyde crosslinker. The antibodies were detected in real-time using anti-IgG and anti-IgM [Yang et al., 2007]. In this study, we will adsorb monoclonal anti-CRP antibodies onto hydrophobic H-terminated NCD, allowing CRP recognition to occur through a typical antigen-antibody interaction via the hypervariable regions of anti-CRP, adding clinical relevance to our immunosensor setup in comparison with the work of Yang et al. [Yang et al., 2007].

Diamond has been studied as a novel transducer material for biosensor fabrication because of very appealing physical, optical, chemical and electrical

characteristics. For a complete overview, the reader is referred to the works of Field and Swain [Swain et al., 1993; Field et al., 1987]. Among others, it has a wide electrochemical window, and, although an insulator with a very wide band gap of 5.5eV, it can be made electrically conductive by chemical doping [Yamanaka et al., 2000; Pernot et al., 2010; Haenen et al., 2009]. These electrical properties of diamond have already been exploited in the construction of diamond-based field-effect transistors (FET) using technologies that are compatible with lithographic methods [Rezek et al., 2002; Sasaki et al., 2010]. Moreover, diamond is biocompatible, allowing in vivo applications [Tang et al., 1995] and it can be functionalized with biomolecules. Although diamond is chemically inert, Takahashi et al. surmounted this barrier by the photochemical activation of H-terminated diamond surface [Takahashi et al., 2000]. The way was paved towards further modification of diamond with biomolecules, such as DNA and proteins. Nowadays, also wet chemical [Ushizawa et al., 2002], electrochemical [Wang et al., 2004; Shin et al., 2006; Uetsuka et al., 2007], and photochemical [Christiaens et al., 2006; Vermeeren et al., 2008; Yang et al., 2002; Härtl et al., 2004] methods exist to functionalize diamond surfaces. The reader is referred to the article of Wenmackers for an extensive review on functionalization and read-out techniques of DNA on diamond [Wenmackers et al., 2009]. In our previous work, it was demonstrated that real-time differentiation between fully complementary and 1-mismatch DNA was possible on lightly boron (B)-doped NCD substrates using EIS [Vermeeren et al., 2007]. In order to achieve a more generic, flexible biosensor platform, this same NCD- and EIS-based setup was developed in an immunosensing application.

6.2 Characterization of sensor electrodes

6.2.1 Confocal fluorescence microscopy

The most reproducible and straight forward method of receptor layer immobilization, similar as in ELISA experiments, is physisorption. Different substrates were tested such as diamond, Si, quartz and Si dioxide, but only the diamond surface was capable of protein adsorption. Antibodies adsorb on both oxidized and hydrogenated diamond. These proteins serve as the receptor layer in the future immunosensing experiments as described below. In this project,

anti-CRP antibodies will be used as functional receptor layer. In order to obtain visual and qualitative information on antibody adsorption on NCD surfaces, 20nM anti-IgG antibodies labeled with an Alexa Fluor® 488 dye (Ab-Al488) were adsorped on the NCD sample, as described in Section 2.2.2

In Figure 6.1 a fluorescence image of Ab-Al488's incubated on hydrogenated NCD (NCD:H) is shown. A photobleaching line indicates that the fluorescence originates from the labeled antibodies and not from background reflection.

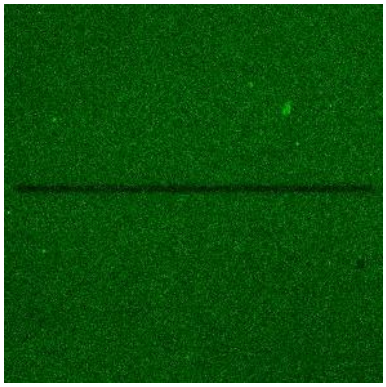

Figure 6.1: Fluorescence image (220x220µm) of Ab-Al488's on NCD:H. Size image is 220x220µm, recorded with gain 850.

6.2.2 ELISA

To verify the functionality of these adsorbed antibodies, two NCD:H samples were coated with 3.00µg/mL unlabeled anti-CRP antibodies and 6 % BSA, as described in paragraph 2.2.4. To examine the non-specific adsorption of CRP and AP-labeled anti-CRP antibodies to diamond, two additional NCD:H samples were only coated with 6 % BSA. For both NCD couples (anti-CRP-coated and BSA-coated), one sample was treated with CRP, while the other was incubated with CRP buffer. The negative control samples (coated or uncoated with anti-CRP) treated with CRP buffer, provided insight in the non-specific adsorption of AP-labeled anti-CRP antibodies to coated or uncoated NCD. The negative control sample that was not coated with anti-CRP but was treated with CRP indicated

the amount of non-specific CRP adsorption to NCD. Detection occurred with an AP-labeled anti-CRP antibody and an AP-based substrate reaction. The absorption of the colored product was determined at 405nm. From 3 independent measurements, it was clear that the absorption is the highest for the sample allowing the formation of the antibody/antigen-complex, with minimal contributions due to non-specific adsorption (Figure 6.2). NCD:H was therefore considered a suitable substrate for antibody adsorption, as the biological functionality of the antibodies are retained.

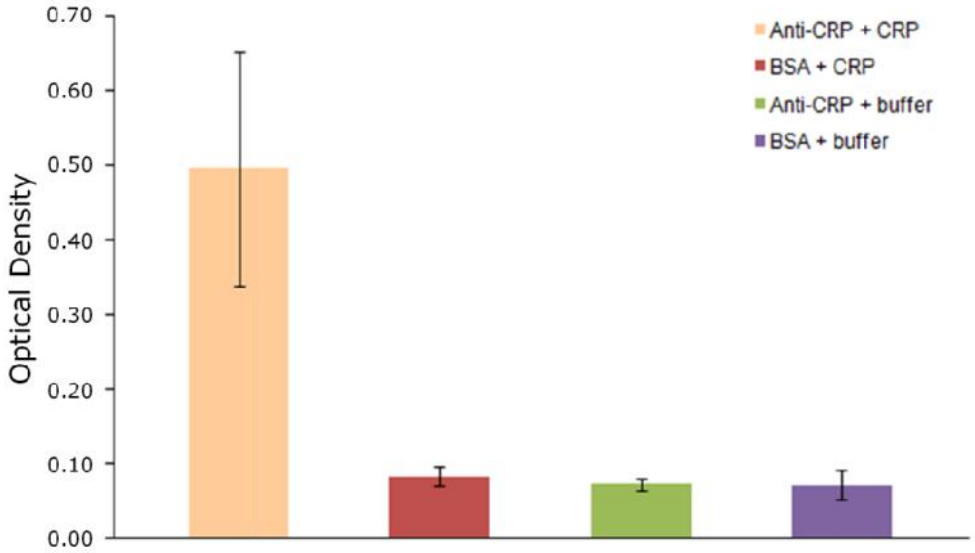

Figure 6.2: Colorimetric measurement of differently functionalized NCD samples. The data are generated from 3 indepedent measurements, with corresponding standard deviations.

6.3 Sensor setup

The sensor setup devised for the development of a CRP-sensitive immunosensor is displayed in Figure 6.3 and described in detail in section 2.2.5.

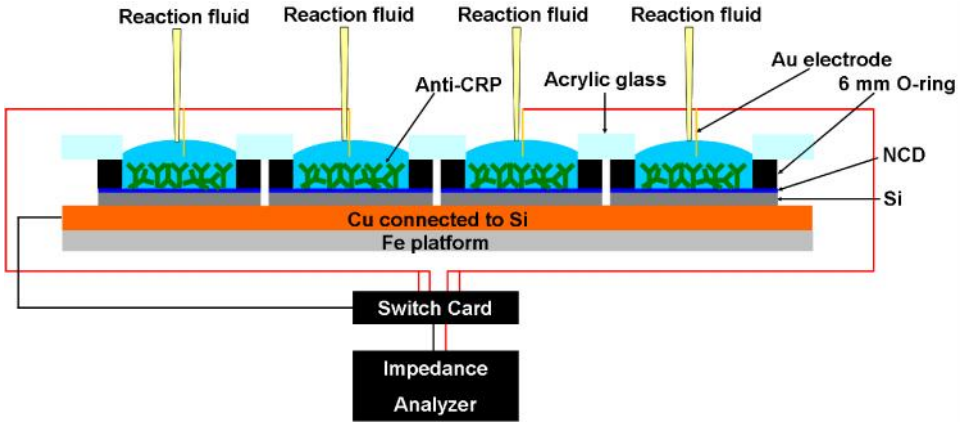

Figure 6.3: Schematic diagram of the immunosensor setup. The sensor houses four anti-CRP-functionalized NCD samples, allowing the simultaneous measurement of four conditions. Adapted from [Bijnens et al., 2009].

Four separate NCD samples of 1cm^2 coated with anti-CRP antibodies, functioning as working electrodes, were mounted on a copper (Cu) back contact using silver (Ag) paste. Rubber O-rings with a diameter of 6mm and an acrylic glass lid containing circular openings of equal size were pressed onto the samples to create four reaction wells above the NCD samples.

Each well was filled with pure (1x or 0.1x) PBS buffer. Au wires, placed ~1mm above each NCD surface and in contact with the reaction fluid, were used as counter-electrodes. Ag/AgCl electrodes were also tested. However, noise was lowest using Au. Working and counter-electrodes were connected to the impedance analyzer with shielded cables. Hence, four signals were recorded simultaneously.

EIS was performed using a Hewlett Packard 4194A Impedance/Gain-Phase Analyzer (Agilent, Diegem, Belgium). The impedance is measured by applying an AC potential (U) of 10mV to the measurement cell. The response to this potential is an AC current signal (I). The complex impedance (Z) was measured for 50 frequencies, equidistant on a logarithmic scale, in a frequency range from 100Hz to 1MHz. The duration of one complete frequency sweep per channel was 8 seconds. A Keithley 7001 switch card (Keithley Instruments, B.V., Sint-Pieters-Leeuw, Belgium) was used to switch between the four channels after each frequency sweep.

Real-time impedance curves from anti-CRP-functionalized or BSA-functionalized NCD samples mounted into the above described setup were recorded continuously during stabilization in buffer before antigen addition, antigen addition, and rinsing. Experiments were performed at 37 °C, by placing the sensor setup inside a humidity-controlled oven, which also provided electromagnetic shielding.

6.4 Detection of CRP in physiological buffer

6.4.1 Specificity of the immunosensor

The specificity of the sensor was investigated by comparing the effect of CRP with that of plasminogen on the impedance behavior of anti-CRP-functionalized NCD samples.

Real-time immunosensing experiments were performed as follows. The wells were first filled with 140 µl of 1× PBS, after which the impedance signal was allowed to stabilize until the difference in between two successive frequency sweeps was negligible throughout the entire frequency range. At the time corresponding to t=0, CRP was added to the first two wells, while plasminogen was added to the third and fourth well, ensuring that all final antigen concentrations were respectively 62.5µg/mL and 40.0µg/mL. After 80 minutes, the four wells were rinsed three times with pure 1× PBS buffer. In order to check for the presence of free antibodies on the NCD surface that were still available for antigen recognition after this procedure, and also to investigate the reliability of the sensing method, the addition of proteins was repeated as before. Figure 6.4 illustrates a typical real-time behavior of the impedance at 100 Hz during such an experiment.

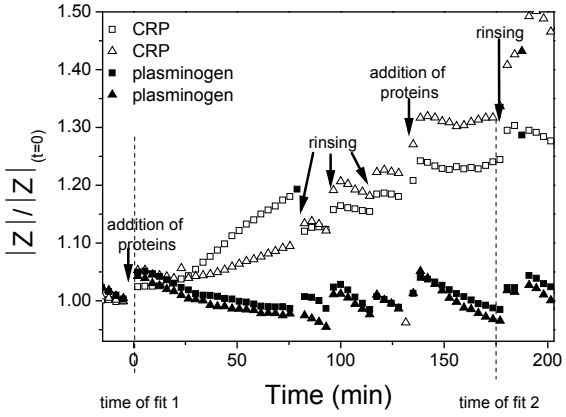

Figure 6.4: Normalized time resolved impedance at 100Hz for the addition of 62.5µg/mL CRP (open symbols) and 40.0µg/mL plasminogen (filled symbols).

Note that the start of the first antigen treatment, immediately after the first antigen addition to the buffer (t=0), can be regarded as an internal reference point, corresponding to a condition where none of the antibodies have recognized their antigen. This allows the events in each channel to be evaluated relative to this point. Hence, the impedance in each channel has been normalized to this internal reference point.

In all of the channels, the direct effect of protein addition is an immediate steep impedance increase of ~5 %. After 80 minutes, the impedance has increased with 20 % in the first well treated with CRP (open squares) and with 10 % in the second well treated with CRP (open triangles), with respect to t=0. A small decrease of ~2 % with respect to $t = 0$ after the initial impedance increase was observed in the wells where plasminogen was added (full symbols).

During the second antigen recognition phase, both CRP channels no longer show the clear increase in impedance after the initial rise as observed during the first protein addition, indicating that most of the anti-CRP antibodies recognized their CRP targets during the first reaction. However, they have now reached an increase of more than 25 % from the reference point t=0, possibly due to extensive ionic redistribution in the molecular layer during the rinsing

steps. The channels where plasminogen was added show the same behavior during both additions.

Figure 6.5 and Figure 6.6 show the Nyquist plots of this experiment at the reference point t=0 (full squares) and at the end of the second protein addition (open squares) of one CRP- and one plasminogen-treated channel, respectively. It is obvious that the impedance at low frequencies has increased during the CRP recognition (Figure 6.5). During plasminogen incubation (Figure 6.66), a completely different behavior is observed. The impedance has decreased over the frequency range from 100Hz to 1000Hz. The results for the remaining channels are similar (data not shown).

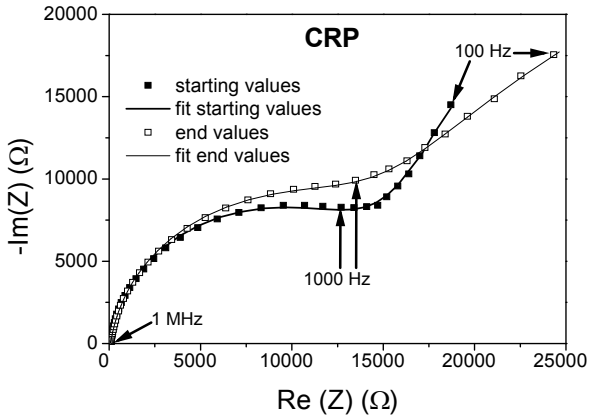

Figure 6.5: Nyquist plots showing the impedance for the 50 frequencies at the start of the first CRP addition (filled symbols) and at the end of the second CRP addition (open symbols). The full lines indicate fits to an equivalent circuit.

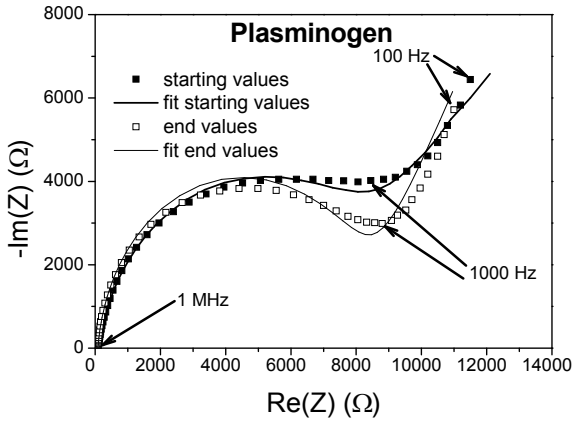

Figure 6.6: Nyquist plots showing the impedance for the 50 frequencies at the start of the first plasminogen addition (filled symbols) and at the end of the second plasminogen addition (open symbols). The full lines indicate fits to an equivalent circuit.

In order to get more insight in the physical meaning of the impedance variations, the Nyquist plots of Figure 6.5 and Figure 6.6 were analyzed using equivalent circuit models. This was done using the ZSimpWin software from Princeton Applied Research (Massachusetts, USA). The fits were performed over the total frequency range from 100Hz to 1MHz. For most of the data, good fits ($\chi^2 \sim 4\times10^{-4}$) could be obtained by using the model circuit given in Figure 6.7, and they are illustrated by the full lines in Figure 6.5 and Figure 6.6.

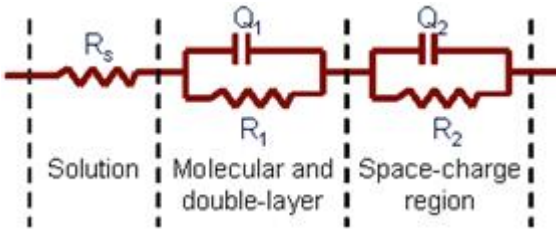

Figure 6.7: The electrical circuit model used for fitting the impedance data.

The circuit can be divided into three components: (a) the solution resistance R_s, between the Au electrode and the NCD surface, (b) a resistance

R_{Q1} and a constant phase element Q_1 in parallel, corresponding to the molecular layer and its associated double-layer on the surface, and (c) a resistance R_{Q2} and a constant phase element Q_2 in parallel, corresponding to the space-charge region in the NCD. The impedance of a Q element, where Q is dependent on i and w, is defined by

$$Z = \left[Q(i\mu)^n\right]^{-1} \qquad \text{(Eq 6.1)}$$

For our data, n varied between 0.7 and 1.0. A value of n=1 is equivalent to a 'perfect' capacitor. A value of n=0.5 corresponds to a Warburg impedance [Grimmes et al., 2000] The parameter values obtained for the fits shown in Figure 6.5 and Figure 6.6 are indicated in Table 6.1.

Table 6.1: Results of fitting the impedance spectra at the start of the first and at the end of the second addition of CRP and plasminogen.

Element	CRP			Plasminogen		
	Start	End	Significant effect (%)	Start	End	Significant effect (%)
R_s (t)	69.7 ± 1.3[a]	66.2 ± 0.8	-5 ± 2	74.1 ± 1.9	81 ± 4	+9 ± 6
Q_1 ($\mu S.s^n$)	0.48 ± 0.05	0.279 ± 0.015	-42 ± 7	1.3 ± 0.3	1.7 ± 0.7	–
n	0.77 ± 0.02	0.78 ± 0.01	–	0.71 ± 0.03	0.69 ± 0.06	–
R_1 (t)	und.[b]	und.	–	und.	und.	–
Q_2 ($nS.s^n$)	12.1 ± 0.9	13 .3 ± 0.7	–	21.2 ± 1.9	6.2 ± 0.9	-70 ± 5
n	0.96 ± 0.01	0.95 ± 0.01	–	0.89 ± 0.01	0.96 ± 0.01	+7 ± 2
R_2 (kt)	1.31 ± 0.04	1.28 ± 0.04	–	7.8 ± 0.4	7.8 ± 0.3	–

Notes:

[a] reported uncertainties are standard deviations as obtained from the data fits

[b] und.: undetermined. Very large uncertainties were obtained for R_1. This can be explained by the fact that R_1 is the value of the real part of the impedance, extrapolated from the very low frequency end of another semi-circle in the Nyquist plot. As can be seen in Fig. 3B and Fig. 3C, only the start of this new semi-circle is visible in the corresponding Nyquist plots, leading to a large uncertainty in the fit results of R_1.

From the fit results it can be seen that the increase of the impedance at low frequencies (100 – 1000Hz) during CRP-treatment in Figure 6.5 corresponds with a significant decrease of the Q_1 value with 42 ± 7 %. This was consistently observed, and indicates a smaller capacity for the molecular layer after CRP recognition at the surface. The additional layer of CRP antigens on top of the anti-CRP antibodies increases the thickness of the molecular layer and changes its dielectric properties, decreasing its capacitance.

However, in the well where plasminogen was added, only the other parallel element R_2Q_2, reflecting the space-charge region of the NCD, shows significant changes. The constant phase element Q_2 decreases with 70 ± 5 %. It should be mentioned that this large decrease of Q_2 was not consistently observed for all plasminogen additions. However, what was observed in each experiment for the reference channel (CRP buffer addition, plasminogen addition, BSA-coated NCD), is a slight decrease of the total impedance at low frequencies, as illustrated in the following paragraph.

6.4.2 Reliability of the immunosensor

In order to get more insight in the reliability of the immunosensor, we performed a variation on the specificity measurements. The effect of antigen addition on NCD:H samples functionalized with anti-CRP was compared with NCD:H coated with BSA. Typical results of such an experiment are illustrated in Figure 6.8, where the normalized impedance at 100 Hz is given during plasminogen treatment of coated and uncoated NCD.

After stabilization, first plasminogen was added to the wells, so that the final concentration in the wells was 40.0µg/mL. The resulting effect is given in Figure 6.8. After the typical initial impedance increase, there was a decrease of ~2 and 6 % with respect to $t = 0$ for both NCD types, comparable to the effect observed in Figure 6.4.

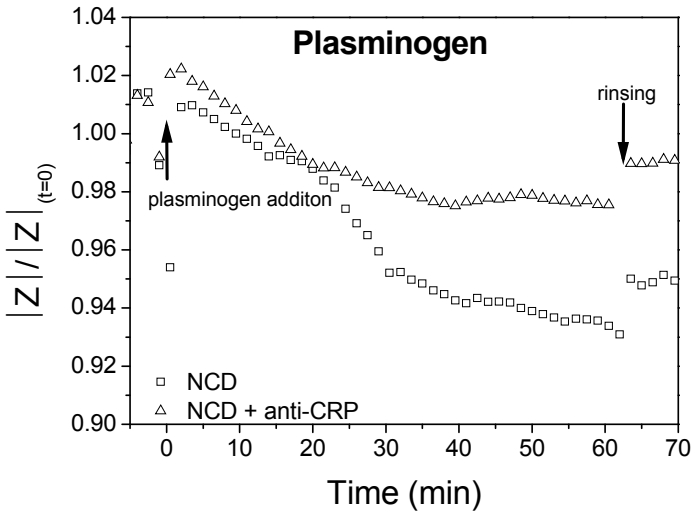

Figure 6.8: Normalized time resolved impedance at 100Hz for the addition of 40µg/mL plasminogen on BSA blocked NCD (□) and NCD functionalized with anti-CRP (a).

In a second step, and after rinsing, CRP was added to these wells in a final concentration of 62.5µg/mL. As can be seen in Figure 6.9, CRP addition has the characteristic increasing effect only on the NCD sample functionalized with anti-CRP (open triangles), associated with a decrease in molecular layer capacitance. The level of this increase, however, is slightly smaller than in Figure 6.4.

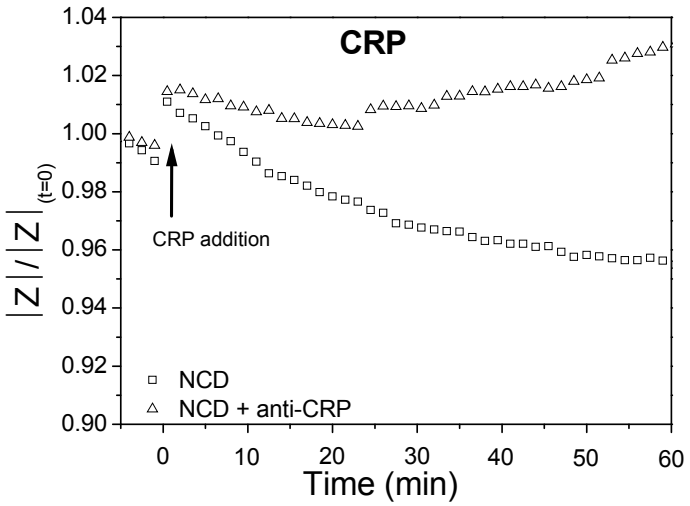

Figure 6.9: Normalized time resolved impedance at 100Hz for the addition of 62.5µg/mL CRP on BSA blocked NCD (□) and NCD functionalized with anti-CRP (a).

6.4.3 Sensitivity of the immunosensor

A clear effect on the impedance is also reproducibly observed in real-time when exposing the anti-CRP-modified NCD:H samples to different concentrations of CRP. Different concentrations of CRP or pure buffer were added to 140µL of 0.1x PBS buffer. The final concentrations of CRP in well 1, 2 and 3 are respectively 12.5µg/mL, 1.25µg/mL and 0µg/mL. The real-time impedance spectra at 100Hz in Figure 6.10 show a typical result of this experiment.

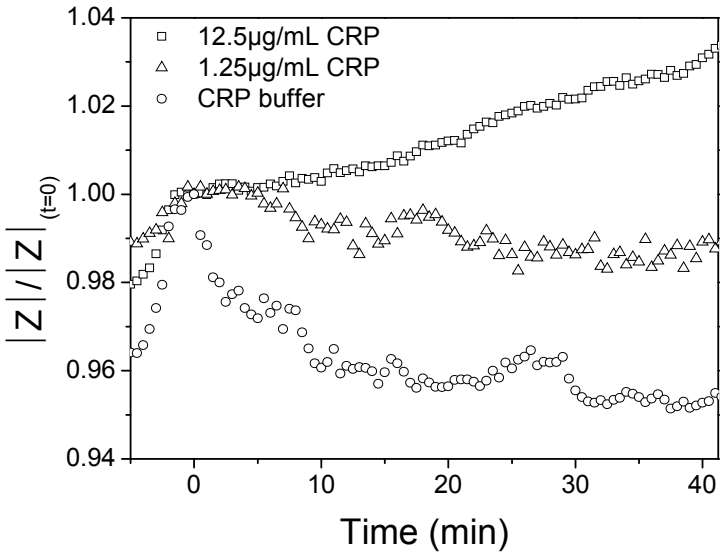

Figure 6.10: Normalized time resolved impedance at 100Hz for the addition of different concentrations of CRP.

The impedance at 100Hz changes in a concentration-dependent manner. The different impedance spectra, corresponding to the different CRP concentrations, can be clearly distinguished from each other within 40 minutes. The impedance of the reference channel (open circles) shows a characteristic decrease, while the impedance of the channel with a CRP concentration of 12.5µg/mL (open squares) is clearly increasing, and shows a comparable behavior to the effect described in Figure 6.4 and Figure 6.9, associated with a decrease in molecular layer capacitance. Like in Figure 6.9, the level of this increase, however, is again smaller than in Figure 6.4. The impedance of the channel with the lowest CRP concentration (open triangles), however, already starts to show a slight decrease, indicating a lower density of antigen/antibody-complexes, and approaching the condition of non-recognition, also seen with buffer and plasminogen treatment. Figure 6.11 shows a calibration for concentrations varying from 0.125 µg /mL to 125µg/mL. The data represent the mean value and standard deviation for the change in Z after 40 minutes of CRP treatment. The mean value and standard deviation for pure CRP buffer are

indicated by the full line and shaded area, respectively. From this curve it is clear that 1.25µg/mL was the lowest concentration that could reproducibly be discriminated from buffer. This limit of detection was comparable to the work described by Hu et al. (2006), who could detect 1µg/mL of purified CRP, and even slightly better than the work described by Meyer et al. (2006), who reached a detection limit of 2 – 5µg/mL of purified CRP. All of these studies were done in real-time, with results of our group and Hu et al. (2006) being obtained in the minute-scale, while an experiment of Meyer et al. (2006) takes about 3 hours. However, further improvements are needed to reach and exceed that of the hs-CRP assay and that of Meyer et al. (2007) in crude samples. However, these are endpoint assays.

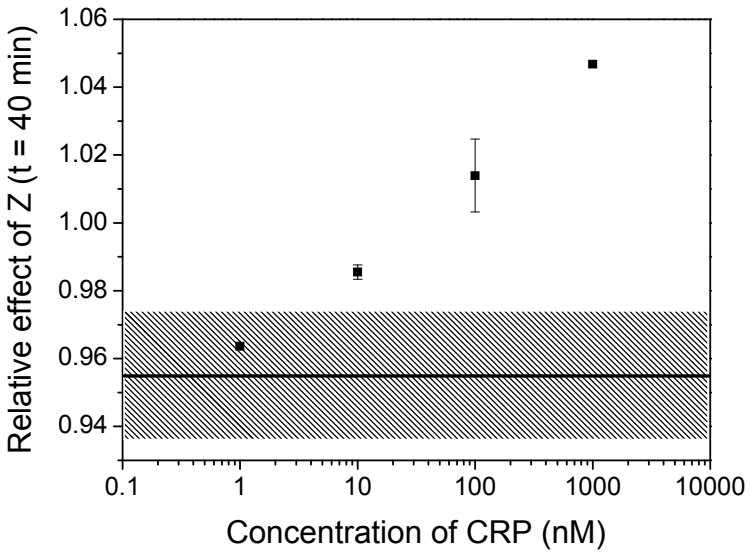

Figure 6.11: Dose response curve of different CRP concentrations. The data are generated from 3 independent measurements, with corresponding standard deviation.

The real-time impedance spectra observed at 100 Hz (Figure 6.4, Figure 6.9 and Figure 6.10) indicate that, when comparing the sample channel to a reference channel in the same measurement, a good discrimination between the two conditions is obtained after 40 minutes of reaction. However, because of the good reproducibility of the sensor, it is also possible to compare the sample

channels of separate measurements. This is illustrated in Figure 6.12, where the CRP-dependent impedance curve (black squares) is the average of 5 independent impedance measurements at 100Hz on anti-CRP-functionalized samples, while the non-specific plasminogen-dependent impedance curve (red squares) is the average of 7 independent impedance measurements at 100 Hz on anti-CRP-functionalized samples. The added concentrations were identical to the previous experiments. The error bars indicate standard deviations. It can be seen that, after 25 minutes, the two types of curves significantly diverge, and obtain a range of values specific for reference and sample. The rise in impedance remains consistently characteristic for the specific CRP recognition.

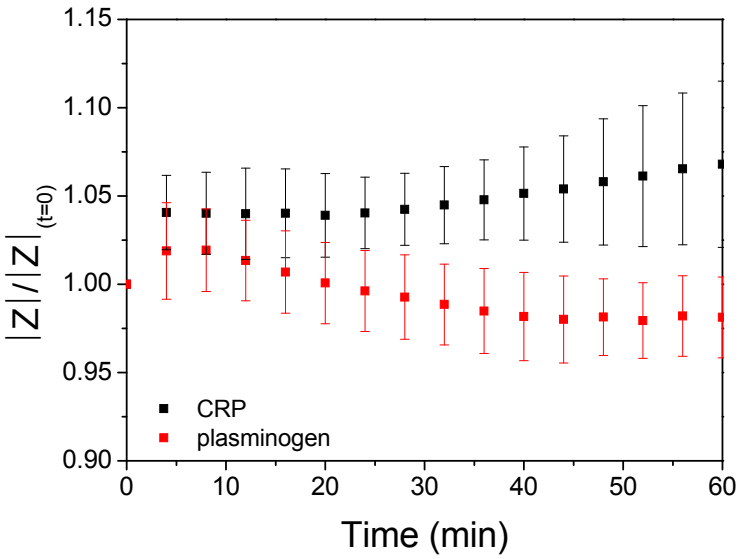

Figure 6.12: Averaged, normalized time resolved impedance at 100Hz during 62.5µg/mL CRP addition (black) and 40.0µg/mL plasminogen addition (red). The data are generated from respectively 5 and 7 independent measurements, with corresponding standard deviations.

6.5 Detection of CRP in serum

To investigate the immunosensor's suitability to detect CRP in a complex and clinically relevant matrix, the reaction wells were first filled with 140µl of pure

human serum. After stabilization of the impedance signal, spiked serum was added so that the final CRP concentration was 62.5µg/mL (t=0). For the negative control, the same volume of unspiked human serum was added. Figure 6.13 shows the average of 6 independent impedance measurements at 100Hz on anti-CRP functionalized samples in human serum.

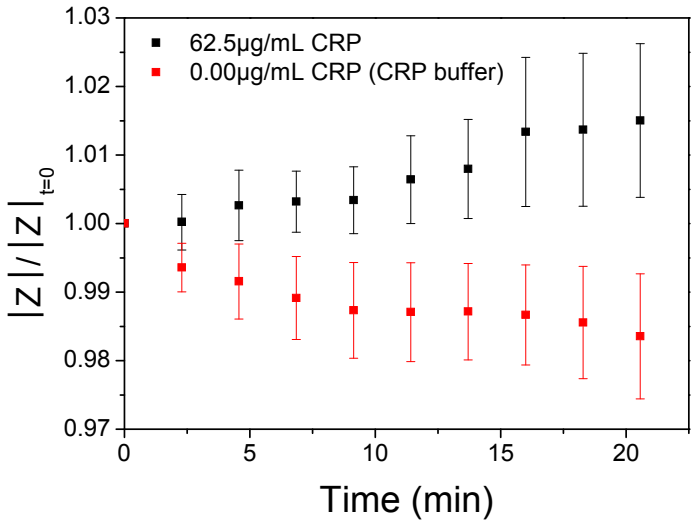

Figure 6.13: Averaged, normalized time resolved impedance at 100Hz during the addition of 62.5µg/mL spiked serum (black) and unspiked serum (red). The data are generated from 6 independent measurements, with corresponding standard deviations.

The negative control shows the typical decrease in impedance signal. The spiked serum causes a characteristic impedance increase of 1.6 % after 30 minutes. As compared to the measurements in buffer, shown in Figure 6.12, the impedance effect is slightly less, probably due to the high complexity of the medium. However, the difference in impedance behaviour between spiked and unspiked serum was significant ($p > 0.045$), indicating that real-time and label-free detection of CRP is possible in human serum.

It should be remarked that, in comparison to our impedimetric experiments on DNA-functionalized NCD samples [Vermeeren et al., 2007], the stabilization of the immunosensor impedance signal after the disturbance of the

system by pipetting manipulations takes longer. This increased stabilization time can be attributed to the fact that the DNA probes were covalently bound to the NCD through fatty acid linker molecules, whereas the antibodies were physically adsorbed to H-terminated NCD. Some degree of gradual dissociation and re-adsorption of the antibodies from and to the surface can therefore not be excluded, resulting in a dynamic molecular layer. It has been reported that covalently attaching the receptor molecules to a surface significantly decreases signal drift as compared to physically adsorbed receptor molecules [Carrara et al., 2008].

6.6 Conclusion

In this work, the potential of EIS on H-terminated NCD is demonstrated for the development of a real-time and label-free immunosensor. The suitability of this diamond substrate for functional antibody adsorption was demonstrated with fluorescence microscopy as reference techniques. In this study a specific discrimination between CRP and plasminogen was obtained with EIS in real-time at low frequencies (100Hz).

Specific CRP recognition by the physisorbed anti-CRP antibodies was consistently associated with an increase in impedance, due to a decreased capacitance of the molecular layer caused by CRP binding. The level of increase varied between 5 and 20 %. On the other hand, non-specific conditions, either by the addition of plasminogen or buffer to anti-CRP-functionalized NCD or the use of BSA-coated NCD, were characterized by a small impedance decrease at 100Hz of ~ 5 %.

The sensitivity of the immunosensor was analyzed by incubating the NCD samples with different concentrations of CRP. At 100 Hz, the lowest concentration of CRP used in our experiments (1.25µg/mL) was still clearly distinguishable from the reference channel treated with buffer within 20 minutes. This indicates the possibility that our prototype immunosensor for CRP can reach a sensitivity within the physiologically relevant concentration range, important to discriminate between healthy controls (1.00 – 1.25µg/mL) and patients at risk for CVD (>1.25µg/mL).

Preliminary serum measurements were also performed, and showed that the impedimetric immunosensor was capable of significantly distinguishing between spiked and unspiked serum. The applicability of the sensor in a real biological matrix displays genuine clinical relevance, and will allow for its use as a point-of-care diagnostic device.

For future experiments, a covalent attachment of blocking molecules and antibody molecules on NCD is recommended to decrease the stabilization time of the impedance signal. Additionaly, to reach physiologically relevant sensitivity in patient serum samples, the CRP detection signal needs to be enhanced, as discussed in Chapter 7.

7

GENERAL DISCUSSION, CONCLUDING REMARKS AND FUTURE PROSPECTIVES

7.1. General discussion

Since the first biosensor in 1962, a lot of different biosensor platforms have been developed for a multitude of applications, but mostly for medical applications. Electrochemical transduction, like EIS, is preferred for clinical diagnostics, because it can be used for the relative cheap, sensitive, label-free and real-time detection of DNA mutations and disease-related proteins. NCD is an attractive transducer material for electrochemical biosensor applications, because it has good electronic and chemical properties. In this work, biosensor platforms based on NCD electrodes were developed for the electrochemical immunological detection of a biomarker related to cardio-vascular diseases and the denaturation-based detection of genetic mutations related to PKU. In this last chapter, the results will be discussed based upon the four major milestones, mentioned in the general introduction.

a. Can an automated DNA-sensor platform be developed to measure the differences in denaturation kinetics in complementary DNA strands and DNA strands containing clinically relevant single base mismatches?

The development of an impedimetric DNA-sensor for the detection of SNPs in synthetic 29-mer PAH exon 9 fragments is described in Chapter 3. SNP detection is based on the difference in the intrinsic stability of complementary and mismatched DNA sequences upon chemically induced denaturation. Continuing on the results of Vermeeren et al. in 2007, a more sophisticated mathematical model was used to describe the impedimetric denaturation kinetics. Denaturation time-constants for complementary and 2 different SNP-containing DNA fragments were calculated using this model. The highest denaturation time was obtained for complementary DNA fragments, the mismatched DNA fragments had lower time-constants. The denaturation times for the 2 different SNP-containing DNA fragments were significally different. However, it is not easy to fine tune chemical denaturation in order to look into minor differences in melting kinetics of different SNPs. For that purpose, thermal denaturation is more appropriate and can be used as alternative for chemically induced denaturation-based SNP detection [Wartell et al., 1998]. Temperature control is possible using the original sensor setup that we described in Chapter 3. However impedance spectroscopy is sensitive to temperature changes. This implicates

that increasing temperatures result in an increase in the impedance as well. This would complicate data analysis even more. However, we observed that thermal denaturation kinetics also has an impact on the R_{th} of biofunctionalized NCD interfaces. The R_{th}-based method was explored and verified with fluorescence- and impedimetric-based SNP detection results in chapter 4.

In Chapter 4, the R_{th}-based technique is used to detect SNPs during thermal denaturation of synthetic 29-mer PAH exon 9 fragments. An increase in R_{th} upon denaturation of dsDNA was observed. This change in R_{th} is probably caused by a conformational change of the immobilized DNA fragments upon denaturation. The immobilized dsDNA fragments, used in chapter 4, are upright, rigid structures [Wenmackers et al., 2009] allowing easily heat-transfer between the stiff dsDNA structures. After denaturation, the resulting ssDNA fragments flatten out and the level of coverage on the NCD surface will increase. As a result the heat-transfer from the NCD surface to the buffer solution will be decreased by the coiled ssDNA fragments and the R_{th} will increase. It looks that this finding is opposite in comparison with the theoretical work of Velizhanin et al. (2011), however they tested the heat-transfer in ssDNA fragments instead of the heat-transfer in between immobilized DNA fragments [Velizhanin et al., 2011].

The temperature at which the change in R_{th} upon denaturation was observed, reflects the melting temperatures of the complementary and SNP-containing dsDNA fragments. As expected, the highest T_m was obtained for the complementary DNA fragments, while the mismatched DNA fragments had lower T_ms. The relative order of T_ms obtained with the R_{th}-based method correlate well with the relative order of T_ms calculated with the online HyTher™ algorithm [http://ozon3.chem.wayne.edu/]. The exact R_{th}-based T_ms are lower than the calculated values, however, these values are reproducibly obtained even with different NCD samples. This label-free technique is a promising, inexpensive, fast, and real-time alternative to the currently used denaturation-based techniques for the detection of point mutations, like DGGE. Indeed, the R_{th}-based DNA-sensor setup was used to detect common PKU related SNPs during thermal denaturation, but only in small synthetic 29-mer fragments. However, in order to translate this R_{th}-based method into a simplified multiplexed assay for

routine genetic analysis, it needs to be extended to exon-size SNP analysis in patient-derived DNA fragments. This issue was tackled in Chapter 5.

b. Can this prototype be used to identify clinically relevant point mutations in patient-derived, exon-size DNA fragments?

Chapter 5 describes the evaluation of the R_{th}-based SNP detection method with the use of both synthetic and patient-derived exon-length PAH DNA fragments. First, the maximum length of DNA fragments was determined, where a R_{th} change upon denaturation of exon-size DNA fragments could still be observed. A clear R_{th} shift was observed upon denaturation of complementary DNA-fragments up to 123 bp. No R_{th} change was observed when using complementary dsDNA fragments of 150 bp. A feasible explanation is that dsDNA fragments of 150 bp exceed the persisting length a do curve to the NCD surface, therefore reducing the heat-transfer through the spaces in between the immobilized dsDNA fragments. This will result in a reduced resolution or disappearance of the differences between the R_{th} values for ssDNA and dsDNA fragments. Additionaly, the sensitivity of the R_{th}-based method for SNPs in synthetic versions of the PAH exons was evaluated. Using exon-length synthetic DNA fragments, it was possible to detect 3 of the most common SNPs in the PAH gene associated with PKU, based on their difference in T_m. The T_m of the SNP-containing dsDNA fragments is decreased compared to the T_m of the complementary dsDNA fragments. This is due to the fact that dsDNA fragments containing a SNP are less stable than homoduplex dsDNA fragments. As proof-of-application, the detection of the most common SNP, c.1222C>T (R408W), was demonstrated using PKU patient blood-derived, PCR-amplified DNA of exon 12. Finally, a uniform procedure to calculate R_{th}-based T_ms is proposed. This method can replace the estimation-based method to obtain R_{th}-based T_ms, as described in chapter 4. The proposed procedure is based on fitting the real-time, normalized R_{th} curves with the sigmoidal Boltzmann function (equation 5.2). The parameters in this equation describe the absolute R_{th} change upon denaturation and the corresponding T_m in a standardized approach. The results in this chapter indicate that R_{th} can be used to detect homozygous mutations in exon-length DNA fragments of PKU patients. The R_{th}-based detection of heterozygous mutations in exon-length DNA fragments of PKU carriers will be discussed in

Section 7.2. The R_{th}-based sensor, described in Chapter 4 and 5, offers the advantages of showing real-time SNP-sensitivity in exon-length PCR-fragments as compared to the DNA-sensors developed by Lapierre et al. (2003) and Davis et al. (2007). Lapierre et al. constructed a biosensor for the detection of PCR-amplified DNA fragments and a medical significant SNP. However this biosensor needs the use of a redox mediator for significantly amplifying the response and moreover no real-time impedimetric information was provided [Lapierre et al., 2003]. Davis et al. developed an impedimetric DNA hybridization sensor for differentiating between different ssPCR fragments. This sensor showed a sensitive response to complementary ssDNA targets in a concentration range from 1 fg/mL to 1 ng/mL. However no SNP-sensitivity was obtained [Davis et al., 2007].

c. Can an electrochemical immunosensor platform be developed to selectively detect a clinically relevant target molecule? And is it possible to detect it in a physiologically appropriate concentration range?

Chapter 6 discusses on the one hand the functionalization of H-terminated NCD with anti-CRP antibodies and, on the other hand, the impedimetric detection of CRP in buffer solutions and in serum samples.

The functionality of anti-CRP antibodies adsorbed on H-terminated NCD surfaces was evaluated using a traditional reference method, an ELISA. CRP detection was indirectly studied by the incubation with AP-labeled anti-CRP antibodies and the corresponding colour formation. The H-terminated NCD sample modified with anti-CRP antibodies could successfully detect 0.3mg/mL CRP. Hence, this result indicates that modification of H-terminated NCD with antibodies through physisorption is possible. Grieten et al. investigated the influence of several surface chemistries on the adsorption efficiency of antibodies. They postulated that oxidized NCD surfaces allowed more rapid adsorption of antibodies, because it is a more hydrophilic surface then H-terminated NCD. On both surfaces the antibodies maintained their biological activity, but the largest impedimetric response was obtained with H-terminated NCD [Grieten et al., 2011].

In a next step, the impedimetric detection of CRP on H-terminated NCD surfaces functionalized with anti-CRP antibodies was evaluated. First, the

specificity of the anti-CRP immunosensor was investigated. The impedance signal increased after 10 minutes of incubation with 62.5µg/mL CRP, due to an increased thickness of the molecular layer, causing a significant decrease in the molecular layer capacitance. A decrease in the impedance signal is observed upon incubation with 40.0µg/mL plasminogen. These results indicate that the immunosensor can differentiate between the specific target and a negative control protein. Secondly, the sensitivity of the immunosensor in physiological buffer was investigated. The lowest concentration that could be reproducible discriminated from buffer was 1.25µg/mL within 20 minutes. This limit of detection was comparable to the work described by Hu et al. in 2006, who could detect 1µg/mL of purified CRP, and even slightly better than the work described by Meyer et al. in 2006, who reached a detection limit of 2 – 5µg/mL of purified CRP [Hu et al., 2006; Meyer et al., 2006]. The impedimetric biosensor developed by Quershi et al. in 2009 has a better detection limit, in the 0.125µg/mL range, but this sensor has an endpoint character and CRP detection is obtained in the hour range instead [Quershi et al., 2009] of in the minute-scale as with our sensor and the sensor developed by Hu et al. in 2006. This result shows that our prototype CRP sensor reaches a sensitivity within physiologically relevant concentration ranges in buffer solutions.

d. Can this prototype also be used to measure the target molecule in a clinically relevant concentration range in patient-derived serum samples?

It is very important that the prototype of the immunosensor is able to discriminate between healthy controls (1.00-1.25µg/mL) and patients at risk for CVD (>1.25µg/mL) in serum samples. Therefore, preliminary serum measurements were performed in Chapter 6. The impedimetric immunosensor was capable of significantly distinguishing between unspiked serum and serum spiked with 62.5µg/mL CRP. However, the increase in impedance signal was lower as compared to the impedance increment upon detection of the same CRP concentration in buffer. This less pronounced effect is probably due to high concentrations of non-specific proteins present in samples. Up till now it is not yet possible to discriminate lower CRP concentrations in undiluted serum samples. Further improvements are needed to reach clinically relevant detection limits in CVD patient samples, to be able to compete with the hs-CRP ELISA-

based assay, the SPR-based assay of Meyer et al. [Meyer et al. 2007] and the impedimetric-based sensor developed by Kunduru et al. [Kunduru et al., 2010]. Possible improvements are described in Section 7.2.

7.2. Concluding remarks and future prospectives

In this dissertation two different label-free, real-time electrochemical DNA-sensors were developed. The first sensor is based on changes in impedimetric behavior upon chemical denaturation of DNA. The impedimetric DNA-sensor was able to detect PKU related SNPs in a 29-mer synthetic, exon 9 fragment of the PAH gene within minutes. Murib et al. suggests that detection times can be decreased by increasing the pump flow rate or the concentration of NaOH [Murib et al., 2013]. However, in general it is not easy to fine tune chemical denaturation to identify mismatches that have comparable melting temperatures. Therefore, thermal denaturation is a good alternative for chemically induced denaturation-based SNP detection. Because impedance spectroscopy is sensitive to temperature changes, a second DNA-sensor was developed based on changes in heat-transfer resistance upon thermal denaturation of DNA. This sensor was able to detect homozygous mutations in PCR-amplified, exon-length DNA fragments of PKU patients. In the future, the R_{th}-based detection of heterozygous mutations in exon-length DNA fragments is recommended for the detection of PKU carriers. Therefore, the NCD will be functionalized with all wildtype and mutant variants of the PAH exons in pre-designated and isolated areas on the surface. In a next step, all exon probes will be hybridized under highly stringent conditions with exon-length target DNA fragments from possible PKU carriers. The thermal denaturation will likely result in a bipartite R_{th} change [Bers et al., 2013], reflecting the denaturation of the different types of dsDNA fragments present on the NCD surface. Thus, for the detection of heterozygous mutations, the sensor needs to be converted to an array-based system. A first step towards an array-based format would be the miniaturization of the NCD sensor electrodes. Possible fabrication processes of array-based NCD electrodes are reported by Bonnauron et al. and Yang et al. [Bonnauron et al, 2008; Yang et al., 2008]. A second step is the development of an array-type R_{th}-based detection system. An array of planar thermocouples, with a contact area comparable to the size of the sensor spots, can be realized

through indium tin oxide (ITO) meander structures [Pérez-Ruiz et al., in preparation]. Furthermore, the R_{th}-based method requires PCR-amplification of the desired exon out of patient material. For the automation of the complete process, the PCR process can be implemented into the same sensor setup as the SNP detection, to construct a POC system.

In this dissertation also a label-free, real-time, impedimetric immunosensor was developed. The immunosensor was able to detect physiologically relevant CRP concentrations in buffer solutions. Furthermore, this sensor was capable of detecting high CRP levels in serum samples, indicative of an infection. However, the signal to noise ratio needs to be improved to reach clinically relevant detection limits in CVD patient samples. There are several possible ways to increase the impedance signal intensity or to reduce noise levels. One way is the depletion of major blood proteins, like human serum albumin and immunoglobin G, to increase the CRP concentration [Kuhn et al., 2004]. However, serum depletion will not only remove non-specific serum proteins, but can also remove the target protein [Roche et al., 2009; Bellei et al. 2010]. Alternatively, CRP can be isolated from serum samples by using magnetic nanoparticles [Jarrige et al., 2011]. Ideally, the CRP isolation and CRP detection should be integrated into one sensor setup. This lab-on-a-chip should consist of a preconcentration unit capturing the target molecule from blood samples and, through microfluidics, this captured target will be brought to the sensing unit [Stern et al., 2010]. Alternatively, if CRP is detected in serum samples, the non-specific interaction of serum proteins on the NCD surface needs to be avoided. In this study, the NCD surface was blocked by the adsorption of BSA molecules. However, adsorption of molecules to NCD surfaces causes drift in the impedance signal. For that reason, a covalent attachment method for both blocking molecules and detection antibodies is recommended. A possible attachment procedure is the EDC-based method, also used to attach ssDNA molecules to COOH-terminated NCD surfaces. However, the necessary aminogroups, needed for EDC-based attachment, are located in both the Fc and the Fab regions of the used antibodies, so the orientation of the covalently attached antibodies will not be optimal. However, preliminary results, with a covalently immobilized biolayer on NCD samples, demonstrate that the time to reach a stable impedance signal was reduced when using a covalently immobilized blocker and recopter layer

(data not shown). Secondly, the impedance response can be enhanced by increasing the amount of immobilized antibodies on the sensor electrode. The electrode surface can be increased by using nanostructured surfaces instead of plain electrodes [Kunduru et al., 2010; Rezaei et al. 2011]. Additionally, it is interesting to analyse frequencies below 100 Hz, because they are more sensitive to events in the molecular layer, which will increase the magnitude of the impedance effects during recognition of CRP. A disadvantage is that lower frequencies display more noisy impedance graphs. Another point of improvement is the miniaturization of the sensor setup. This could result in a decrease of the reaction time due to a decrease in diffusion time of the target molecules to the surface. Furthermore, the sensor should be converted to an array-based setup for multi-analyte detection. Detection of a panel of biomarkers, like CRP, TNF-a and IL6, could enable a more accurate prediction of CVD risk, than the detection of CRP alone [Qureshi et al., 2010].

In this dissertation, an universal biosensor platform, based on NCD electrodes for the electrochemical immunological detection of protein biomarkers and the denaturation-based detection of genetic mutations, was evaluated in terms of clinical relevance. The outcome is: that the impedimetric immunosensor is capable of detecting infection-related CRP concentrations in serum samples and in the future, it should be possible to use this impedimetric sensor for the prediction of CVD, when some of the improvements, mentioned in this section, are implemented. Additionaly, the R_{th}-based DNA-sensor is at the moment able to detect PKU patients and in the future it should be possible to detect PKU carriers as well.

References

Altintas Z. and Tothill IE. DNA-based biosensor platforms for the detection of TP53 mutation. Sensors and Actuators B. 2012, 169:188-194

Ambia-Garrido J., Vainrub A., Pettitt P.M. A model for structure and thermodynamics of ssDNA and dsDNA near a surface: a coarse grained approach. Comput. Phys. Commun.

Application note: Basics of electrochemical impedance spectroscopy. Gamry instruments

Ariksoysal D.O., Karadeniz H., Erdem A., Sengonul A., Sayiner A.A., Ozsoz M. Label-free electrochemical hybridization genosensor for the detection of hepatitis B virus genotype on the development of Lamivudine resistance. Anal Chem. 2005, 77(15): 4908-4917

Baccar Z., Caballero D., Eritja R., Errachid A. Development of an impedimetric DNA-biosensor based on layered double hydroxide for the detection of long ssDNA sequences. Electrochimica Acta 2012, 74:123-129

Bangar M., Shirale D., Chen W., Myung N., Mulchandani A. Single Conducting Polymer Nanowire Chemiresistive Label-Free Immunosensor for Cancer Biomarker. Anal. Chem. 2009, 81:2166-2175

Bart M., Stigter E., Stapert H., de Jong G., van Bennekom W. On the response of a label-free interferon-g immunosensor utilizing electrochemical impedance spectroscopy. Biosens Bioelectron. 2005, 21:49-59

Baur J., Gondran C., Holzinger M., Defrancq E., Perrot H., Cosnier S. Label-Free Femtomolar Detection of Target DNA by Impedimetric DNA Sensor Based on Poly(pyrrole-nitrilotriacetic acid) Film. Anal. Chem. 2010, 82:1066-1072

Bellei E., Bergamini S., Monari E., Fantoni L., Cuoghi A., Ozben T., et al. High-abundance proteins depletion for serum proteomic analysis: concomitant removal of non-targeted proteins. Amino Acids. 2010, 40:145-146

Belluzo M., Ribone M., Camussone C., Marcipar I., Lagier C. Favorably orienting recombinant proteins to develop amperometric biosensors to diagnose Chagas' disease. Anal. Biochem. 2011, 408:86-94

Bers K., van Grinsven B., Vandenryt T., Murib M., Janssen W, Geerets B. et al. Implementing heat-transfer resistivity as a key element in a nanocrystalline diamond based single nucleotide polymorphism detection array. Diamond & Related Materials. 2013, 38: 45-51

Bianchi N., Rutigliano C., Tomassetti M., Feriotto G., Zorzato F., Gambari R. Biosensor technology and surface plasmon resonance for real-time detection of HIV-1 genomic sequences amplified by polymerase chain reaction. Clin Diagn Virol. 1997, 8(3): 199–208.

Bickel H., Gerrard J.W., Hickmans E.M. Influence of phenylalanine intake on phenylketonuria. Lancet. 1953, 265(6790):812–813.

Bijnens N., Vermeeren V., Daenen M., Grieten L., Haenen K., Wenmackers S. Synthetic diamond films as a platform material for label-free protein sensors, Phys. Stat. Sol. a. 2009, 206: 520-526

Blau N., van Spronsen F.J., Levy HL. Phenylketonuria. Lancet. 2010, 376(9750): 1417–1427.

Bonnauron M., Saada S., Mer C., Gesset C., Williams O.A., Rousseau L., et al. Transparent diamond-on-glass micro-electrode arrays for ex-vivo neuronal study. Phys. Status Solidi A. 2008, 205: 2126 – 2129

Booth M., Harbison S., Travas-Sejdic J. Development of an electrochemical polypyrrole-based DNA sensor and subsequent studies on the effects of probe and target length on performance. Biosens Bioelectron 2011, 28:362-367

Bourigua S., Hnaien M., Bessueille F., Lagarde F., Dzyadevych S., Maaref A. et al. Impedimetric immunosensor based on SWCNT-COOH modified gold microelectrodes for label-free detection of deep venous thrombosis biomarker. Biosens. Bioelectron. 2010, 26:1278-1282

Brianina K., Kozitsina A., Belkin J. Electrochemical immunosensor for Forest-Spring encephalitis based on protein A labeled with colloidal gold. Anal Bioanal Chem. 2003, 376:481-485

Buchan B., Peterson J., Cogbill C., Anderson D., Ledford J., White M., et al. Evaluation of a Microarray-Based Genotyping Assay for the Rapid Detection of Cytochrome P450 2C19 *2 and *3 Polymorphisms From Whole Blood Using Nanoparticle Probes. Am J Clin Pathol 2011, 136:604-608

Cabellero D., Martinez E., Baussels J., Errachid A., Samitier J. et al. Impedimetric immunosensor for human serum albumin detection on a direct aldehyde-functionalized silicon nitride surface. Anal Chim Acta. 2012, 720:43-48

Carrara S., Bhalla V.K., Stagni C., Benini L., Riccò, Samorì B. Improving probe immobilization for label-free capacitive detection of DNA hybridization on microfabricated gold electrode. Sensors and Transducers. 2008, 88: 31-39.

Chen B., Zhou X., Li C., Wanga Q., Liua D., Lin B. Rapid screening of phenylketonuria using a CD microfluidic device. J Chromatogr A. 2011, 1218(14): 1907-1912

Chetcuti A., Wong D. An Indirect Perfluorosulfonated Ionomer-Coated Electrochemical Immunosensor for the Detection of the Protein Human Chorionic Gonadotrophin. Anal. Chem. 1999, 71:4088-4094

Christenson R., Azzazy H. Cardiac point of care testing: A focused review of current National Academy of Clinical Biochemistry guidelines and measurement platforms. Clin. Biochem. 2009, 42:150-157

Christiaens P., Vermeeren V., Wenmackers S., Daenen M., Haenen K., Nesladek M., et al., EDC-mediated DNA attachment to nanocrystalline CVD diamond films. Biosens Bioelectron 2006, 22:170-177

Chua J., Chee R., Agarwai A., Wong S., Zhang G. Label-Free Electrical Detection of Cardiac Biomarker with Complementary Metal-Oxide Semiconductor-Compatible Silicon Nanowire Sensor Arrays. Anal. Chem. 2009, 81:6266-6271

Clark L.C., Lyons C. Electrode systems for continuous monitoring in cardiovascular surgery. Ann. N. Y. Acad. Sci. 1962, 102: 29-45

Clukers T., van Grinsven B., Vandenryt T., Janssens S., Wagner P., De Ceuninck W. Boron doped nanocrystalline diamond temperature regulator for sensing applications. Phys. Status Solidi A. 2010, 207:2110-2113

Cohen H., Nogues C., Naaman R., Porath D. Direct measurement of electrical transport through single DNA molecules of complex sequence. Proc. Natl. Acad. Sci. USA. 2005, 102: 11589 – 11593

Cooper M. A., Dultsev F. N., Minson T., Ostanin V. P., Abell C., Klenerman D. Direct and sensitive detection of a human virus by rupture event scanning. Nat Biotechnol. 2001, 19: 833– 837.

Cooreman P., Thoelen R., Manca J., vandeVen M., Vermeeren V., Michiels L., et al. Impedimetric immunosensors based on the conjugated polymer PPV. Biosens. Bioelectron. 2005, 20: 2151-2156

Cullen D., Sethi R., Lowe C. A multi-analyte miniature conductance biosensor. Anal. Chim. Acta. 1990, 231:33-40

Cuniberti G., Craco L., Porath D., Dekker C. Backbone-induced semiconducting behavior in short DNA wire. Phys. Rev. B. 2002, 65

Davis F., Hughes M.A., Cossins A.R., Higson S.P. Single gene differentiation by DNA-modified carbon electrodesusing an AC impedimetric approach. Anal. Chem. 2007, 79: 1153 – 1157

Dekker C., Ratner M. Electronic properties of DNA. Phys. World. 2001, 14: 29 – 33.

Demers L.M., Ginger D.S., Park S.J., Li Z., Chung S.W., Mirkin C.A. Direct patterning of modified oligonucleotides on metals and insulators by dip-pen nanolithography. Science. 2002, 296: 1836 – 1838

Desai A.N., Jere A. Next-generation sequencing: ready for the clinics? Clin Genet. 2012, 81(6): 503-510

DiLella A.G., Kwok S.C.M., Ledley F.D., Marvit J., Woo S.L.C. Molecular structure and polymorphic map of the human phenylalanine hydroxylase gene. Biochemistry. 1986, 25(4): 743-749

Dunning A.M., Healey C.S., Pharoah P.D., Teare M.D., Ponder P.A., Easton D.F., CEBP. 1999, 8: 843 – 854

Eckfeldt J., Levine A., Greiner C., Kershaw M. Urinary urea: Are currently available methods adequate for revival of an almost abandoned test? Clin. Chem. 1982, 28:1500-1502

Eersels K., van Grinsven B., Ethirajan A., Timmermans S., Jiménez Monroy K.L., Bogie J.F.G., et al., Selective Identification of Macrophages and Cancer Cells Based on Thermal Transport through Surface-Imprinted Polymer Layers. ACS Appl. Mater. Interfaces. 2013, 5: 7258−7267

Elshavey R., Tlili C., Abulrob A., Tavares A., Zourob M. Label-free impedimetric immunosensor for ultrasensitive detection of cancer marker Murine double minute 2 in brain tissue. Biosens Bioelectron 2013, 39:220-225

Fang A., Ng H. T., Li S. F. A high performance glucose biosensor based on monomolecular layer of glucose oxidase covently immobilized on indium-tin oxide surface. Biosens. Bioelectron. 2003, 19: 43-49

Farjami E., Clima L., Gothelf K., Ferapontova E.E. “Off-On” electrochemical hairpin-DNA-based genosensor for cancer diagnostics. Anal Chem. 2011, 83(5): 1594–1602

Field J.E. Mechanical and physical properties of diamond. Inst. Phys. Conf. Ser. 1987, 75: 181-205

Fodde R., Losekoot M. Mutation detection by denaturing gradient gel electrophoresis. Human Mutation. 1994, 3: 83 – 94

Gasparac R., Taft B., Lapierre-Devlin M., Lazareck A., Xu J., Kelley S. Ultrasensitive electrocatalytic DNA-detection at two- and three-dimensional nanoelectrodes. J. Am. Chem. Soc. 2004, 126:12270-12271

Gaylord B. S., Heeger A. J., Bazan G. C., DNA detection using water-soluble conjugated polymers and peptide nucleic acid probes. Proc. Natl. Acad. Sci. U.S.A. 2002, 99 (17):10954–10957.

Geerets B., Peeters M., van Grinsven B., Bers K., de Ceuninck W., Wagner P. Optimizing the thermal read-out technique for MIP-based biomimetic sensors: towards nanomolar detection limits. Sensors (Basel). 2013, 13(7): 9148-9159

Gholivand M., Khodadadian M. Amperometric cholesterol biosensor based on the direct electrochemistry of cholesterol oxidase and catalase on a graphene/ionic liquid-modified glassycarbon electrode. Biosens. Bioelectron. 2014, 53:472-478

Gracio J., Fan Q., Madaleno J. Diamond growth by chemical vapour deposition. J Phys D: Appl Phys 2010, 43:374017-374039

Grieten L., Janssens S.D., Ethirajan A., Vanden Bon N., Ameloot M., Michiels L., et al. Real-time study of protein adsorption on thin nanocrystalline diamond. Phys Status Solidi A. 2011, 208:2093-2098

Grimnes S., Martinsen O.S. Bioimpedance & Bioelectricity - Basics. Academic Press, London, 2000

Gruenwedel D.W. Salt effects on the denaturation of DNA. Biochim. Biophys.Acta. 1974, 340: 16 – 30

Guldberg P., Henriksen K.F., Güttler F. Molecular analysis of phenylketonuria in Denmark: 99 % of the mutations detected by denaturing gel electrophoresis. Genomics. 1993, 17(1): 141–146

Guldberg P., Rey F., Zschocke J., Romano V, Francois B., Michiels L. A European multicenter study of phenylalanine hydroxylase deficiency: classification of 105

mutations and a general system for genotype-based prediction of metabolic phenotype. American Journal of Human Genetics. 1998, 63: 71 – 79

Guo X.F., Gorodetsky A.A., Hone J., Barton J.K., Nuckolls C. Conductivity of a single DNA duplex bridging a carbon nanotube gap.

Guthrie R., Susi A. A simple phenylalanine method for detecting phenylketonuria in large populations of newborn infants. Pediatrics. 1963, 32: 338-343

Haenen K., Lazea A., Barjon J., D'Haen J., Habka N., Teraji T., et al. P-doped diamond grown on (110)-textured microcrystalline diamond: growth, characterization and devices. Journal of Physics-Condensed Matter. 2009, 21

Hahm J., Lieber C. Direct ultrasensitive electrical detection of DNA and DNA sequence variation using nanowire nanosensors. Nano Letters. 2004, 4:51-54

Härtl A., Schmich E., Garrido J.A., Hernando J., Catharino S.C.R, Walter, P. Protein-modified nanocrystalline diamond thin films for biosensor applications. Nat. Mater. 2004, 3: 736-742

Haverkate F., Thompson S.G., Pyke S.D., Gallimore J.R., Pepys M.B., Production of C-reactive protein and risk of coronary events in stable and unstable angina. European Concerted Action on Thrombosis and Disabilities Angina Pectoris Study Group. Lancet. 1997, 349: 462-466

Hokama Y. and Nakamura R.M. C-reactive protein: Current status and future perspectives. J. Clin. Lab. Anal. 1987, 1: 15-27

Hooper J.W. The genetic map to theranostics. Medical Laboratory Observer. 2006, 38: 22 – 35

Hooyberghs J., Baiesi M., Ferrantini A., Carlon E. Breakdown of thermodynamic equilibrium for DNA hybridization in microarrays. Phys. Rev. E. 2010: 81

Hooyberghs J., Carlon E. Hybridisation thermodynamic parameters allow accurate detection of point mutations with DNA microarrays. Biosens. Bioelectron. 2010, 26: 1692 – 1695

Hou L., Gao Z., Xu M., Cao X., Wu X., Chen G., Tang D. DNAzyme-functionalized gold–palladium hybrid nanostructures for triple signal amplification of impedimetric immunosensor. Biosens Bioelectron 2014, 54:365-371

Hu W.P., Hsu H.Y., Chiou A., Tseng K.Y., Lin H.Y., Chang G.L., et al. Immunodetection of pentamer and modified C-reactive protein using surface plasmon resonance biosensing. Biosens. Bioelectron. 2006, 21: 1631-1637

Ingebrandt S., Han Y., Nakamura F., Poghossian A., Schöning M.J., Offenhäusser A. Label-free detection of single nucleotid polymorphisms utilizing the differential transfer function of field-effect transistor device. Biosens. Bioelectron. 2007, 22: 2834 – 2840

Ionescu R.E., Jaffrezic-Renault N., Bouffier L., Gondran C., Cosnier S., Pinacho D.G., et al. Impedimetric immunosensor for the specific label free detection of ciprofloxacin antibiotic. Biosens. Bioelectron. 2007, 23: 549-555.

Janssens S.D., Pobedinskas P., Vacik J., Petráková V., Ruttens B., D'Haen J., et al. Separation of intra- and intergranular magnetotransport properties in nanocrystalline diamond films on the metallic side of the metal–insulator transition. New J. Phys. 2011, 8

Jarrige V., Nieuwenhuis J., van Son J., Martens M, Vissers J. A fast intraoperative PTH point-of-care assay on the Philips handheld magnotech system. 2011, 396:337-343

Katz E. and Willner I., Probing Biomolecular Interactions at Conductive and Semiconductive Surfaces by Impedance Spectroscopy: Routes to Impedimetric Immunosensors, DNA-Sensors, and Enzyme Biosensors. Electroanalysis. 2003, 15: 913 – 947

Kawarada H., Ruslinda A.R. Diamond electrolyte solution gate FETs for DNA and protein sensors using DNA/RNA aptamers. Phys. Status Solidi A. 2011, 208: 2005 – 2016

Key G., Schreiber A., Feldbrügge R., McNeil C., Jorgensen P., Pelsers M. et al. Multicenter Evaluation of an Amperometric Immunosensor for Plasma Fatty Acid-Binding Protein:An Early Marker for Acute Myocardial Infarction. Clin. Biochem. 1999, 32:229-231

Kick A., Boensch M., Katzschner N., Voigt J., Herr A., Brabetz W., et al. DNA microarrays for hybridization detection by surface plasmon resonance spectroscopy. Biosens. Bioelectron. 2010, 26: 1543 – 1547

Knez K., Janssen K., Spasic D., Declerck P., Vanysacker L., Denis C. et al. Spherical nucleic acid enhanced FO-SPR DNA melting for detection of mutations in Legionella pneumophila. Anal Chem. 2013, 85(3): 1734-1742

Kodama T., Jain A., Goodson K.E. Heat conduction through a DNA-gold composite. Nano Lett. 2009, 9: 2005 – 2009

Koh W., Choe E., Lee D., Chang S., Shim Y. Monitoring the activation of neuronal nitric oxide synthase in brain tissue and cells with a potentiometric immunosensor. Biosens. Bioelectron. 2009, 25:211-217

Kuhn E., Wu J., Karl J., Liao H., Zolg W., Guild B., Quantification of C-reactive protein in the serum of patients with rheumatoid arthritis using multiple reaction monitoring mass spectrometry and 13C-labeled peptide standards. Proteomics 2004, 4:1175-1186

Kunduru V., Bothara M., Grosch J., Sengupta S., Patra P., Prasad S. Nanostructured surfaces for enhanced protein detection toward clinical diagnostics. Nanomedicine 2010, 6:642-50

Kwok P. Methods for genotyping single nucleotide polymorphisms. Annual Review of Genomics and Human Genetics. 2001, 2:235 - 258

Lakard B., Magnin D., Deschaume O. Vanlacker G., Glinel K., Demoustier-Champagne S. et al. Urea potentiometric enzymatic biosensor base don chargerd biopolymers and electrodeposited polyaniline. Biosens. Bioelectron. 2011, 26: 4139-4145

Lapierre M., O'Keefe M., Taft B., Kelley S. Electrocatalytic detection of pathogenic DNA sequences and antibiotic resitance markers. Anal. Chem. 2003, 75:6327-6333

Lapierre-Devlin M., Asher C., Taft B., Gasparac R., Roberts M., Kelley S. Amplified electrocatalysis at DNA-modified nanowires. Nano Letters. 2005, 5:1051-1055

Leber M., Kaderali L., Schönhuth A., Schrader R. A fractional programming approach to efficiënt DNA melting temperature calculation. Bioinformatics. 2005, 21: 2375 – 2382

Lefferts J., Janetto P., Tsongalis G. Evaluation of the Nanosphere Verigene® System and the Verigene® F5/F2/MTHFR Nucleic Acid Tests. Experimental and molecular pathology. 2009, 87:105-108

Lettau K., Warsinke A., Katterle M., Danielsson B., Scheller F.W. A bifunctional molecularly imprinted polymer: analysis of binding and catalysis by a thermistor. Angew. Chem. Inte. Ed. 2006, 45: 6986 – 6990

Liang R., Peng H., Qiu J. Fabrication, characterization, and application of potentiometric immunosensor based on biocompatible and controllable three-dimensional porous chitosan membranes. Journal of Colloid and Interface Science. 2008, 320:125-131

Lidsky A.S., Ledley F.D., DiLella A.G., Kwok S.C.M., Daiger S.P., Robson K.J.H., Woo S.L.C. Extensive restriction site polymorphism at the human phenylalanine hydroxylase locus and application in prenatal diagnosis of phenylketonuria. Am J Hum Genet. 1985, 37(4): 619-634

Lin C., Shih C., Chau L. Amperometric L-lactate sensor based on sol-gel processing of an enzyme-linked silicon alkoxide. Anal. Chem. 2007, 79:3757-3763

Lin K., Kunduru V., Bothara M., Rege K., Prasad S., Ramakrishna B. Biogenic nanoporous silica-based sensor for enhanced electrochemical detection of cardiovascular biomarkers proteins. Biosensor Bioelectron 2010, 25:2336-2342

Liu H.X., Sun W.Q., Chen Q., Xu S.Y. Thin-Film Thermocouple Array for Time-Resolved Local Temperature Mapping. IEEE Electron Device Lett. 2011, 32: 1606 – 1608

Lloyd-Jones D., Adams R., Carnethon M., De Simone G., Ferguson T.B., Flegal K., et al. Heart disease and stroke statistics - 2009 update: a report from the American Heart Association Statistics Committee and Stroke Statistics Subcommittee. Circulation. 2009, 119: 480-486

Lodewyckx L. , Vandevyver C., Vandervorst C., Van Steenbergen W., Raus J. and Michiels L. Mutation detection in the alpha-1 antitrypsin gene using denaturing gradient gel electrophoresis. Human Mutation. 2001, 18: 243 – 250

Lui B., Hu R., Deng J., Studies on a potentiometric urea biosensor based on an ammonia electrode and urease, immobilized on a γ-aluminum oxide matrix. Anal. Chim. Acta. 1997, 341:161-169

Maruccio G., Primiceri E., Marzo P., Arima V., Torre A., Rinaldi R. A nanobiosensor to detect single hybridization events. Analyst. 2009, 134: 2458-2461

Meusel M., Renneberg R., Spener F. Development of a heterogeneous amperometric immunosensor for the determination of apolipoprotein E in serum. Biosens. Bioelectron. 1995, 10:577-586

Meyer M.H., Hartmann M., Keusgen M. SPR-based immunosensor for the CRP detection - a new method to detect a well known protein. Biosens. Bioelectron. 2006, 21: 1987-1990

Meyer M.H., Hartmann M., Krause H.J., Blankenstein G., Mueller-Chorus B., Oster J., et al. CRP determination based on a novel magnetic biosensor. Biosens. Bioelectron. 2007, 22: 973-979

Michiels L., François B., Raus J., Vandevyver C. Rapid identification of PKU-associated mutations by multiplex DGGE analysis of the PAH gene. J Inherit Metab Dis. 1996, 19(6): 735-738

Mohan S., Nigam P., Kundu S., Prakash R., A label-free genosensor for BRCA1 related sequence based on impedance spectroscopy. Analyst. 2010, 135:2887-2893

Muntau A.C., Roschinger W., Habich M., Demmelmair H., Hoffmann B., Sommerhoff C.P., et al. Tetrahydrobiopterin as an alternative treatment for mild phenylketonuria. N Engl J Med. 2002, 347(26): 2122-2132

Murib M., van Grinsven B., Grieten L., Janssens S., Vermeeren V., Eersels K., et al. Electronic monitoring of chemical DNA denaturation on nanocrystalline diamond electrodes with different molarities and flow rates. Phys Status Solidi A. 2013, 210:911-917

Muyzer G., Smalla K. Application of denaturing gradient gel electrophoresis and temperature gradient gel electrophoresis in microbial ecology. Antonie van Leeuwenhoek. 1998, 73: 127 – 141

Nassef H., Radi A., O'Sullivan C. Simultaneous detection of ascorbate and uric acid using a selectivel catalytic surface. Anal Chim. Acta. 2007, 583:182-189

Nebel C., Shin D., Rezek B., Tokuda N., Uetsuka H., Watanabe H. Diamond and biology. J. R. Soc. Interface 2007, 4:439-461

Ng J.K., Liu W.T. Miniaturized platforms for he detection of single-nucleotide polymorphisms Anal. Bioanal. Chem. 2006, 3:427 – 434

O.A., Rousseau L., et al. Transparent diamond-on-glass micro-electrode arrays for ex-vivo neuronal study. Phys. Status Solidi A. 2008, 205: 2126 – 2129

O'Regan T. (a), Pravda M., O'Sullivan C., Guilbault G. Development of a disposable immunosensor for the detection of human heart fatty-acid binding

protein in human whole blood using screen-printed carbon electrodes. Talanta. 2002, 57:501-510

O'Regan T. (b), O'Riordan L., Pravda M., O'Sullivan C., Guilbault G. Direct detection of myoglobin in whole blood using a disposable amperometric immunosensor. Anal. Chim. Acta. 2002, 460:141-150

Ozkan D., Erdem A., Kara P., Kerman K., Meric B., Hassmann J., et al. Allele-specific genotype detection of factor V Leiden mutation from polymerase chain reaction amplicons based on label-free electrochemical genosensor. Anal Chem. 2002, 74(23): 5931–5936

Özkumur E., Ahn S., Yalcin A., Lopez C.A., Cevik E., Irani R.J. Label-free microarray imaging for direct detection of DNA hybridization in microarrays. Biosens. Bioelectron. 2010, 25: 1789 – 1795

Paine R.S. The variability in manifestations of untreated patients with phenylketonuria (phenylpyruvic aciduria). Pediatrics. 1957, 20(2):290-302.

Pandey C., Sumana G., Malhotra B. Microstructured Cystine Dendrites-Based Impedimetric Sensor for Nucleic Acid Detection. Biomacromolecules 2011, 12:2925-2932

Paniccia R., Fedi S., Carbonetto F., Noferi D., Conti P., Bandinelli B. et al. Evaluation of a new point-of-care celite-activated clotting time analyzer in different clinical settings. Anesthesiology. 2003, 99:54-59

Panini N., Messina G., Salinas E., Fernandez H., Raba J., Integrated microfluidic systems with an immunosensor modified with carbon nanotubes for detection of prostate specific antigen (PSA) in human serum samples. Biosens. Bioelectron. 2008, 23:1145-1151

Park J.Y., Park S.M. DNA hybridization sensors based on electrochemical impedance spectroscopy as a detection tool. Sensors. 2009, 9: 9513 – 9532

Park S.J., Taton T.A., Mirkin C. A. Array-based detection of DNA with nanoparticle probes. Science. 2002, 295: 1503-1506

Pasceri V., Willerson J.T., Yeh E.T. Direct proinflammatory effect of C-reactive protein on human endothelial cells. Circulation 2000, 102: 2165-2168

Peeters M., Csipai P., Geerets B., Weustenraed A., van Grinsven B., Thoelen R., et al., Heat-transfer-based detection of L-nicotine, histamine, and serotonin using molecularly imprinted polymers as biomimetic receptors. Anal. Bioanal. Chem. 2013, 405:6453–6460

Perez-Ruiz E., Vandenryt T., Witters D., Decrop D., van Grinsven B., Wagner P., et al., Integration of heat-transfer resistance measurements onto a digital microfluidic platform towards the miniaturized and automated label-free detection of biomolecular interactions. (In preparation)

Pernot J., Volpe P.N., Omnes F., Muret P., Mortet V., Haenen K., et al. Hall hole mobility in boron-doped homoepitaxial diamond. Physical Review B. 2010, 81

Phenylalanine Hydroxylase Locus Knowledgebase. Canada: DeBelle Laboratory; c2002-10 [updated 2009 August 31]; URL: http://www.pahdb.mcgill.ca. Accessed November 26, 2013.

Pividori M., Lermo A., Bonanni A., Alegret S., del Valle M. Electrochemical immunosensor for the diagnosis of celica disease. Anal. Biochem. 2009, 388:229-234

Poghossian A., Cherstvy A., Ingebrandt S., Offenhäuser A., Schöning M.J. Field-effect sensors with charged macromolecules: characterization by capacitance-voltage, constant-capacitance, impedance spectroscopy and atomi-force microscopy. Sens. Actuators B. 2005, 111:470 – 480

Poté J., Rossé P., Roselli W., Van W.T., Wildi W. Kinetics of mas and DNA decomposition in tomato leaves. Chemosphere. 2005, 61: 677 – 684

Prabhulkar S., Alwarappan S., Liu G., Li C. Amperometric micro-immunosensor for the detection of tumor biomarker. Biosens. Bioelectron. 2009, 24:3524-3530

Privalov P.L., Ptitsyn O.B., Birshtein T.M. Determination of stability of the DNA double helix in an aqueous medium. Biopolymers. 1969, 8:

Qamhieh K., Wong K., Lynch G.C., Pettitt B.M. The melting mechanism of DNA tethered to a surface. Int J Numer Anal Model. 2009, 6(3): 474-488

Quershi A., Gurbuz Y., Kang W., Davidson J. A novel interdigitated capacitor based biosensor for detection of cardiovascular risk marker. Biosens Bioelectron. 2009, 25:877-882

Qureshi A., Kang W., Davidson J., Gurbuz Y. Review on carbon-derived, solid-state, micro and nano sensors for electrochemical sensing applications. Diamond & Related Materials 2009, 18:1401-1420

Qureshi A., Niazi J., Kallempudi S., Gurbuz Y. Label-free capacitive biosensor for sensitive detection of multiple biomarkers using gold interdigitated capacitor arrays. Biosens Bioelectron 2010, 25:2318-2323

Radomska A., Koncki R., Pyrzynska K., Glab S. Bioanalytical system for control of hemodialysis treatment based on potentiometric biosensors for urea and creatinine. Anal. Chim. Acta 2004, 523:193-200

Rahman M., Shiddiky M., Park J., Shim Y. An impedimetric immunosensor for the label-free detection of bisphenol A. Biosens. Bioelectron. 2007, 22:2464-2470

Rant U., Arinaga K., Scherer S., Pringsheim E., Fujita S., Yokoyama N. Swithable DNA interfaces for the highly sensitive detection of label-free DNA targets. Proc. Natl. Acad. Sci. USA. 2007, 104: 17364 – 17369

Raus J. and Michiels L. Mutation detection in the alpha-1 antitrypsin gene using denaturing gradient gel electrophoresis. Human Mutation. 2001, 18: 243 – 250

Rezaei B., Khayamian T., Majidi N., Rahmani H. Immobilization of specific monoclonal antibody on Au nanoparticles for hGH detection by electrochemical impedance spectroscopy. Biosens Bioelectron 2009, 25:395-399

Rezaei B., Majidi N., Rahmani H., Khayamian T. Electrochemical impedimetric immunosensor for insulin like growth factor-1 using specific monoclonal antibody-nanogold modified electrode. Biosens Bioelectron 2011, 26:2130-2134

Rezek B., Garrido J.A., Stutzmann M., Nebel C.E., Snidero E., Bergonzo P., Local oxidation of hydrogenated diamond surfaces for device fabrication, Phys. Stat. Sol. (a) 2002, 193: 523-528

Rezek B., Shin D., Nebel C.E. Properties of hybridized DNA arrays on single-crystalline undoped and boron-doped diamonds studied by atomic force microscopy in electrolytes. Langmuir. 2007, 23: 7626 – 7633

Ridker P.M., Cushman M., Stampfer M.J., Tracy R.P., Hennekens C.H., Inflammation, aspirin, and the risk of cardiovascular disease in apparently healthy men. N. Engl. J. Med. 1997, 336: 973-979

Riess O., Michel A., Speer A., Cobet G., Coutelle C. Introduction of genomic diagnosis of classical phenylketonuria to the health care system of the German Democratic Republic. Clin Genet. 1987, 32(4): 209-215

Roche S., Tiers L., Provanasal M., Seveno M., Piva M., Jouin P., et al., Depletion of one, six, twelve or twenty major blood proteins before proteomic analysis: The more the better? Journal of proteomics. 2009, 72:945-951

Sakata T., Miyahara Y. Potentiometric detection of single nucleotide polymorphism by using a genetic filed-effect transistor. ChemBioChem. 2005, 6: 703 – 710

Sakon J.J., Ribeill G.J., Garguilo J.M., Parkins J., Weninger K.R., Nemanich R.J. Fluorescence quenching effects of nanocrystalline diamond surfaces. Diamond & Related Materials. 2009, 18(1): 82-87

Santandrea M., Alegret S., Fabregas E. Determination of b-HCG using amperometric immunosensors based on a conducting immunocomposite. Anal. Chim. Acta. 1999, 396:181-188

Sasaki Y., Kawarada H. Low drift and small hysteresis characteristics of diamond electrolyte-solution-gate FET. Journal of Physics D-Applied Physics 2010, 43

Schnabl K., Bagherpoor S., Diker P., Cursio C., Dubois J., Yip P. Evaluation of the analytical performance of the Nova StatSensor creatinine meter and the reagent strip technology for whole blood testing. Clin. Biochem. 2010, 43:1026-1029

Schon E.A., Bonilla E., DiMauro S. Mitochondrial DNA mutations and pathogenesis. J. Bioenerg. Biomembr. 1997,

Seland F., Tunold R., Harrington D., Impedance study of methanol oxidation on platinum electrodes. Electrochim. Acta. 2006, 51:3827-3840

Sesso H.D., Buring J.E., Rifai N., Blake G.J., Gaziano J.M., Ridker P.M. C-reactive protein and the risk of developing hypertension. JAMA. 2003, 290: 2945-2951.

Shin D., Rezek B., Tokuda D., Takeuchi D., Watanabe H., Nakamura, et al. Photo- and electrochemical bonding of DNA to single crystalline CVD diamond. Phys. Stat. Sol. a. 2006, 203: 3245-3272

Shiskanova T. V., Volf R., Krondak M., Kral V. Functionalization of PVC membrane with ss oligonucleotides for a potentiometric biosensor. Biosens. Bioelectron. 2007, 22: 2712-2717

Shriver-Lake L., Donner B., Edelstein R., Breslin K., Bhatia S., Ligler F. Antibody immobilization using heterobifunctional crosslinkers. Biosens Bioelectron 1997, 12:1101–1106.

Siegmann-Thoss C., Renneberg R., Glatz J., Spener F., Enzyme immunosensor for diagnosis of myocardial infarction. Sensor and Actuators B. 1996, 30:71-76

Smirnov I., Shafer R.H. Effect of loop sequence and size on DNA aptamer stability. Biochemistry. 2000, 39: 1462–1468

Stavis C., Clare T., Butler J., Radadia A., Carr R., Zeng H., et al. Surface functionalization of thin-film diamond for highly stable and selective biological interfaces

Steel A.B., Levicky R., Herne T.M., Tarlov M.J. Immobilization of nucleic acids at solid surfaces: effect of oligonucleotide length on layer assembly. Biophys. J. 2000, 79(2): 975-981

Stern E., Vacic A., Rajan N., Criscione J., Park J., Ilic B., et al., Label-free biomarker detection from whole blood. Nat Nanotechnol. 2010, 5:138-142

Swain G.M., Ramesham M. The electrochemical activity of boron-doped polycrystalline diamond thin-film electrodes. Anal. Chem. 1993, 65: 345-351

Syu M., Chang Y. Ionic effect investigation of a potentiometric sensor for urea and surface morphology observation of entrapped urease/polypyrrole matrix. Biosens. Bioelectron. 2009, 24:2671-2677

Takahashi K., Tanga M., Takai O., Okamura H., DNA bonding to diamond. Bio. Ind. 2000, 17: 44-51.

Tang D., Ren J. Direct and Rapid Detection of Diphtherotoxin via Potentiometric Immunosensor Based on Nanoparticles Mixture and Polyvinyl Butyral as Matrixes. Electroanalysis. 2005, 17:2208-2216

Tang L., Tsai C., Gerberich W.W., Kruckeberg L., Kania D.R., Biocompatibility of chemical-vapour-deposited diamond, Biomaterials. 1995, 16: 483-488

Taton T. A., Mirkin C. A., Letsinger R. L. Scanometric DNA array detection with nanoparticle probes. Science 2000, 289:1757–60.

Thévenot D. R., Toth K., Durst R., Wilson G.S. Electrochemical biosensors: Recommended definitions and classification. Pure Appl. Chem. 1999, 71(12): 2333-2348

Tindall E. A., Petersen D.C., Woodbridge P., Schipany K., Hayes V.M. Assessing high-resolution melt curve analysis for accurate detection of gene variants in complex DNA fragments Human Mutation. 2009, 30: 876 – 883

Tully E., Higson S., O'Kennedy R. The development of a 'labeless' immunosensor for the detection of Listeria monocytogenes cell surface protein, Internalin B. Biosens Bioelectron 2008, 23:906-912

Turner A. P. F. Biosensors: Sense and sensibility. Chem Soc Rev. 2013, 42(8): 3175-3648

Uetsuka H., Shin D., Tokuda N., Saeki K., Nebel C.E. Electrochemical grafting of boron-doped single-crystalline chemical vapor deposition diamond with nitrophenyl molecules. Langmuir. 2007, 23: 3466-3472

Ushizawa K., Sato Y., Mitsumori T., Machinami T., Ueda T., Ando T. Covalent immobilization of DNA on diamond and its verification by diffuse reflectance infrared spectroscopy. Chem. Phys. Lett. 2002, 351: 105-108

Uslu F., Ingebrandt S., Mayer D., Böcker-Meffert S., Odenthal M., Offenhäusser A. Label-free fully electronic nucleic acid detection system based on label-free DNA targets. Biosens. Bioelectron. 2004, 19: 1721 – 1731

van Grinsven B., Vanden Bon N., Grieten L., Murib M., Janssens S.D., Haenen K., et al. Rapid assesment of the stability of DNA duplexes by impedimetric realtime monitoring of chemically induced denaturation. Lab Chip. 2011, 11: 1656 – 1663

van Grinsven B., Vanden Bon N., Strauven H., Grieten L., Murib M. Janssens S.D. et al. Heat-Transfer Resistance at Solid-Liquid Interfaces: A Tool for the Detection of Single-Nucleotide Polymorphisms in DNA. ACS Nano. 2012, 6(3): 2712-2721

van Grinsven B., Vandenryt T., Duchateau S., Gaulke A., Grieten L., Thoelen R. Phys. Status Solidi A. Customized impedance spectroscopy device as possible sensor platform for biosensor applications. 2010, 9: 2110 – 2113

Vasconcelos E., Peres N., Pereira C., da Silva V., da Silva E., Dutra R. Potential of a simplified measurement scheme and device structure for a low cost label-free point-of-care capacitive biosensor. Biosens Bioelectron 2009, 25:870-876

Velizhanin K.A., Chien C.C., Dubi Y., Zwolak M. Driving denaturation: nanoscale thermal transport as a probe of DNA melting. Phys. Rev. E.

Vermeeren V., Bijnens N., Wenmackers S., Daenen M., Haenen K., Williams O., et al., Towards a real-time, label-free, diamond-based DNA-sensor. Langmuir. 2007, 23: 13193-13202.

Vermeeren V., Grieten L., Vanden Bon N., Bijnens N., Wenmackers S., Janssens S., et al. Sensors and Actuators 2011, 1: 130-138

Vermeeren V., Wenmackers S., Daenen M., Haenen K., Williams O., Ameloot M. Topographical and Functional Characterization of the ssDNA Probe Layer Generated Through EDC-Mediated Covalent Attachment to Nanocrystalline Diamond Using Fluorescence Microscopy. Langmuir. 2008, 24:9125-9134

Vermeeren V., Wenmackers S., Wagner P., Michiels L. DNA Sensors with Diamond as a Promising Alternative Transducer Material. Sensors 2009, 9:5600-5636

Wang J., Firestone M.A., Auciello O., Carlisle J.A., Functionalization of ultrananocrystalline diamond films by electrochemical reduction of aryldiazonium salts. Langmuir. 2004, 20: 450-456

Wang X.Y. , Ruther R.E., Streifer J.A., Hamers R.J. Photochemical grafting of

Wartell R.M., Hosseini S., Powell S., Zhu J. Detecting single base substitutions, mismatches and bulges in DNA by temperature gradient gel electrophoresis and related methods. J Chromatograph A. 1998, 806(1): 169-185

Weizmann Y., Chenoweth D., Swager T. DNA-CNT nanowire networks for DNA detection. J Am Chem Soc. 2011, 133:3238-3241

Wenmackers S., Vermeeren V., vandeVen M., Ameloot M., Bijnens N., Haenen K., et al. Diamond-based DNA sensors: surface functionalization and read-out technologies. Phys. Status Solidi A. 2009, 206(3): 391-408

Williams O., Nesladek M., Daenen M., Michaelson S., Hoffman A., Osawa E., et al. Growth, electronic properties and applications of nanodiamond. Diamond & Related materials 2008, 17:1080-1088

Woo S. L. C., Lidsky A.S., Guttler F., Chandra T., Robson K.J.H. Cloned human phenylalanine hydroxylase gene permits prenatal diagnosis and carrier detection of classical phenylketonuria. Nature. 1983, 306(5939): 151-155

World Health Organization. World Health Statistics Annual. 1998, Ref Type: Report

Yagiuda K., Hemmi A., Ito S., Asano Y., Fushinuki Y. Chen C., et al., Development of a conductivity-based immunosensor for sensitive detection of methamphetamine (stimulant drug) in human urine. Biosens Bioelectron. 1996, 11:703-707

Yamanaka S., Takeuchi D., Watanabe H., Okushi H., Kajimura K., Low-compensated boron-doped homoepitaxial diamond films, Diamond Relat. Mater. 9 (2000) 956-959.

Yang N., Uetsuka H., Osawa E., Nebel C.E. Vertically aligned diamond nanowires for DNA sensing. Angew. Chem. Int. Ed. 2008, 47: 5183 – 5185

Yang W., Auciello O., Butler J.E., Cai W., Carlisle J.A., Gerbi J.E. DNA-modified nanocrystalline diamond thin-films as stable, biologically active substrates. Nat. Mater. 2002, 1: 253-257

Yang W., Butler J.E., Russell J.N., Hamers R.J. Direct electrical detection of antigen-antibody binding on diamond and silicon substrates using electrical impedance spectroscopy. Analyst. 2007, 132: 296-306

Zhou Y., Yu B., Guiseppi-Ellie A., Sergeyev V., Levon K. Potentiometric monitoring DNA hybridization. Biosens. Bioelectron. 2009, 24:3275-3280

Zhu L., Luo L., Wang Z. DNA electrochemical biosensor based on thionine-graphene nanocomposite. Biosens Bioelectron. 2012; 35(1): 507–511

Curriculum Vitae

Natalie Vanden Bon werd geboren op 20 juni 1986 te Maaseik. In 2004 behaalde ze haar diploma Algemeen Secundair Onderwijs (ASO) in de afstudeerrichting Wetenschappen-Wiskunde aan de Stedelijke Humaniora te Dilsen-Stokkem. Vervolgens startte ze haar bachelor opleiding in de Chemie aan de Universiteit Hasselt, waar ze in 2007 het diploma bachelor in de Chemie met specialisatie Levenswetenschappen behaalde. Haar bachelorthesis, getiteld “Het effect van Triton X-100 op de oplosbaarheid van thylakoidmembranen” werd uitgevoerd aan het centrum voor milieukunde binnen de onderzoeksgroep moleculaire en fysische plantkunde onder leiding van Prof. Dr. Roland Valcke. Aansluitend startte ze haar master opleiding in de Biochemie en Biotechnologie aan de Universiteit Antwerpen, waar ze in 2009 zowel het FELASA C Certificaat voor proefleider in de proefdierkunde als het diploma master in de Biochemie en Biotechnologie, finaliteit onderzoek in moleculaire en cellulaire genbiotechnologie, met onderscheiding behaalde. Tijdens deze opleiding genoot ze in 2008 een tien weken durende masterstage, getiteld “Een systeembiologische benadering van de effecten van cadmiumblootstelling aan de zebravis via water en via voedsel”. Deze stage werd uitgevoerd aan het laboratorium van ecofysiologie, biochemie en toxicologie onderleiding van Dr. K. van der Ven. Haar masterthesis, getiteld “De expressie en opzuivering van globine gekoppelde sensoren” werd uitgevoerd binnen de onderzoeksgroep Proteïnechemie en Proteoomanalyse onder leiding van Prof. Dr. Luc Moens. In september 2009 startte ze haar doctoraat aan het Biomedische Onderzoeksinstituut van de Univeristiteit Hasselt binnen de onderzoeksgroep Immunologie/Biochemie. Tijdens deze periode van 4 jaar deed ze onderzoek naar de ontwikkeling van DNA en immunsensoren voor de detectie van DNA mutaties en eiwitmerkers, onder leiding van Prof. Dr. Luc Michiels, Dr. Veronique Vermeeren en Prof. Dr. Patrick Wagner. Ze werkte tevens mee aan het Interreg project, getiteld “NanoSensEu”, gefinancieerd door de Europese Unie. In het kader van dit Interreg project werkte ze actief mee aan de organisatie van the 2nd NanoSensEu Symposium on Biosensor Development: “Trends and Technology”, dat plaatsvond op 25 april 2012, aan de Universiteit Hasselt. Tijdens haar doctoraat behaalde ze het certificaat van de doctoral school for

Medicine and Life Sciences en volgde ze de cursussen Introduction to kinetic analysis in Biacore™ systems (GE Healthcare), Advanced course in kinetic analysis with Biacore™ technology (GE Healthcare), Introduction to bioinformatics (GIGA), Parametric and non-parametric methods for the life sciences (BioStat, UHasselt), Onderzoek en Intellectuele eigendom (Tech Transfer, UHasselt), Zoeken in octrooibanken voor onderzoekers (Tech Transfer, UHasselt), The importance of innovation and entrepreneurship in the biotech sector (FlandersBio), Presentation Skills (Skills3), A series of tutorial lectures on microfluorimetry in biomedical research (UHasselt), Kleine branden blussen (PLOT), Project management (True Colours), Lab safety (UHasselt), Lab book taking (UHasselt) en Good scientific conduct (UHasselt). Daarnaast was ze stagebegeleider voor zowel bachelor als masterstudenten van zowel de Provenciale Hogeschool Limburg als de Universiteit Hasselt. Verder nam ze actief deel aan het onderwijs van de vakken 'Bioinformatica', 'Ziek organisme' en 'Exploratie' uit het 3de bachelor biomedische wetenschappen van de Univeristeit Hasselt.

Publications

1. Vanden Bon N., van Grinsven B., Murib M.S., Yeap W.S, Haenen K., De Ceuninck W., Wagner P., Ameloot M., Vermeeren V., and Michiels L. Heat-transfer-based detection of SNPs in the PAH gene of PKU patients Int J Nanomedicine 2014, 9: 1629 – 1640

2. van Grinsven B., Vanden Bon N., Strauven H., Grieten L., Murib M., Jimenez Monroy K.L., Janssens S.D., Haenen K., Schöning M.J., Vermeeren V.,Ameloot M., Michiels M., Thoelen R., De Ceuninck W. and Wagner P. Heat-transfer resistance at solid-liquid interfaces: a new tool for the detection of single nucleotide polymorphisms in DNA. ACS Nano 2012, 6(3): 2712 – 2721

3. Vermeeren V., Grieten L., Vanden Bon N., Bijnens N., Wenmackers S., Janssens S.D., Haenen K., Wagner P. and Michiels L. Impedimetric, diamond-based immunosensor for the detection of C-reactive protein. Sensors and Actuators B 2011, 157: 130 – 138

4. van Grinsven B., Vanden Bon N., Grieten L., Murib M., Janssens S.D., Haenen K., Schneider E., Ingebrandt S., Schöning M.J., Vermeeren V.,Ameloot M., Michiels L., Thoelen R., De Ceuninck W. and Wagner P. Rapid assessement of the stability of DNA duplexes by impedimetric real-time monitoring of chemically induced denaturation. Lab Chip 2011, 11(9): 1656 – 1663

5. Grieten L., Janssens S.D., Ethirajan A., Vanden Bon N., Ameloot M., Michiels L., Haenen K. and Wagner P. Real-time study of protein adsorption on thin nanocrystalline diamond. Phys Status Solidi A 2011, 208(9): 2093 – 2098

Oral Presentation

1. Vanden Bon N., Vermeeren V., van Grinsven B., Haenen K., De Ceuninck W., Wagner P., Ameloot M. and Michiels L. A diamond-based DNA-sensor used for real-time and electronic detection of point mutations. 11th International Symposium on Mutation in the Genome 2011, 6th-10th june, Santorini, Greece

Poster Presentations

1. Vanden Bon N., van Grinsven B., Vermeeren V., Murib M., Janssens S.D., Haenen K., Ameloot M., De Ceuninck W., Wagner P. and Michiels L. Development of a diamond-based biosensor for the detection of point mutations in PKU patients based on the heat-transfer resistance principle
    - International Diamond Workshop, 2013, Hasselt, Belgium

2. Vanden Bon N., Vermeeren V., Grieten L., Janssens S.D., Haenen K., Wagner P. and Michiels L. Development of a diamond-based, electronic sensor platform for rapid and reliable medical diagnostics.
    - International Diamond Workshop, 2012, Hasselt, Belgium

3. Vanden Bon N., Vermeeren V., Grieten L., Haenen K., Wagner P. and Michiels L. Development of an electronic sensor platform for rapid and reliable medical diagnostics.
    - World congress on Biosensors, 2012, Cancun, Mexico

4. Vanden Bon N., Vermeeren V., Grieten L., Bloemen K., Janssens S.D., Jacob A., Haenen K., Ameloot M., van IJzendoorn L., Wagner P. and Michiels L. The development of an all-round sensor platform for biomarker detection in medical diagnostics.
    - Advances in Biodetection and Biosensors, 2012, Edinburgh, U.K.
    - NanoSensEu Symposium, 2012, Diepenbeek, Belgium

5. Vanden Bon N., Vermeeren V., van Grinsven B., Grieten L., Tran D.T., Lammertyn J., Ameloot M., Haenen K., De Ceuninck W., Wagner P and Michiels L. The use of diamond as a flexible surface for the attachment of different bioreceptors in the development of impedimetric biosensors
    - Spring meeting Material Research Society, 2011, San Francisco, U.S.A.

6. Vanden Bon N., Vermeeren V., van Grinsven B., Ameloot M., Haenen K., De Ceuninck W., Wagner P. and Michiels L. A diamond based, impedimetric biosensor used for realtime SNP detection
    - Biomedica life science summit, 2011, Eindhoven, The Netherlands

7. Vanden Bon N., Vermeeren V., van Grinsven B., Ameloot M., Haenen K., De Ceuninck W., Wagner P. and Michiels L. Real-time SNP-detection using a diamond based, impedimetric DNA-sensor
    - International Diamond Workshop, 2011, Hasselt, Belgium
8. Vanden Bon N., Vermeeren V., Grieten L., Haenen K., Wagner P. and Michiels L.Real-time detection of C-reactive protein with a diamond-based, impedimetric immunosensor
    - Knowledge for growth, 2011, Gent, Belgium

9. Vanden Bon N., Vermeeren V., Grieten L., Haenen K., Wagner P. and Michiels L. Label-Free and Real-time Detection of C-reactive Protein with a Diamond-Based, Impedimetric Immunosensor
    - Bio-Sensing Technology, 2011, Amsterdam, The Netherlands

Dankwoord

Het is mij gelukt, de resultaten van vier jaar onderzoek gebundeld in een boekje! Dit boekje zou ik evenwel niet hebben kunnen verwezenlijken zonder jullie hulp! Daarom wil ik in dit laatste hoofdstuk een woordje van dank richten aan iedereen die een bijdrage heeft geleverd aan mijn thesis.

In de eerste plaats een woord van dank aan mijn promoter prof. dr. Luc Michiels. Luc, bedankt om mij de kans te geven om dit doctoraatsonderzoek uit te voeren, maar vooral om steeds in mij en in de succesvolle afronding van dit project te blijven geloven. Ook zal ik onze autoritten van Mol naar Diepenbeek en de bijhorende gesprekken nooit vergeten! Ook mijn co-promotoren, prof. dr. Patrick Wagner en dr. Veronique Vermeeren verdienen een welgemeende dankjewel. Patrick, dankjewel voor de beschikbare meetapparatuur in het IMO en voor je eeuwige enthousiasme en oprechte interesse in dit project. Dr. Veronique Vermeeren, jij hebt mij vier jaar geleden wegwijs gemaakt binnen het biosensorenonderzoek. Bedankt voor de ontelbare uren die je hebt gespendeerd aan het nalezen, verbeteren en bijsleutelen van al mijn abstracts, papers en dit boekje. Ik hoop dat er nergens nog –ly fouten in staan ☺. Ook had je steeds een luisterend oor voor al mijn mogelijke 'problemen' en dit zowel tijdens als buiten de werkuren. Maar ik zal ook de toffe congressen samen en de voor mij heel spannende Halloweenavond bij jouw thuis nooit vergeten. Veronique, je schitterde als een diament binnen je functie als biosensor post-doc, maar je doet het zeker en vast ook schitterend in je nieuwe job. Veel succes bij LRM!

Alle leden van de jury en de jury voorzitter wil ik oprecht bedanken voor hun kritische blik op en evaluatie van dit werk. Nog een speciaal woordje van dank aan prof. dr. Marcel Ameloot. Marcel, bedankt voor het steeds grondig nalezen van mijn papers, en voor de tijd die u vrijmaakte om wiskundige en fysische begrippen extra ter verduidelijken met zelf getekende figuren en de nodige wetenschappelijke literatuur.

Mijn doctoraatsonderzoek kaderde gedeeltelijk in het ruimere interuniversitaire project "NanoSensEu". Ik ben blij dat ik heb mogen deel uitmaken van dit

project, en ik wil dan ook alle NanoSensEu-collega's bedanken voor de fijne samenwerking.

Anderzijds werkte ik tijdens mijn doctoraat nauw samen met het Instituut voor Materiaal Onderzoek. In het bijzonder ben ik de onderzoekers van de WBGM-groep van prof. dr. Ken Haenen zeer dankbaar voor de vele zelfgegroeide diamantstalen. Weng, thanks for all the working hours during the weekend to clean my samples! Ook prof. dr. Ward De Ceuninck, bedankt voor uw oprechte interesse in en voor de technologische steun binnen het DNA-luik van mijn doctoraatsproefschrift. Verder verdienen de onderzoekers van de BIOS-groep van prof. dr. Patrick Wagner zeker een welverdiend plaatsje in mijn dankwoord. Mo, 'dankuwel' for the hundreds of samples you hydrogenated and carboxylated for me, even during the weekend! Bart, bedankt voor de technologische ondersteuning binnen het DNA-project, voor de leuke uren in de kelder van Biomed en voor het inzetten van de vele stalen tijdens mijn zwangerschap, zonder jou was het laatste artikel er nooit zo snel gekomen. Veel succes met je nieuwe job aan de universiteit van Maastricht! Lars, dankjewel om de vele technische begrippen uit te leggen in mensentaal, om mij wegwijs te maken in de vele dataverwerkingsprogramma's en voor de aangename babbels tijdens de steeds lang durende stabilisatieperiodes. Doen we ons wedstrijdje van in Glasgow, deze keer wel met Belgisch bier, nog eens over op mijn feestje? ☺

Ook mijn collega's van het biomedisch onderzoeksinstituut wil ik allemaal bedanken voor de toffe samenwerking en de gezellige sfeer en dit zowel in het labo, tijdens de middagpauzes als tijdens het jaarlijkse kerstfeestje, de Biomed bbq, het bezoek aan de kerstmarkt en de vele andere Biomed-feestjes! Een extra dankjewel voor Anne, Christel, Erik, Igna, Katrien en Regine voor de dagdagelijkse ondersteuning van mijn labexperimenten, voor Agnes, Veronique P, Rani, Jean, Laura en Els voor het in orde maken van alle administratie en voor Paul, voor het steeds ijs en sneeuwvrij houden van de trappen in de winter! Lotte, jij verdient een extra dikke merci voor alle experimenten die jij voor mij hebt uitgevoerd. Ik wens je veel succes in het zoeken naar een nieuwe job! De mannen (Nick, Ben, Kristof en Rik) en ondertussen ook vrouwen (Kathleen en Sarah) van in de bureau op de kelderverdieping van Biomed, ben ik ook erg

dankbaar voor de vele hulp bij het gebruik van de confocale microscoop en bij het verwerken van de fluorescente beelden. Ook wil ik graag mijn mede-doctoraatstudenten van de biosensorgroep bedanken omdat ze zo'n toffe collega's zijn! Karolien, je was aangenaam gezelschap tijdens onze Amsterdam-trip en Mexico-reis. Veel succes met jullie verbouwingen, als het af is kom ik naar Aalsts carnaval! Jeroen, ik heb 4 jaar een bureau met je gedeeld en toch leerde ik je pas echt kennen in de lange treinrit naar Amsterdam. Veel succes met de afronding van je doctoraat en in je nieuwe job! Kaushik, I will never forget the Indian dinners at your place en of course your wedding in India! Good luck with writing your thesis and with your new job in Dublin! Will you also arrange a tour for us in Dublin? ☺ Evi, ook al was je het merendeel van de tijd op de FOR, het was altijd tof als je ons kwam vergezellen in onze bureau. Onze India-tour was uiteraard onvergetelijk, maar onze middaguitstapjes naar de Quick zal ik ook niet snel vergeten! Veel succes nog op de FOR! Katrijn, jij was er steeds om mij te vergezellen zowel in de vroege als in de late uurtjes, zowel op onze bureau als in het labo. Jij kent ook als geen ander al mijn ups and downs van de afgelopen vier jaar, je diploma van psychologie kwam hier goed van pas! Jij bent ook een krak in het maken en geven van gestructureerde presentaties, het formuleren van mooie titels en het (her)schrijven van teksten. Dus het schrijven van je doctoraat en de bijhordende presentatie zullen absoluut geen probleem vormen voor jou, veel succes in je laatste thesis jaar!

Ook een dikke merci aan al mijn vrienden en kennissen voor de nodige ontspanning en sportieve inspanningen! Na mijn verdediging heb ik terug tijd om mijn zwempak, tennisschoenen en mijn naaimachine onder het stof te halen! En Floer, Xilo, Moev, Crusj en Dédété reserveer alvast maar een tafeltje om nog eens gezellig te gaan eten en bij te babbelen, want dat is al veel te lang geleden!

Een speciale dank u voor mijn Desselse familie. Merci voor de steun en de fijne familiefeesten, ik voel mij echt thuis in Dessel dankzij jullie! Breg, merci dat je steeds paraat staat om met je magische handen de stress te laten verdwijnen uit mijn nek en rug! Ria en Ludo, merci voor alles wat jullie doen voor mij, Lasse en de verbouwingen, zonder jullie hulp zou het niet lukken!

Ook mijn familie verdient een extra woordje van dank. Mijn grootouders voor de belangstelling in mijn doctoraat, tijdens de wekenlijkse telefoontjes. Jolien, ik vind het fijn dat je vandaag komt supporteren voor mij! Mammie en Danny, dankjewel dat jullie steeds klaar staan voor mij en steeds een luisterend oor hebben voor al mijn kleine en grote problemen. Dankjewel voor jullie steun in alles wat ik doe, ik weet zeker dat jullie vandaag trots gaan zijn op jullie dochter! Danny, ook bedankt om alle kleine foutjes uit mijn doctoraatstekst te halen.

Lennert, je hebt de voorbije maanden echt afgezien met mij, ik was heel prikkelbaar en met momenten echt onhandelbaar. En toch bleef je altijd je rustige zelf en kwam je me altijd helpen wanneer ik het je, niet altijd even vriendelijk, vroeg. Je kon me steeds weer kalmeren en met een mopje over bv. een grappige referentie kon je me soms zelfs weer aan het lachen krijgen. Merci om er altijd voor mij te zijn en om zo een goede papa te zijn voor onze Lasse! Nu kunnen we terug samen ONS huis (ver)bouwen!

Natalie
Mei 2014